



An Open Access Journal Available Online

Covenant Journal of Engineering Technology (CJET)

Vol. 4 No. 2, December 2020

Publication of the College of Engineering, Covenant University, Canaanland.

Editor-in-Chief: Dr. Imhade Princess Okokpujie
editorcjet@covenantuniversity.edu.ng

URL: <http://journals.covenantuniversity.edu.ng/index.php/cjet>

© 2020 Covenant University Journals

All rights reserved. No part of this publication may be reproduced, stored in a retrieval system or transmitted in any form or by any means, electronic, electrostatic, magnetic tape, mechanical, photocopying, recording or otherwise, without the prior written permission of the publisher.

It is a condition of publication in this journal that manuscripts have not been published or submitted for publication and will not be submitted or published elsewhere.

Upon the acceptance of articles to be published in this journal, the author(s) are required to transfer copyright of the article to the publisher.

ISSN: p. 2682-5317 e. 2682-5325

Published by Covenant University Journals,
Covenant University, Canaanland, Km 10, Idiroko Road,
P.M.B. 1023, Ota, Ogun State, Nigeria

Printed by Covenant University Press

Articles

Reliability of a Health and Safety Complaint Ergonomic Assessment Tool Developed for Improved Work Posture Assessment on the Shop Floor Mgbemena, Chika Edith	1
Development and Performance Evaluation of a Household Liquefied Petroleum Gas Monitoring and Leakage Detector B. J. Olorunfemi, D. E. Adenuga, and A. E. Olumilua	11
Load-ability Analysis during Contingency with Unified Power Flow Controller Using Grey Wolf Optimization Technique Yusuf Samuel Sunday*, Okorie Patrick Ubeh, Abubakar Adamu Saidu, Momoh Illiasu Onimisi & Jimoh Boyi	23
Rainfall Variability and Trend Analysis over Lokoja, Nigeria Animashaun I. M.*, Adeoye P. A. Otache, M. Y and Abatan, O. A.	32
Effect of Temperature and Residence Time on Torrefaction Characteristics of African Birch (<i>Anogeissus leiocarpa</i>) Pious O. Okekunle, Samuel Maduekwe, Gbenga S. Ajadi and Sanyaolu A. Olugbemisoye	43
Effect of Welding Using Electrodes with Certain Treatment on Stainless Steel 304 Using SMAW Welding Iswanto, Ribangun B. Jakaria, Mulyadi, M. Sofwan Hariadi	50
Optimum Portland Cement-Guinea Corn Husk Ash Blend as Filler in Hot Mix Asphalt Abdulmumin Ahmed Shuaibu, Aliyu Mani Umar, Hassan Suleiman Otuoze, *Ashiru Mohammed and Aminu Muhammad Abba	56



An Open Access Journal Available Online

Reliability of a Health and Safety Complaint Ergonomic Assessment Tool Developed for Improved Work Posture Assessment on the Shop Floor

Mgbemena, Chika Edith

Department of Industrial & Production Engineering, Nnamdi Azikiwe University, Awka, Nigeria.
ce.mgbemena@unizik.edu.ng

Received: 18.03.2020

Accepted: 01.10.2020

Published: 31.12.2020

Abstract- Strategies for minimising the rate of occurrence of awkward postures during manual handling operations have been recommended. Awkward postures, if adopted for prolonged periods, can result in Musculoskeletal Disorders (MSDs). Hence, manual operations need to be assessed to identify if awkward postures exist. A real-time automatic Health and Safety (H&S) compliance posture assessment tool based on 3D sensing technology has been developed to assess operators undertaking manual handling tasks. This paper presents the validation of the developed tool using a reference tool. The analysis results indicate little notable angular discrepancies in the data measured by the developed tool and the reference tool. Comparing the data measured with the two tools, it is evident that there is remarkable consistency. The tool could be useful in workplaces to assess new workstations' safety and correct workers' methods in real-time.

Keywords: Microsoft Kinect; Musculoskeletal Disorders; Awkward Postures; Ergonomics; Manual Handling

1. INTRODUCTION

Strategies for minimising awkward postures' rates during manual handling operations have been recommended and include improved workstation design, modified tool design, proper reach distances, adjustable seated and standing workstations [1]–[8]. Researchers have recommended posture assessment as a remedial measure to minimise MSD threat because effective posture assessment is important in ensuring postural comfort [9]–[11]. Existing assessment is normally carried out by observing several operations and carrying out analysis afterward. Although some improvements can be identified for the operations, this lagging assessment cannot alert operators and prevent them from adopting awkward postures in time. The real-time automatic health and safety assessment tool developed by [12] that can prompt the workers to adjust their work postures continuously is of great significance in workplaces .

There are two methods by which human work postures are analysed on the shop floor – the observational technique and the instrument-based technique. The observational technique uses visual

perception to evaluate the rate at which the body moves away from the neutral position. These include the Ovako Working Posture Analysis System, Rapid Upper Limb Assessment, RULA, the Quick Exposure Check, the Rapid Entire Body Assessment, REBA [13]–[18]. The tools are time-consuming and labour-intensive [19]. The instrument-based technique records work postures using instruments [20]. These tools often require offline data collection for posture assessment and include the force plate, photography. Direct body measurements using the goniometers, inclinometers, and 3D analysis using markers. Electromagnetic tracking system, 4D Computer tomography (4D CT) [13], [21]–[24]. Active and passive video-based systems such as the NDI and the Vicon Motion capture systems can pose great problems because they are complex and bulky [25]. The Electromagnetic tracking system, which is less bulky, is less accurate because of the magnetic field interferences caused by metallic objects on the shop floor. The Inertial systems, such as the Xsens, also have their accuracy greatly affected by metals [26]. Photographs and videos often produce an inaccurate measurement of joint

angles resulting from distortions caused by camera placement issues [13].

This study is aimed at testing the developed real-time, automatic, health and safety compliance ergonomic posture assessment tool, which is based on 3D sensing and tracking technology for reliability and validity under repeatable and reproducible conditions

2. MATERIALS AND METHODS

A 12-inch, 360 degrees goniometer was used in this study to measure the exact back flexion, elbow flexion, and shoulder flexion angles of the participants.

2.1. Experimentations

Testing the developed tool, an experiment was conducted to evaluate the closeness of agreement in the tool's measured data and compare the captured data with data from the reference tool (Goniometer). For all the tests, the participants were asked to perform tasks while facing the Kinect at a 2m-distance and 90° horizontal field of view from the sensor, which is placed on a tripod 1.2m above the floor [27], as depicted in Figures 1a and 2a. The back and arm postures were measured at a specified time using the developed tool, as the participants performed the assigned tasks. The Goniometer was also used to record the same angles of the participant at that posture. The measured angles include the back-flexion angle, the shoulder flexion angle, and the elbow flexion angle.

2.2. Data Processing and Statistical Analysis.

Two tests were conducted to assess the precision of measurements obtained from the developed tool compared to the goniometer measurements. These are the repeatability and reproducibility tests.

2.2.1. Repeatability Tests

While a sole participant repeatedly performed a lifting-above-head-height task, the elbow and shoulder angles were measured using the developed tool and the Goniometer. The purpose of the test was to evaluate the consistency and conformity in the data measured by the two independent tools and, consequently, the tool's reliability, when a participant's postures are assessed while wearing the same clothing to perform the same task with the same load severally at the same workstation. The experimental setup

for this study is depicted in Figure 1a. The participant, shown in Figure 1b, was asked to lift a load of 0.5kg from a work table to above head height, while the elbow and shoulder flexion angles are captured at 5 seconds from the start of the lift depicted in Figure 1c. The Goniometer is then used to measure these angles simultaneously as the participant maintains the same posture. This procedure is repeated 30 times. For each capture, the Goniometer is used to measure the participant's elbow and shoulder flexion angles.

The developed tool's measurement results were compared with those of the goniometer measurement to assess the level of agreement and consistency, which helps to inform the precision of measurements obtained from the developed tool. The difference in angular measurements is statistically analysed using the mean, standard deviation, and the inter-item correlation between the two tool's measured data. The intraclass correlation coefficient (ICC) was used to evaluate the tool's test-retest reliability in SPSS version 24.0. The significance level was set at $p < 0.05$ and the results obtained was evaluated from 0 to 0.5 = no/poor agreement/reliability, 0.5 to 0.75 = moderate agreement/reliability, 0.75 to 0.9 = good agreement/reliability and >0.9 = excellent agreement/reliability [28]. ICC was selected because of its suitability in assessing the consistency of quantitative measurements made by different devices measuring the same quantity.

2.2.2. Reproducibility Tests

The purpose of the reproducibility test conducted in this study was to evaluate the consistency and conformity in the data measured by the two independent tools. During the test, postures of different participants were assessed while wearing different clothings to perform different tasks involving different loads in different workplace locations. Sixteen different volunteers participated in the study. Some of the tasks undertaken are presented in Figure 2 and include lifting, hammering, sitting to handle, assembly tasks, and carrying the load. Figures 2a and 2b depict the experimental Setup for the assembly of electrical components and the participant performing the task, respectively. Sixteen participants were asked to perform specified tasks as their back flexion, elbow, and shoulder flexion angles were captured after 5 seconds with the developed tool and



a. Experimental Setup for the repeatability test



b. Participant during the repeatability test



c. Screenshot of the participant as captured by Kinect during repeatability test

Figure 1. Participant during the repeatability test

Goniometer. Figure 2c shows one of the participants who performed the sitting to pick a task, as his left elbow posture was measured with the Goniometer. Figures 2d and 2e presents the screenshots of two participants as tracked and measured by the developed tool.

Angular discrepancies in the two tool's measured data are statistically analysed using the measured data's mean and standard deviation. The Kendall's coefficient of concordance (w) was used to evaluate the level of agreement in the data measured by the two independent tools because of its suitability and versatility in handling data measured by different raters without any regard to the nature of the data's probability distribution. The significance level was set at $p < 0.05$, and the

results obtained were evaluated from 0 = no agreement to 1 = perfect agreement.

3. RESULTS AND DISCUSSION

Results of Testing for Tool's Reliability

The result of the repeated arm posture assessment of a sole participant, captured 30 different times with the developed tool and the Goniometer during a lifting task, is presented in Figure 3. Figure 3 shows, at a glance, the angular discrepancies in the data measured with the developed tool and the reference tool. Generally, there was excellent agreement between the measurements made by the developed tool and the Goniometer when four different arm postures were analysed in SPSS, as summarised in Table 1.



a. Experimental Setup for the reproducibility test



b. Participant during the reproducibility test



c. Measuring the Left elbow of a participant with the Goniometer

AngleNeck	-12.77	LElbow Good	RElbow Good
AngleNeckRight	0	Neck RTL Good	Neck RTR Good
AngleNeckLeft	0	NECK AWKWARD	SpineBase Good
AngleLeftElbow	32.34	LShoulder Good	RShoulder Good
AngleRightElbow	37.63	RightWrist Good	LeftWrist AWKWARD
Angle S B Left	0	SpineB RTR AWKWARD	SpineB RTL Good
Angle S B Right	-13.32		
AngleSpineBase	0		
AngleLeftShoulder	0		
AngleRightShoulder	0		
AngleRightWrist	45.3		
AngleLeftWrist	63.47		

Count: 3694

Start Timer

d. Participant carrying some components

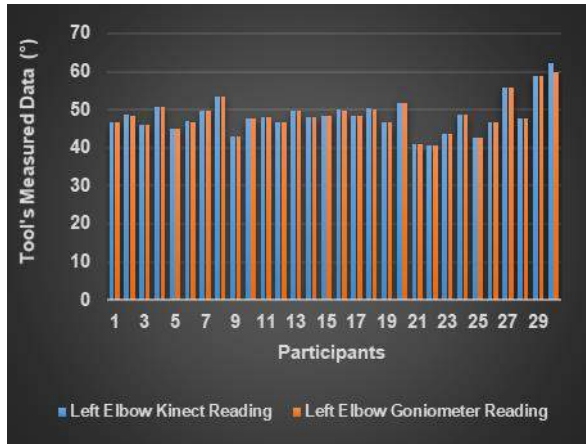
AngleNeck	15.4	LElbow Good	RElbow Good
AngleNeckRight	0	Neck RTL AWKWARD	Neck RTR Good
AngleNeckLeft	17.17	NECK AWKWARD	SpineBase Good
AngleLeftElbow	53.68	LShoulder Good	RShoulder Good
AngleRightElbow	45.37	RightWrist Good	LeftWrist Good
Angle S B Left	10.4	SpineB RTR AWKWARD	SpineB RTL Good
Angle S B Right	23.61		
AngleSpineBase	12.4		
AngleLeftShoulder	0		
AngleRightShoulder	0		
AngleRightWrist	0		
AngleLeftWrist	0		

Count: 823

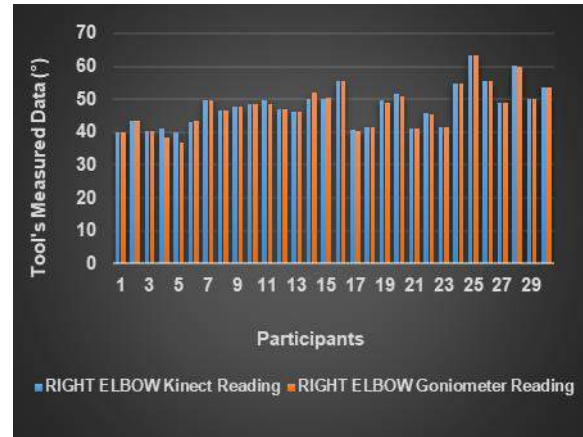
Start Timer
Stop Timer
Color
Depth
Infrared
skeleton

e. Participant handling electrical components

Figure 2 Screenshots of participants during reproducibility testing.



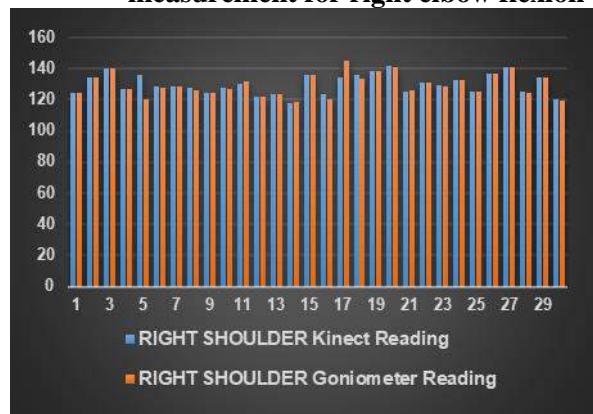
a. Developed tool vs. Goniometer measurement for left elbow flexion



b. Developed tool vs. Goniometer measurement for right elbow flexion



c. Developed tool vs. Goniometer measurement for left shoulder flexion



a. Developed tool vs. Goniometer measurement for right shoulder flexion

Figure 3: Developed tool vs. Goniometer is measured arm posture data of a sole participant under repeatability conditions

Table 1: Result of statistical analysis of the data measured under repeatable conditions.

Posture	Mean (°) & S.D. for new tool's reading	Mean (°) & S.D. for Goniometer reading	Difference in Mean (°) & Difference in S.D.	inter-item correlation	Average Measures for ICC
Left Elbow Flexion	48.45 & 4.72	48.34 & 4.51	0.11 & 0.21	0.997	0.998
Right Elbow Flexion	47.92 & 6.13	47.71 & 6.39	0.21 & 0.26	0.992	0.996
Left Shoulder Flexion	129.16 & 4.76	128.81 & 4.86	0.35 & 0.1	0.982	0.990
Right Shoulder Flexion	130.14 & 6.5	129.67 & 7.15	0.47 & 0.65	0.863	0.925

**ICC = Intraclass correlation coefficient, S.D. = Standard Deviation.

** & Separates the Mean from the Standard Deviation

For left elbow flexion, an average angle of 48.45° and 48.34° with the standard deviation of 4.72 and 4.51 was measured for the 30 participants using the developed tool and the Goniometer, respectively. The apparent similarity in the average angular measurements and standard deviation

indicates no notable difference in the distribution of the data measured by the developed tool and the Goniometer. The difference in measurements of 0.11° is low, indicating that discrepancies in angular measurement between the two tools are small, with a standard deviation of 0.21 indicating

possible consistency in measurement. An inter-item correlation of 0.997 was obtained, showing an excellent correlation between the developed tool's measured data and the Goniometer measured data. The reliability test yielded an average ICC measure of 0.998, which indicates excellent inter-rater reliability. For right elbow flexion, an average angle of 47.92° and 47.71° with the standard deviation of 6.13 and 6.39, was measured for the 30 participants using the developed tool and the Goniometer, respectively. The difference in the measurements was 0.21°, with a standard deviation of 0.26. Again, the obvious similarity in the average angular measurements and standard deviation indicates no notable difference in the distribution of the data measured by the developed tool and the Goniometer. The measurements' difference is low, indicating that discrepancies in angular measurement between the two tools are small. An inter-item correlation of 0.992 was obtained, showing an excellent correlation between the developed tool's measured data and the Goniometer measured data. The reliability test yielded an average ICC measure of 0.996, which indicates excellent inter-rater reliability.

For left shoulder flexion, an average angle of 129.16° and 128.81° with the standard deviation of 4.76 and 4.86 was measured for the 30 participants using the developed tool and the Goniometer. The difference in the measurements was 0.35°, with a standard deviation of 0.1. The obvious similarity is that the average angular measurements and standard deviation indicate no notable difference in the distribution of the data measured by the developed tool and the Goniometer. The measurements' difference is low, indicating that discrepancies in angular measurement between the two tools are small. An inter-item correlation of 0.982 was obtained, indicating an excellent correlation between the developed tool's measured data and the Goniometer measured data. The reliability test yielded an average ICC measure of

0.990, which indicates excellent inter-rater reliability.

For right shoulder flexion, an average angle of 130.14° and 129.67° with the standard deviation of 6.5 and 7.15 was measured for the 30 participants using the developed tool and the Goniometer, respectively. The difference in the measurements was 0.47°, with a standard deviation of 0.65. The obvious similarity is that the average angular measurements and standard deviation indicate no notable difference in the distribution of the data measured by the developed tool and the Goniometer. The measurements' difference is low, indicating that discrepancies in angular measurement between the two tools are small. An inter-item correlation of 0.863 was obtained, indicating a good correlation between the developed tool's measured data and the Goniometer measured data. The reliability test yielded an average ICC measurement of 0.925, which indicates excellent inter-rater reliability.

Similarly, when tested under reproducible conditions, the results obtained from the 16 volunteers that participated in the study are presented in Figure 4 and Table 2. For back flexion, an average angle of 16.88° and 16.74°, with the standard deviation of 15.94 and 15.81, was measured for the 16 participants using the developed tool and the Goniometer, respectively. The obvious similarity is that the average angular measurements and standard deviation indicate no notable difference in the distribution of the data measured by the developed tool and the Goniometer when tested under reproducibility conditions. The difference in the measurements of 0.15° means and 0.13 S.D. is low, indicating that the two tools' angular measurement is small and consistent. Kendall's coefficient of concordance (w) of 0.989 ($p = 0.013$) was obtained, showing an excellent level of agreement between the developed tool's measured data and the Goniometer measured data.

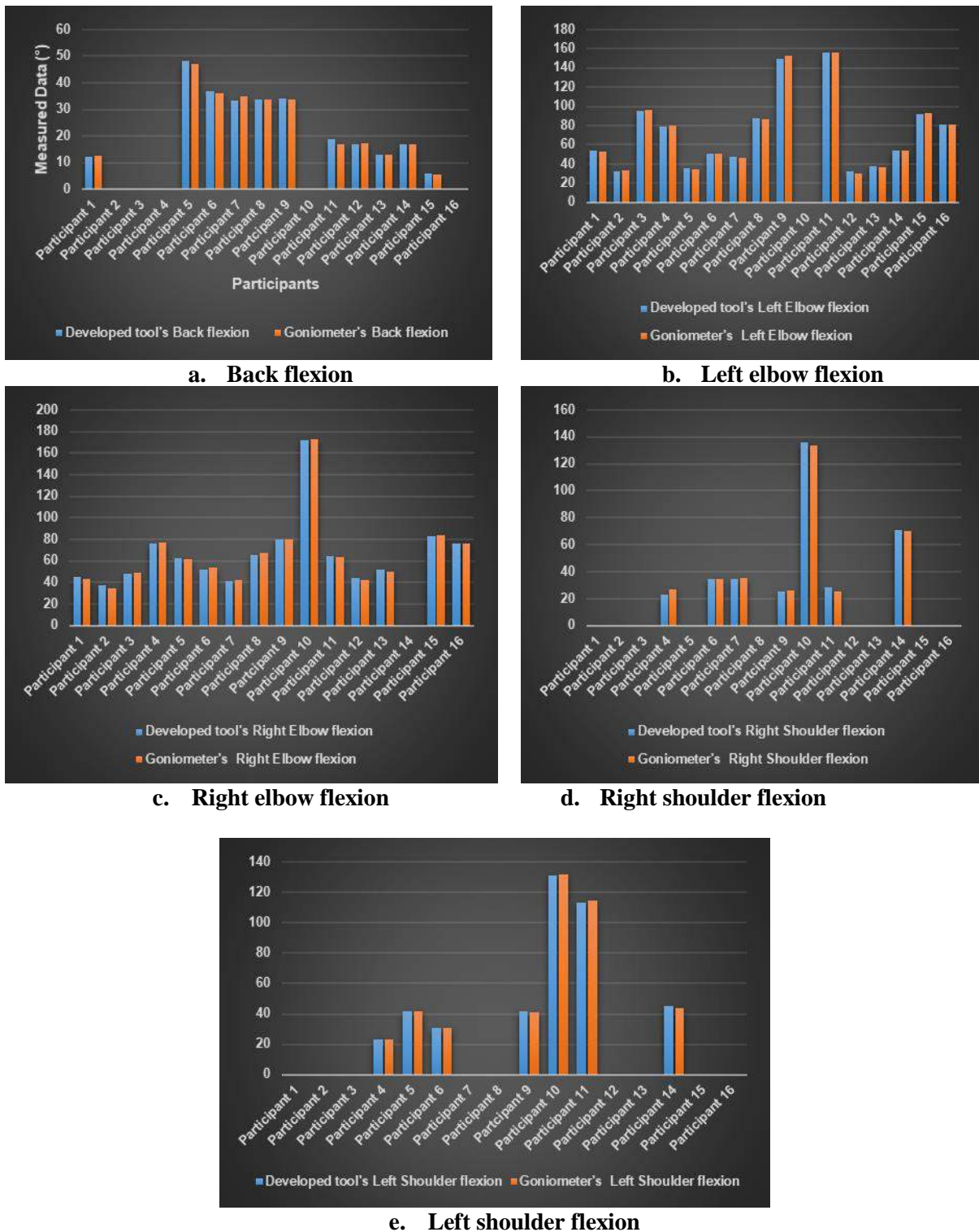


Figure 4: Developed tool vs. Goniometer's measured posture data of different participants under reproducibility conditions.

Table 2: Results of statistical analysis of the data measured under reproducibility conditions

Posture	Mean (°) & S.D. for new tool's measurement	Mean (°) & S.D. for Goniometer measurement	Difference Mean (°) & Difference in S.D.	Kendall's Coefficient of Concordance (w)	P-value
Back Flexion	16.88 & 15.94	16.74 & 15.81	0.15 & 0.13	0.989	0.013
Left Elbow Flexion	67.75 & 42.27	67.71 & 42.84	0.04 & 0.57	0.999	0.012

Right Elbow Flexion	62.57 & 35.73	62.52 & 36.15	0.06 & 0.42	1	0.012
Left Shoulder Flexion	26.70 & 41.34	26.64 & 41.55	0.06 & 0.21	1	0.012
Right Shoulder Flexion	22.13 & 36.70	22.00 & 36.12	0.13 & 0.57	0.993	0.013

** & Separates the Mean from the Standard Deviation

The left elbow flexion, an average angle of 67.75° and 67.71°, with the standard deviation of 42.27 and 42.84, was measured for the 16 participants using the developed tool Goniometer, respectively. Despite the large spread in the measured data as indicated by the large quantity of S.D., there is an obvious similarity in the average angular measurements and standard deviation, indicating no notable difference in the distribution of the data measured by the developed tool and the Goniometer, when tested under reproducibility conditions. The difference in the measurements of 0.04° mean and -0.57 S.D. is low, indicating that the angular measurement between the two tools is small and consistent. Kendall's coefficient of concordance of 0.999 ($p = 0.012$) was obtained, showing an excellent level of agreement between the developed tool's measured data and the Goniometer measured data.

For right elbow flexion, an average angle of 62.57° and 62.52°, with the standard deviation of 35.73 and 36.15, was measured for the 16 participants using the developed tool and the Goniometer, respectively. Despite the large spread in the measured data as indicated by the large quantity of S.D., there is an obvious similarity in the average angular measurements and standard deviation, indicating no notable difference in the distribution of the data measured by the developed tool and the Goniometer, when tested under reproducibility conditions. The difference in the measurements of 0.06° mean and -0.42 S.D. is low, indicating that the angular measurement between the two tools is small and consistent. Kendall's coefficient of concordance of 1 ($p = 0.012$) was obtained, showing an excellent level of agreement between the developed tool's measured data and the Goniometer measured data.

Also, for left shoulder flexion, an average angle of 26.70° and 26.64°, with the standard deviation of 41.34 and 41.55, was measured for the 16 participants using the developed tool and the Goniometer, respectively. Despite the large spread in the measured data as indicated by the large quantity of S.D., there is an obvious similarity in the average angular measurements and standard

deviation, indicating no notable difference in the distribution of the data measured by the developed tool and the Goniometer, when tested under reproducibility conditions. The difference in the measurements of 0.06° mean and -0.21 S.D. is low, indicating that the angular measurement between the two tools is small and consistent. Kendall's coefficient of concordance of 1 ($p = 0.012$) was obtained, showing an excellent level of agreement between the developed tool's measured data and the Goniometer measured data.

For right shoulder flexion, an average angle of 22.13° and 22.00°, with the standard deviation of 36.70 and 36.12, was measured for the 16 participants using the developed tool and the Goniometer, respectively. Despite the large spread in the measured data as indicated by the large quantity of S.D., there is an obvious similarity in the average angular measurements and standard deviation, indicating no notable difference in the distribution of the data measured by the developed tool and the Goniometer, when tested under reproducibility conditions. The difference in the measurements of 0.13° means and 0.57 S.D. is low, indicating that the two tools' angular measurement is small and consistent. Kendall's coefficient of concordance of 0.993 ($p = 0.013$) was obtained, showing an excellent level of agreement between the developed tool's measured data and the Goniometer measured data.

Finally, the analysis results indicate little notable angular discrepancies in the data measured by the developed tool and the reference tool. Comparing the data measured with the two tools, it is obvious that there is a great consistency. This is further validated by the intraclass correlation coefficient and Kendall's coefficient of concordance values, which suggest excellent levels of agreement and consistency in the data measured by the two tools. Hence, the developed tool proved to be reliable and consistent in its measurement.

4. CONCLUSION

Several posture assessment tools have been developed, but these often require an assessment to be carried out by observing several operations and

carrying out analysis afterward. A real-time automatic health and safety posture assessment tool developed by [12], [27] was tested in this study. The new tool is an automatic, portable, cost-effective tool that detects and assesses work postures with real-time feedback to the workers and their employers. It consists of a Microsoft Kinect 3D motion sensor and a developed software application for retrieving posture data from the 3D motion sensor. The tool's statistical test under repeatability and reproducibility conditions, presented in this study, suggests satisfactory agreement and consistency levels in the data measured by the developed tool. Hence, the developed tool proved to be reliable and consistent in its measurement. The tool's benefit is its usefulness in the automatic real-time detection and assessment of work postures, promoting a reduction in the rate of occurrence of awkward postures and, consequently, the risk of MSDs among workers in the workplace.

ACKNOWLEDGMENT

The author would like to acknowledge the Petroleum Technology Development Fund, PTDF Nigeria, for sponsoring her Ph.D. from which this paper is derived.

CONFLICT OF INTEREST

There is no conflict of interest associated with this work.

REFERENCES

- [1] HSE, "ART tool: Posture," 2015. .
- [2] OSHA-Heavy Lifting, "Ergonomics eTool: Solutions for Electrical Contractors - Materials Handling: Heavy Lifting." .
- [3] OSHA Technical Manual, "OSHA Technical Manual (OTM) | Section VII: Chapter 1 - Back Disorders and Injuries | Occupational Safety and Health Administration." .
- [4] OSHA - Hazard Index, "Ergonomics eTool: Solutions for Electrical Contractors - Supplemental Information: Hazard Index." .
- [5] U. Steinberg, "New tools in Germany: development and appliance of the first two KIM ("lifting, holding and carrying" and 'pulling and pushing') and practical use of these methods," *Work*, vol. 41, pp. 3990–3996, 2012.
- [6] WSH (Workplace Safety and Health) Council, "Workplace Safety and Health Guidelines Improving Ergonomics in the Workplace," Workplace Safety and Health Council in collaboration with the Ministry of Manpower., 2014.
- [7] C. E. Mgbemena, A. Tiwari, Y. Xu, V. Prabhu, and W. Hutabarat, "Ergonomic evaluation on the manufacturing shop floor: A review of hardware and software technologies," *CIRP J. Manuf. Sci. Technol.*, vol. 30, pp. 68–78, Aug. 2020.
- [8] C. E. Mgbemena *et al.*, "Gesture Detection Towards Real-Time Ergonomic Analysis for Intelligent Automation Assistance," in *Advances in Ergonomics of Manufacturing: Managing the Enterprise of the Future*, C. Schlick and S. Trzeciński, Eds. Switzerland: Springer International Publishing, 2016, pp. 217–228.
- [9] A. Naddeo, N. Cappetti, and C. D'Oria, "Proposal of a new quantitative method for postural comfort evaluation," *Int. J. Ind. Ergon.*, vol. 48, pp. 25–35, 2015.
- [10] W. Chu, S. Han, X. Luo, and Z. Zhu, "Monocular Vision-Based Framework for Biomechanical Analysis or Ergonomic Posture Assessment in Modular Construction," *J. Comput. Civ. Eng.*, vol. 34, no. 4, p. 04020018, Jul. 2020.
- [11] F. Scotto di Luzio, C. Lauretti, F. Cordella, F. Draicchio, and L. Zollo, "Visual vs vibrotactile feedback for posture assessment during upper-limb robot-aided rehabilitation," *Appl. Ergon.*, vol. 82, p. 102950, Jan. 2020.
- [12] C. E. Mgbemena, J. Oyekan, W. Hutabarat, Y. Xu, and A. Tiwari, "Design and implementation of ergonomic risk assessment feedback system for improved work posture assessment," *Theor. Issues Ergon. Sci.*, vol. 19, no. 4, pp. 431–455, Oct. 2018.
- [13] J. A. Diego-Mas and J. Alcaide-Marzal, "Using Kinect™ sensor in observational methods for assessing postures at work," *Appl. Ergon.*, vol. 45, no. 4, pp. 976–985, 2014.
- [14] J. Sanjog, T. Patel, A. Chowdhury, and S. Karmakar, "Musculoskeletal ailments in Indian injection-molded plastic furniture manufacturing shop-floor: Mediating role of work shift duration," *Int. J. Ind. Ergon.*, vol. 48, pp. 89–98, 2015.
- [15] A. D. Pinder, "Benchmarking of the Manual Handling assessment Charts (MAC)," 2002.
- [16] L. McAtamney and E. Nigel Corlett, "RULA: a survey method for the

- investigation of work-related upper limb disorders.," *Appl. Ergon.*, vol. 24, no. 2, pp. 91–9, Apr. 1993.
- [17] H.-S. Park, J. Kim, H.-L. Roh, and S. Namkoong, "Analysis of the risk factors of musculoskeletal disease among dentists induced by work posture.," *J. Phys. Ther. Sci.*, vol. 27, no. 12, pp. 3651–4, Dec. 2015.
- [18] P. Mukhopadhyay, D. Jhodkar, and P. Kumar, "Ergonomic risk factors in bicycle repairing units at Jabalpur.," *Work*, vol. 51, no. 2, pp. 245–54, Jun. 2015.
- [19] C. Wiktorin, M. Mortimer, L. Ekenvall, A. Kilbom, and E. W. Hjelm, "HARBO, a simple computer-aided observation method for recording work postures.," *Scand. J. Work. Environ. Health*, vol. 21, no. 6, pp. 440–9, Dec. 1995.
- [20] D. Kee and W. Karwowski, "A Comparison of Three Observational Techniques for Assessing Postural Loads in Industry," *Int. J. Occup. Saf. Ergon.*, vol. 13, no. 1, pp. 3–14, Jan. 2007.
- [21] R. a Clark *et al.*, "Validity of the Microsoft Kinect for assessment of postural control.," *Gait Posture*, vol. 36, no. 3, pp. 372–7, Jul. 2012.
- [22] J. L. P. do Rosário, "Biomechanical assessment of human posture: A literature review," *J. Bodyw. Mov. Ther.*, vol. 18, no. 3, pp. 368–373, 2014.
- [23] I. Åkesson, I. Balogh, and G.-Å. Hansson, "Physical workload in neck, shoulders and wrists/hands in dental hygienists during a work-day.," *Appl. Ergon.*, vol. 43, no. 4, pp. 803–11, Jul. 2012.
- [24] A. B. Cunha *et al.*, "Assessing the Validity and Reliability of a New Video Goniometer App for Measuring Joint Angles in Adults and Children," *Arch. Phys. Med. Rehabil.*, vol. 101, no. 2, pp. 275–282, Feb. 2020.
- [25] C. D. McKinnon, M. W. Sonne, and P. J. Keir, "Assessment of Joint Angle and Reach Envelope Demands Using a Video-Based Physical Demands Description Tool," *Hum. Factors J. Hum. Factors Ergon. Soc.*, p. 001872082095134, Sep. 2020.
- [26] T. Dutta, "Evaluation of the Kinect™ sensor for 3-D kinematic measurement in the workplace.," *Appl. Ergon.*, vol. 43, no. 4, pp. 645–9, Jul. 2012.
- [27] C. E. Mgbemena, J. Oyekan, W. Hutabarat, S. Fletcher, Y. XU, and A. Tiwari, "Optimum Kinect Setup for Real-Time Ergonomic Risk Assessment on the Shop Floor," in *Contemporary Ergonomics and Human Factors 2017*, 2017th ed., J. Charles, Rebecca & Wilkinson, Ed. London, UK: Chartered Institute of Ergonomics and Human Factors, 2017, pp. 265–272.
- [28] T. K. Koo and M. Y. Li, "A Guideline of Selecting and Reporting Intraclass Correlation Coefficients for Reliability Research.," *J. Chiropr. Med.*, vol. 15, no. 2, pp. 155–63, Jun. 2016.



An Open Access Journal Available Online

Development and Performance Evaluation of a Household Liquefied Petroleum Gas Monitoring and Leakage Detector

B. J. Olorunfemi^{1*}, D. E. Adenuga¹, and A. E. Olumilua¹

¹Mechanical Engineering Department, Federal University Oye Ekiti, Nigeria

²Agricultural and Environmental Engineering Department, Federal University of Technology Akure, Nigeria

*Corresponding E-mail: bayode.olorunfemi@fuoye.edu.ng +2348036061994

Received: 01.04.2020

Accepted: 27.10.2020

Published: 31.12.2020

Abstract- The percentage of death and material losses as a result of the explosion of household liquefied petroleum gas (LPG) has risen in recent years, hence the need for a suitable gas leaking detection and alert system. Gas level monitoring and leakage detection device consist essentially of two main units; LPG volume monitoring unit and leakage detection unit. LPG volume monitoring unit consists of load cells, HX711 signal amplification module, and infrared temperature sensor. 50 kg E-shaped load cell was used for this work due to its relatively small size, lightweight and ease of installation. The system is powered with 9 volts' battery. The leakage alert mode is triggered by a signal from the gas sensor when the concentration of LPG in the controlled atmosphere is more than the programmed safe value. On entry into this mode, a warning alert is displayed on the screen and the buzzer emits a continuous beep until the level of the LPG falls below the programmed level. A rectangular platform houses the load cells and signal amplification module. The alert system was programmed to produce three short beeps on the start of the device whenever the cylinder volume is less than 0.5 kg. The standard safe allowable concentration of LPG in the atmosphere was put at 1000 ppm (part per million) and once this is exceeded, the system automatically switches to the alert mode. The developed system performs satisfactorily, is safe to use, and therefore recommended for domestic use.

Keywords: Cooking gas, gas cylinder, load cell, microcontroller, monitoring system

1. INTRODUCTION

One of the most common uses of liquefied petroleum gas (LPG) is essentially as a household cooking fuel due to a variety of reasons ranging from being a relatively clean source of fuel compared to biogas and wood to its low greenhouse gas emission rating. It is also a relatively fast and easy means of cooking, providing instant heating at 8-9 times the efficiency of wood. The level of use of LPG has increased worldwide in recent time because of its convenience. It is more comfortable, efficient and heat quickly than the recent technology of biomass stoves. LPG stoves reduce time spent in cooking, could be regulated, easily transportable, and provide a cleaner kitchen [1], [2].

Despite the aforementioned advantages associated with the use of LPG for household cooking, there exist a variety of downsides with its usage as cooking fuel. LPG exists as a colourless, odourless, and highly flammable liquid which readily evaporates into gaseous state. Hence, the addition of odourant to help detect leaks. When there is a leakage, LPG evaporates quickly to form a thick big cloud of gas. And because butane/propane is heavier than air, it falls to the ground level, and it can transport for relatively long distance at ground level [3]. In the process of this displacement, if the gas meets a source of ignition, it will explode because of its volatility. It has been reported that LPG can cause

cold burns to skin. It can lead to loss of consciousness due to the interruption of breathing and subsequent anoxia (as it acts as an asphyxiant) from choking at high concentrations [4], [5].

The issue of explosion or fire hazard resulting from undetected gas leakage from LPG cylinders and pipes has posed to be a very big problem over the years [6]. Different inventions have been made on the way to monitor gas leakage of which gas sensors are introduced to detect any leakage [7], [8]. Sitan and Ghafar [2] worked on detecting gas leakage by using two types of alarm alert, and two sensing unit. This was connected with an online monitoring to alert the user. Apeh et al. [9] also worked on a gas leakage detection device that will alert the subscriber by using alarm system, and automatic gas shut off system. Ramya et al. [10] also implemented a similar design but without the sprinkler. It detected the level of gas concentration in the air, and automatically notified the user when the quantity of gas in the cylinder goes below a set threshold. This will prompt the user it is time to refill [11]. Another researcher carried out some works in the area of detecting gas leakage and monitoring, by introducing cellphone alerts (beep), turning-off of gas supply, and send notification to the user [2]. These developments have broader focus beyond kitchen gas leakages into industrial usage.

This work is aimed at designing and constructing a functional gas level monitoring system for LPG cylinders with an integrated leakage unit for households. This will provide an easy and reliable way for managing and running gas vending business, attain maximum reliability for the effective use of liquefied petroleum gas, and evaluate the performance of the developed device

2. METHODOLOGY

The gas level monitoring and leakage detection device consist essentially of two main units; the LPG volume monitoring unit and the leakage detection unit. The LPG volume monitoring unit consists of load cells, HX711 signal amplification module, and the infrared temperature sensor [12].

2.1 Load Cells

As a transducer, load cell is used to convert compressive force to create an electrical signal with magnitude that can be standardized and be made to be directly proportional to the force being measured. The three main types of load cell are the pneumatic, hydraulic, and strain gauge.

2.1.1 Hydraulic Load Cells

Whenever there is an application of force on a confined space of a liquid medium, the resultant effect is increase in pressure of the liquid medium, which will be directly proportional to the load. This may imply that the applied force is equivalent to the pressure variation of the liquid. Hence, a hydraulic load cells is a force-balance device that measure weight as a change in pressure of the fluid in the confined space. When there is a change in pressure as a result of movement of the piston and the fitted diaphragm, this change in pressure is proportional to the applied force. This increase is measured on a Bourdon pressure gauge connected with the load cells. Figure 1 shows a sketch diagram of a hydraulic load cell.

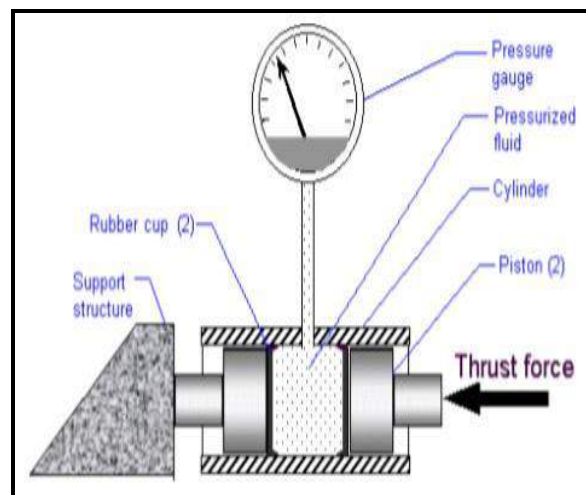


Figure 1: A sketch diagram showing a hydraulic load cell

2.1.2 Pneumatic Load Cells

Air pressure is applied to an elastic diaphragm, and the gas escapes at the bottom of the load cell, which has a pressure gauge inside the cell where the weight will be measured. In other words, the

required air to equal the weight will measure the weight of the object applied while (Figure 2).

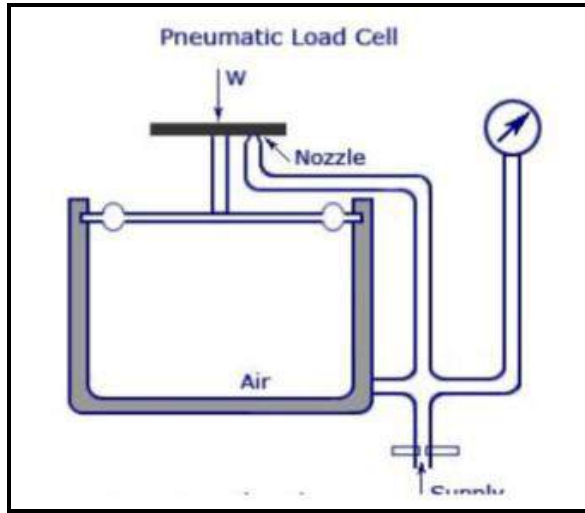


Figure 2: Pneumatic load cell

2.1.3 Strain gauge load cells

Strain gauge load cells resembles the legs of a wheatstone bridge configuration makes use of a mechanical element in which the force is being sensed by the deformation is measured as proportion to the change in the electrical signal of a/or several strain gauge(s) on the element (Figure 3).

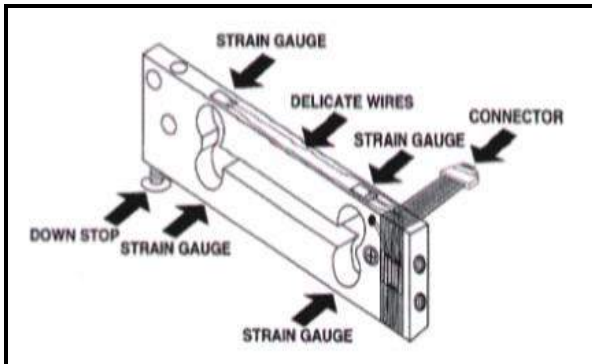


Figure 3: Strain gauge load cells

2.2 Working of the load cell

Today, strain gauge based load cells have become the choice for the applications of industrial weighing. Most load cells use a strain gauge to determine the measurements, the force and the electrical signal it produces. The working of strain gauge load cell is designed as a Wheatstone bridge with two input terminals, it connects four resistors configured in a diamond-like

arrangement in a combination to give a null center value [13], [14]. A Wheatstone bridge circuit is shown in Figure 4 below.

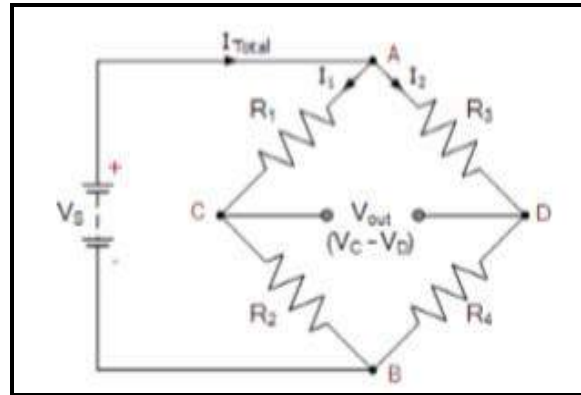


Figure 4: The Wheatstone bridge

The Wheatstone bridge can be determined by connecting the two series strings in parallel and the result of swapping the two resistors is that both sides and arms of the parallel network are different as they produced different voltage drops. At this point, the parallel network is said to be unbalanced as the voltage at point C is at a different value to the voltage at point D (Equation 1);

$$V_{out} = V_C - V_D = (V_C - V_D) = (V_{R2} - V_{R4}) = 0 \tag{1}$$

$$R_C = \frac{R_2}{R_1 + R_2} \tag{2}$$

$$R_D = \frac{R_4}{R_3 + R_4} \tag{3}$$

$$\frac{R_2}{R_1 + R_2} = \frac{R_4}{R_3 + R_4} \tag{4}$$

Where, V_c = Voltage of node C

V_D = Voltage of node D

R_C = Equivalent resistance at node C

R_D = Equivalent resistance at node D

At balance, $R_C = R_D$ (Figure 5) thus,

$$R_2(R_3 + R_4) = R_4(R_1 + R_2) \tag{5}$$

$$R_4 = \frac{R_2 R_3}{R_1} = R_X \tag{6}$$

Figure 5 shows a diagram of how to find unknown resistance (s) with the Wheatstone bridge as presented below;

When R_4 is replaced with a resistance of known value at the Wheatstone bridge sensing arm that has correspondence with R_X , R_3 will also be

adjusted as the opposing resistor, to a balance point, the resultant network outcome of this will be zero voltage output. This balance occurs when (Equation 7);

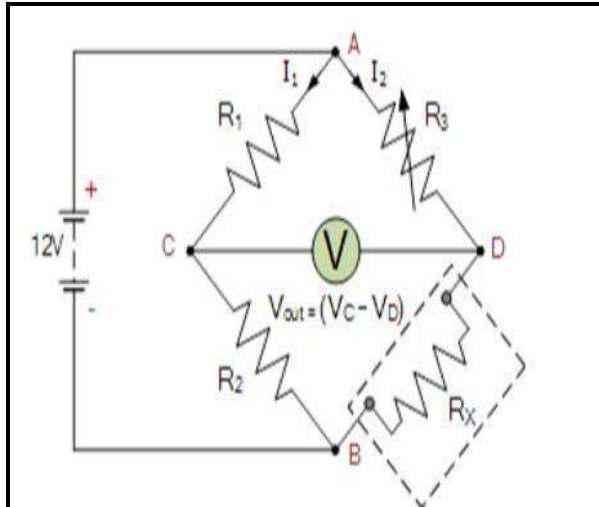


Figure 5: Finding unknown resistance with the Wheatstone bridge

$$R_1/R_2 - R_3/R_4 = 1 \tag{7}$$

And for the calculation of the value of the unknown resistance, R_x at balance can be obtained using Eqn. (2);

$$V_{out} = (V_C - V_D) = (V_{R2} - V_{R4}) = 0$$

Where, resistors, R_1 and R_2 are known or with preset values.

A 50 kg E-shaped load cell is used for this work due to its relatively small size, lightweight and ease of installation. Figure 6 is a flat face load cell for the monitoring of gas cylinder weight. Since most household cylinder are in the range of

5 kg, 6 kg, 25 kg, and 50 kg, A 50 kg E-shape face load cell is used for this work



Figure 6: 50kg flat face load cell

2.3 Hx711 24bit ADC Module

The amplifier module used was based on HX711. It consists of an amplifier and a precision 24-bit analog-to-digital convertor. It was designed for industrial control applications and weigh scale, as it interfaces with the bridge sensor. The input interface of this weight sensor module is used as sensor interface, which is compatible with Arduino input and output ports. The benefits of HX711 24 Bit ADC Module include, fast response, high integration, reliable, economical, and improvement of performance. The output adopts compact terminal that makes weight sensor module easier to connect to the weight sensor [15]. Figure 7 shows the HX711 ADC amplification unit.

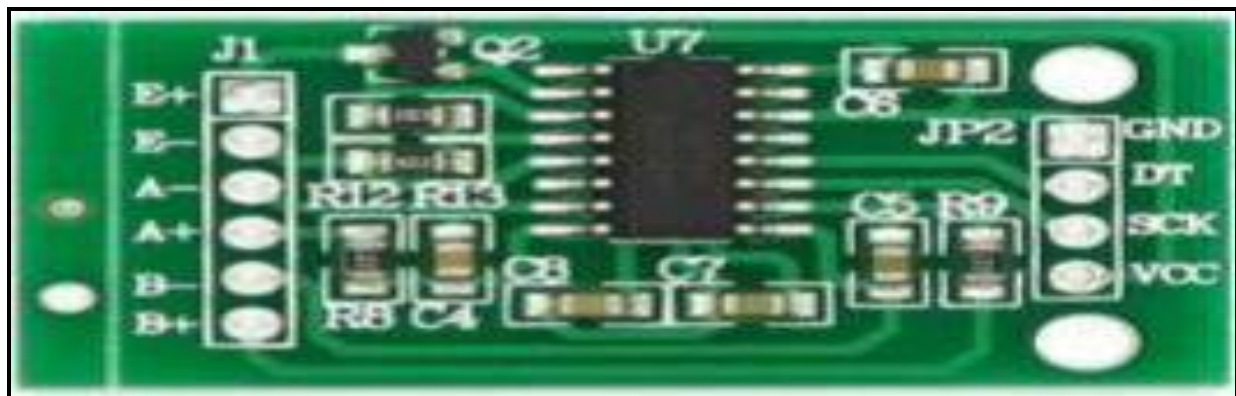


Figure 11: HX711 ADC amplification unit.

2.4 Infrared Temperature Sensing Unit

This unit was incorporated in this design in order to measure the temperature of the cylinder that have been developed as a result of the collision of gas molecules inside the cylinder due to high pressure. An Infrared thermometer sensor. The MLX90614 infrared thermometer used in this work is a non-contact temperature sensing device. Heat is generated inside the gas cylinder due to

collision of gas molecules. This temperature changes in the gas are sensed from the body of the cylinder by the infrared thermometer sensor. The MLX90614 is factory-calibrated in a wide range of temperature capacity; between -40 °C to 85 °C for ambient temperature, and -70 °C to 382 °C for the object temperature [15]. Figure 8 shows the MLX90614 Thermometer sensor.

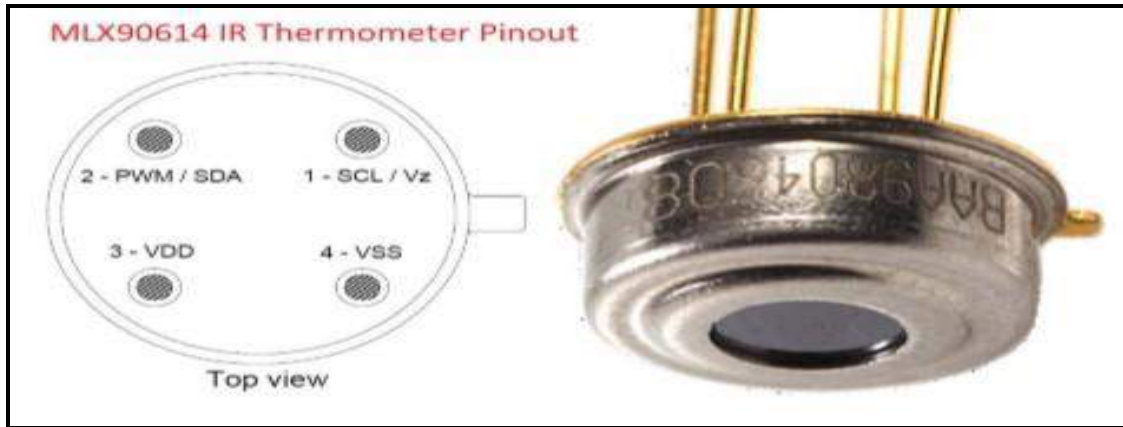


Figure 8: MLX90614 Thermometer sensor

2.5 Sensor Sections

The sensor comprises of the thermopile detector and signal conditioning section. While the thermopile detector converts thermal energy to electrical energy, the signal conditioning section process signal from thermopile detector and make it readable signal to the external peripherals. The sensor contains a strong Digital Signal Processing (DSP) and a 17-bit ADC which have contributed to its high accuracy and resolution., The 17-bit ADC block convert detected signal by the thermopile and calibrate

DSP block quantizes the signal after output signal has travelled through I/O Pulse Width Modulation (PWM) and FC/TWI terminals. 10-bit PWM output provides a resolution of 0.14 °C, and the I²C method gives resolution of 0.02 °C [15]. Figure 9 shows a MLX90614 Thermometer with an attached integrated circuit as presented below; The MLX 90614 thermometer sensor can be directly connected with an alert device, and can be easily made because it is a plug and play device. Figure 10 shows the Infrared-thermal-alarm-circuit.

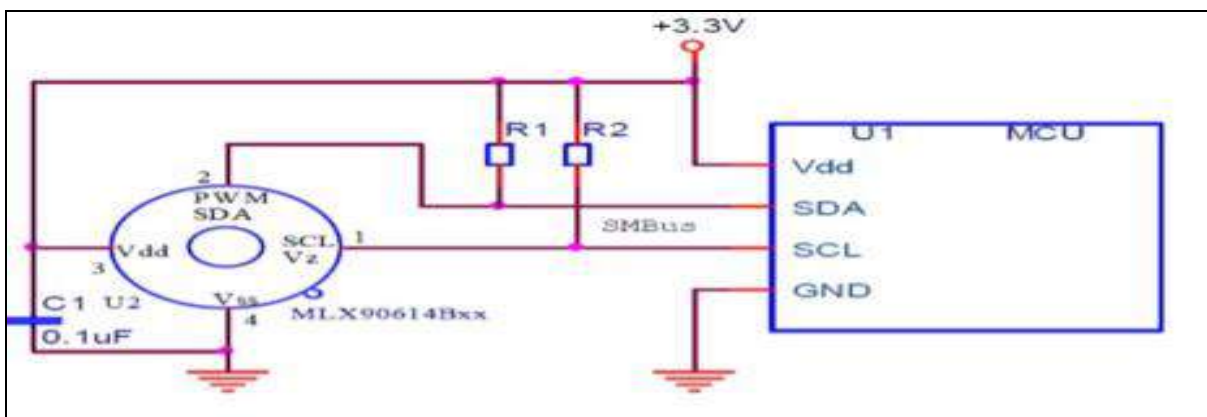


Figure 9: MLX90614 Thermometer with an attached IC.

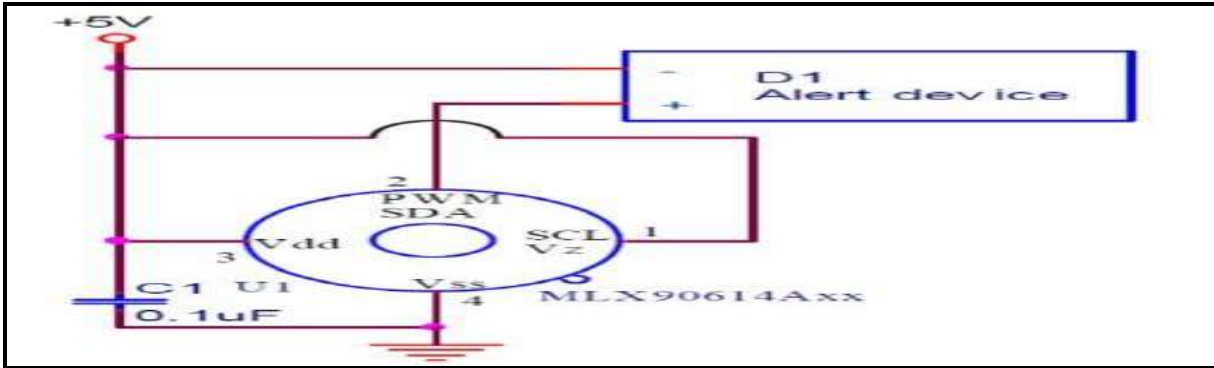


Figure 10: Infrared-thermal-alarm-circuit

2.6 Interfacing MLX 90614:

The MLX 90614 thermometer also has I2C communication lines so that we can interface this sensor with microcontroller without any additional circuits. In the same vein, the microcontrollers have I2C communication way to get interfaced with external peripherals. The sensor operates with 3.3V DC supply. Beetner et al. [16] reported that, if the microcontroller

operates with 5V DC, then there is the need pull up resistors between SDA and SCL lines to +3.3V DC line. The amplifier module is based on HX711, which comprises of an amplifier and a precision 24-bit analog-to-digital convertor designed for weigh scale and industrial control applications, to interface directly with a bridge sensor. Figure 10 shows the interfacing of the MLX 90614 Thermometer with Arduino Nano.

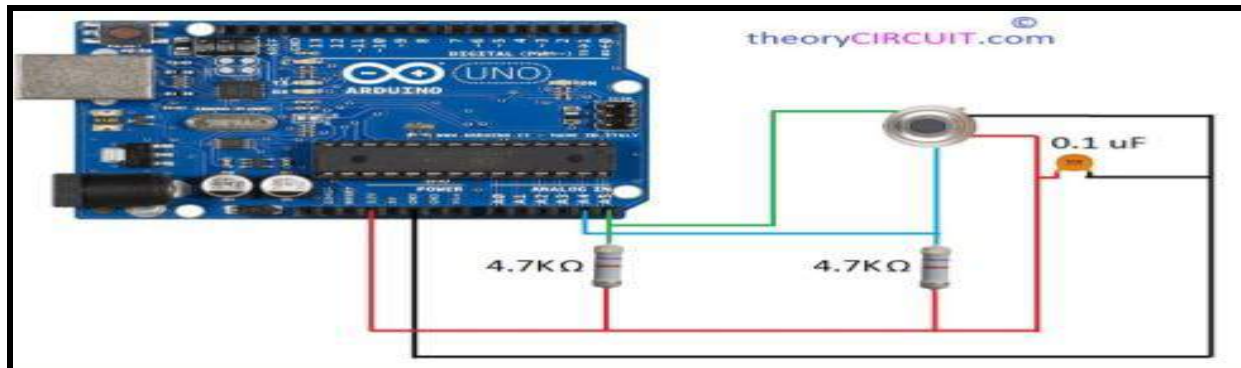


Figure 11: MLX 90614 Thermometer with Arduino

2.7 Leakage Detection Unit

The Leakage Detection Unit consists of the Arduino Nano microcontroller, gas sensor module, and interfaced with control circuits system. This will enable a process to be shutdown automatically. The gas sensor detects the concentration (in ppm) of leaked gas in the surrounding area, this output value is converted to a digital signal through the inbuilt analog to the Arduino Nano microcontroller's digital convertor. The MQ-5 device gas module controls the reading the LPG Gas device module, output, sending message to the LCD and activating of the buzzer. While the function of the circuit once it is

in 'ON' position, it initiates the microcontroller and the show of LCD digital display alphanumeric display, and also begins the reading of the analog voltage rom the MQ-5 device. has four pins [17]. Figure 12 shows a MQ-5 LPG Gas Sensor.

2.8 Arduino Nano Microcontroller

The Arduino Nano is a compacted friendly microcontroller board (Figure 13). The Nano board weighs around 7 grams with dimensions of 4.5 cm to 1.8 cm (L to B) [18]. The choice of Arduino Nano over Arduino Duemilanove and Arduino UNO was because of its specifications and special features (Table 1).

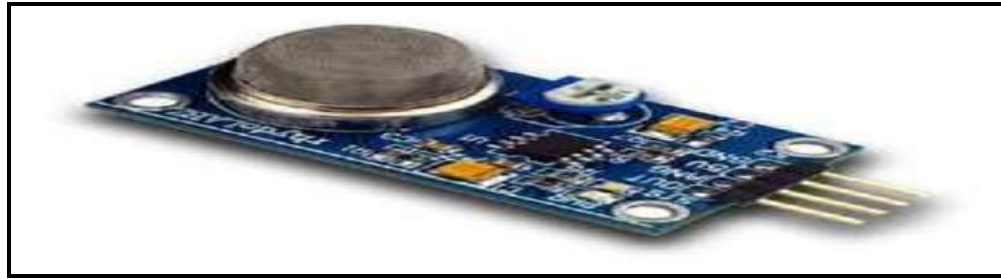


Figure 12: MQ-5 LPG Gas Sensor

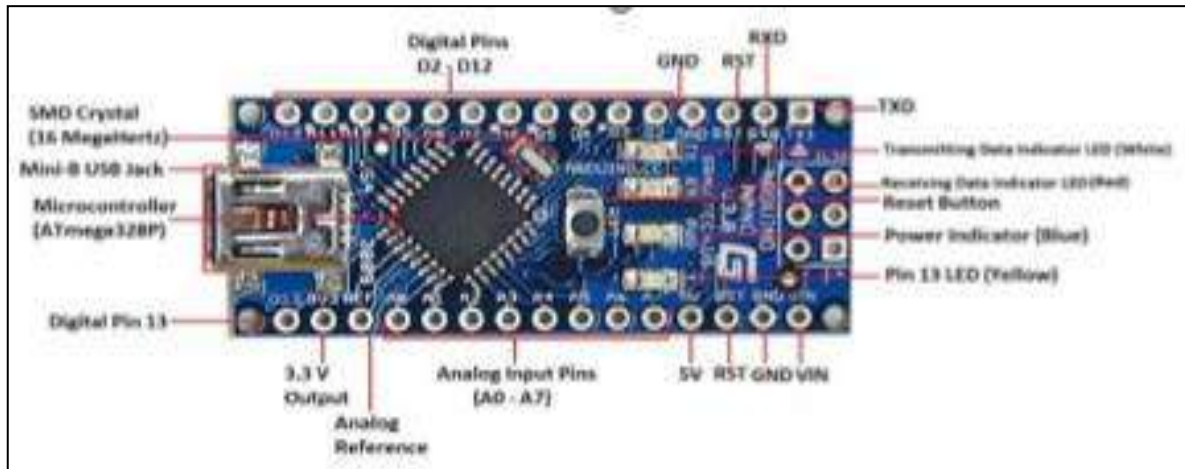


Figure 13: Arduino Nano Microcontrollers

Table 1: The Specifications and Features of Arduino Nano

S/No	Description	Specification
1.	Microcontroller	ATmega328P
2.	Architecture	AVR
3.	Operating Voltage	5 Volts
4.	Flash Memory	32 KB of which 2 KB used by bootloader
5.	SRAM	2 KB
6.	Clock Speed	16 MHz
7.	Analog I/O Pins	8
8.	EEPROM	1 KB
9.	DC Current per I/O Pins	40 milli/Amps
10.	Input Voltage	7-12 Volts

2.9 Liquid Crystal Display (LCD)

LCD is an electronic visual display with flat panel display, that uses the light modulating properties of liquid crystals (Figure 14). Liquid crystals do not emit light directly. According to Rajitha & Swapna (19) reported that LCDs are used in several areas of applications including aircraft cockpit displays, and signage, computer monitors, televisions, and instrument panel.

2.10 Modes of Operation

This mode is used to set the initial weight of a refilled LPG or users gas cylinder;

- This mode can be accessed by pressing and releasing the calibration button for at least 5 seconds after switching on;
- The user is prompted to calibrate the new cylinder;
- The device reads the total weight of the gas cylinder and saves the weight in the EEPROM. The saved weight subsequently

forms the reference weights for computing 'low level'.

The leakage alert mode is triggered by a signal from the gas sensor when the concentration of LPG in the atmosphere is greater than the programmed safe value. On entry into this mode, a warning alert is displayed on the screen and the buzzer emits a continuous beep until the level of LPG falls below the programmed level. For the low volume alert mode, this mode is activated whenever the device is switched on. The volume of gas in the cylinder measured at that point is

compared with calibrated value a "LOW LEVEL" alert accompanied by 3 short beeps from the buzzer is produced whenever the difference in the calibrated value and current values is beneath the programmed value after which the system enters the monitoring mode. While the normal mode (Monitoring mode) is the default mode of the device in which the system continually checks for LPG leakage as well as measure and show the current weight of the gas cylinder in real time as shown in Figure 15.

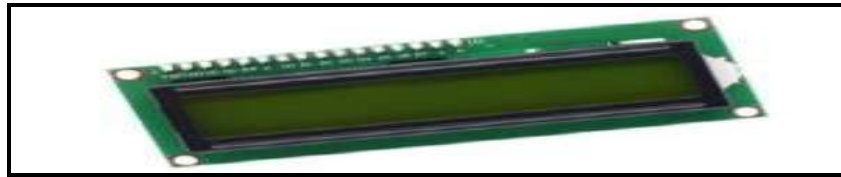


Figure 14 LCD screen 1602

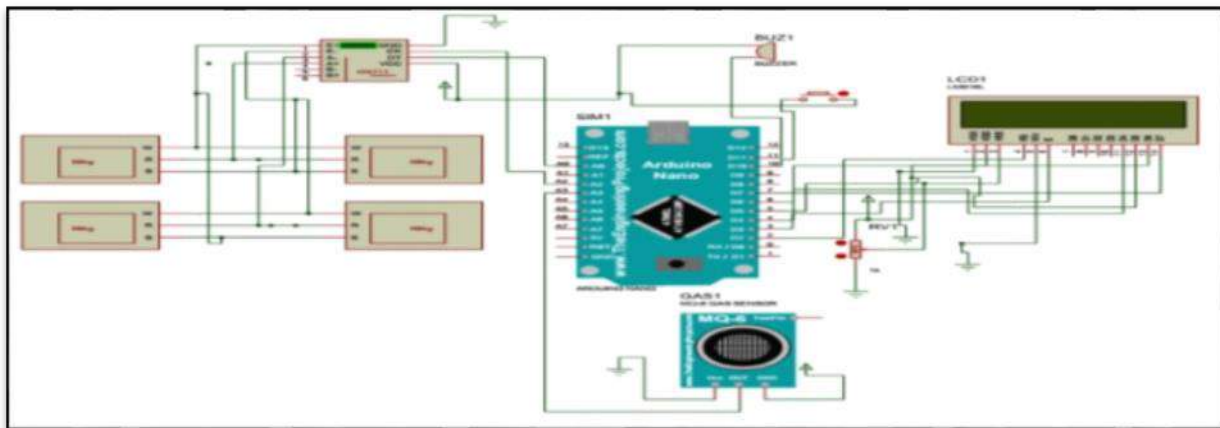


Figure 15: The circuit diagram of auto gas monitoring and leakage detection system.

3. CONSTRUCTION PROCEDURE

The base (rectangular platform) houses the load cells and signal amplification module and essentially provides the platform for the cylinder to be placed while in use. Its dimension was (27 x 27 x 7) cm³ and made of plywood for bottom and top halves, and particle board for the sides (Figure 16). The load cell was arranged in full bridge (4 load cells) and glued to the top half of the plywood and a suitable elevation made of wood for the base of the load cell is provided for the bottom half of the frame as shown in Figure

17. The individual pieces are fastened together via glue and screws to assemble the structure. The control unit consists of the LCD screen (Figures 18-20) an Arduino Nano microcontroller, the control panel, gas sensor and other passive electronic components that made up the control circuit. The casing for the control panel is made from plastic and houses the control circuit. The individual components are soldered to Vero board and the system is powered via a pair of 9v battery [20].

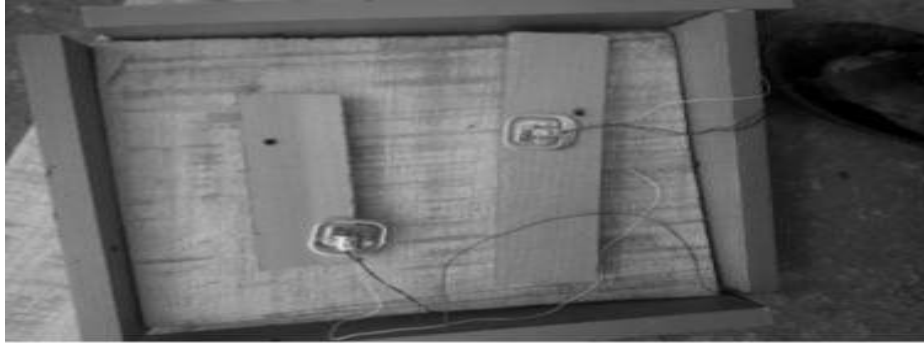


Figure 16: Base (cylinder) platform.

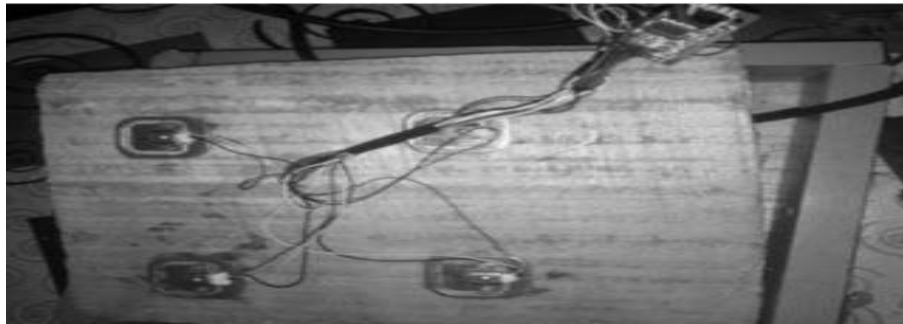


Figure 17: Load cells arranged in full bridge

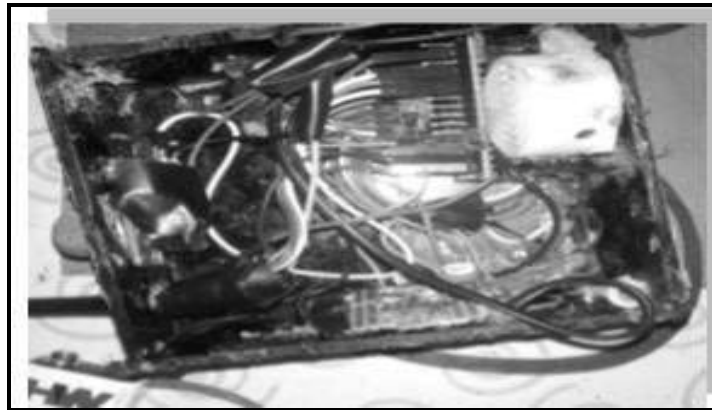


Figure 18: control unit



Figure 19: LCD display



Figure 20: The auto gas monitoring device

4. RESULT AND DISCUSSION

To test for real time measurement weight and low level alert system:

- The device was installed and with the control panel and sensor unit mounted on suitable location from the base,
- An LPG cylinder containing cooking gas was then placed on the platform,
- The calibration button was then pressed down and released to save the initial weight of the cylinder,
- The cylinder was mounted and placed under usage over a period of time and the changes in volume were observed real time.

The alert system was programmed to produce 3 short beeps on start of the device whenever the cylinder volume is less than 0.5 kg. This value is obtained by subtracting the current gas volume

reading from the saved weight or calibrated weight reading. The device was observed to conform to the desired objectives as shown in Figure 21 while Figure 22 shows Performance test of the developed gas monitoring device.

Figure 23 is the graph showing the Relationship between LPG concentration in air and distance covered. Figure 24 indicated the LPG

concentration in air against elapsed time while Figure 25 shows temperature variations with cylinder weight.

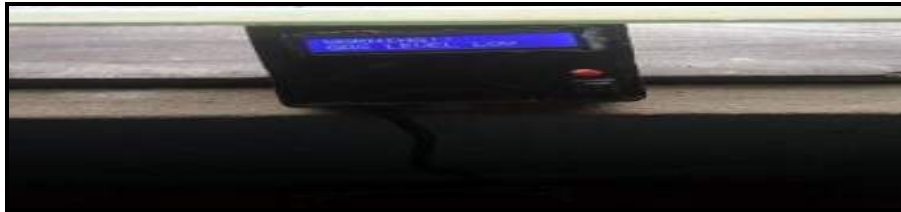


Figure 21: Low LPG level mode

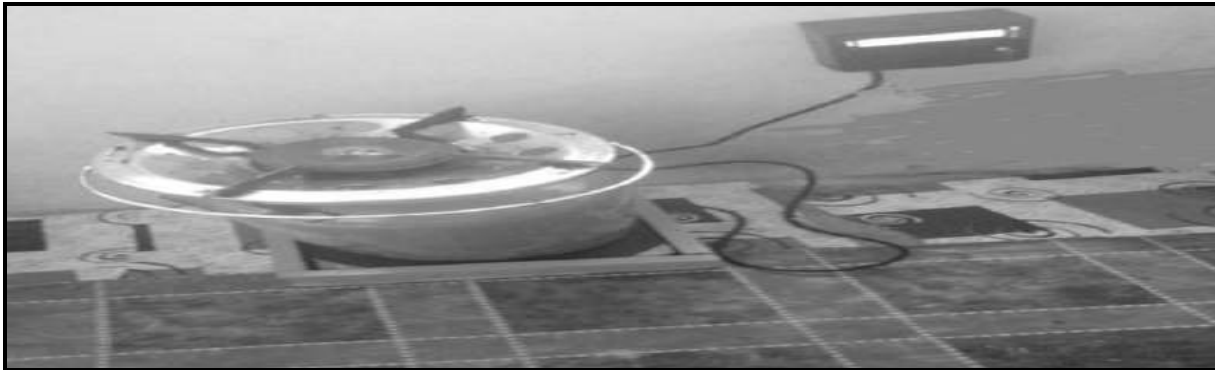


Figure 22: Performance test of the developed gas monitoring device

From Figures 23 and 24 above, it is noted that concentration of LPG in air is inversely proportional to distance moved away from leakage source and time elapse from starting of leakage. It can be seen that the more distant the device is from the leakage, the more time it will take for the device to detect leakage, therefore the device must be close enough to the cylinder

to detect leakage faster. Figure 25 shows the response of the temperature sensor with constant reduction in gas level. They both

slope downward towards the right. This implies that a reduction in gas level causes a decrease in temperature reading on the LCD, which is also a good way to define the quantity of gas in the cylinder Gupta [21].

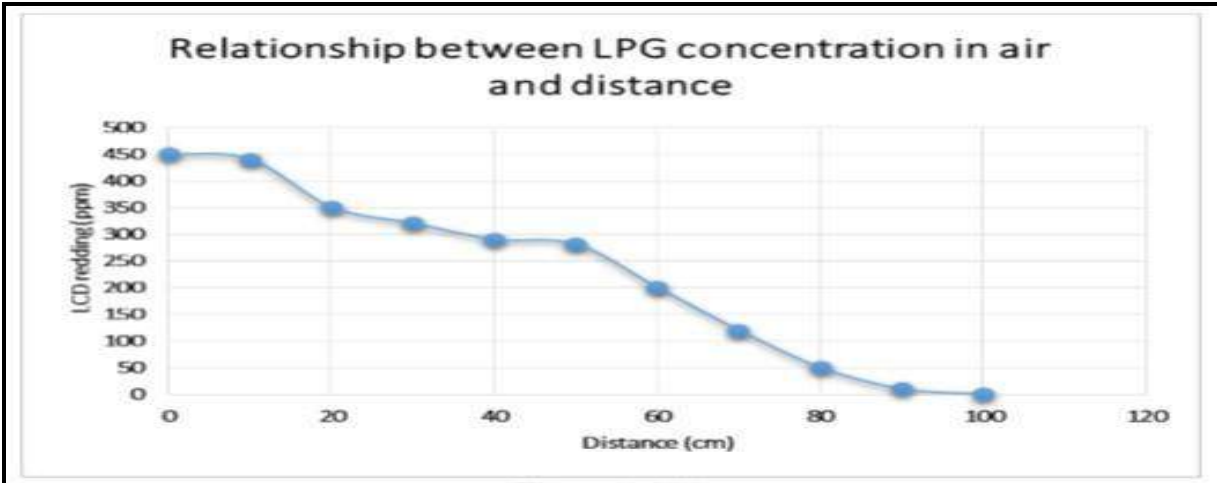


Figure 23: Relationship between LPG concentration in air and distance

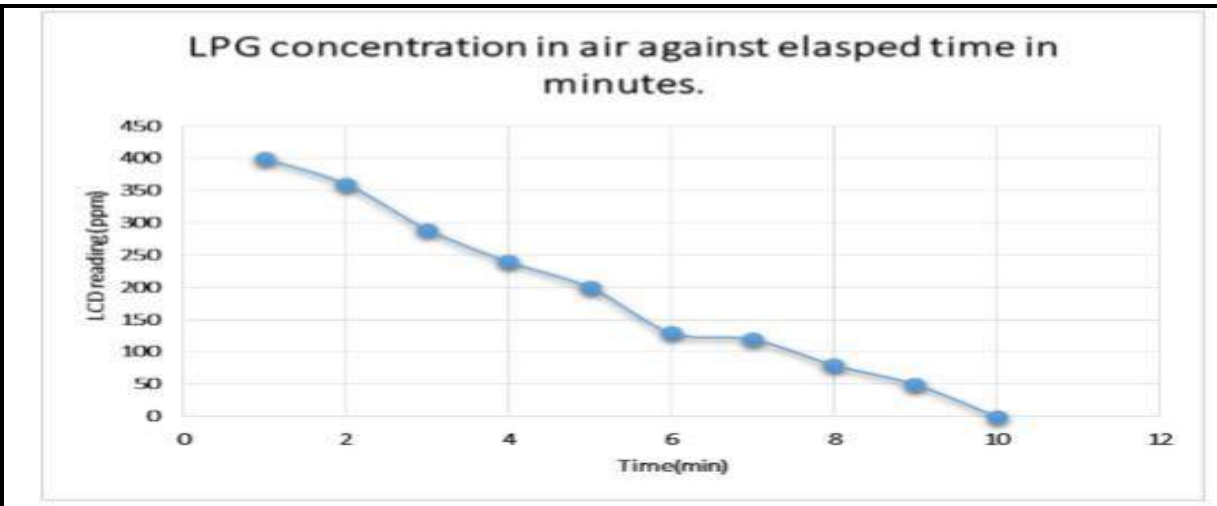


Figure 24: LPG Concentration in air against elapsed time (min)

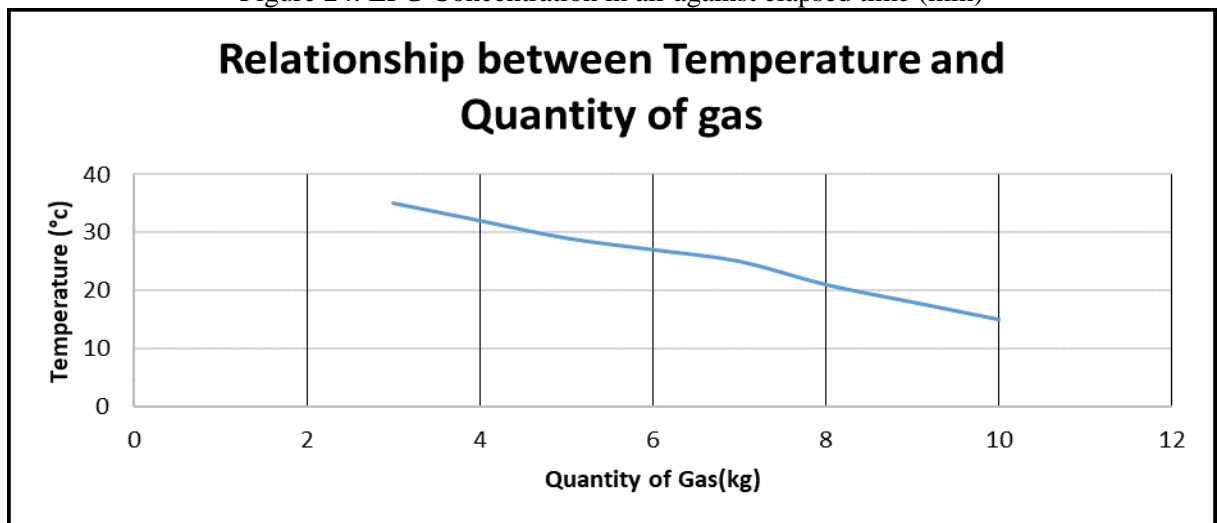


Figure 25: Temperature variations with cylinder mass

5. CONCLUSION

The gas monitoring system here constructed not only measures the weight of an LPG cylinder in real time but also provides a suitable audio-visual alert system for both detections of leakages and low content of LPG cylinders. Results showed that, at 0 cm, LCD reading was 450 ppm, at 50 cm distance, LCD was 281 ppm, while at 100 cm, LCD reading was 0 ppm. The concentration of LPG was 400 ppm in 1min, and 0 ppm in 10 min. While temperature variations with cylinder mass recorded 37 °C at 3.0 kg, and 15 °C at 1.9 kg respectively.

CONFLICT OF INTEREST

There is no conflict of interest associated with this work.

REFERENCES

- [1] Tsado, J., Imoru, O. & Olayemi, S. O. (2014). Design and construction of a GSM-based gas leak alert system. *Int. Res. J. Electr. and Electro. Eng.* **1**(1), aqwrtyt002-006.
- [2] Tamil, S S. & Aim, S. G. (2018) Liquefied Petroleum Gas (LPG) leakage detection and monitoring system, *J. Sci. and Technol*, **10**(3), 46–53.
- [3] Mokhatab, S., Poe, W. A. & John, Y. M. (2015). Handbook of natural gas transmission and processing (3rd Ed), Gulf Professional Pub. <https://doi.org/10.1016/C2013-0-15625-5>
- [4] Jolhe, B. D., Potdukhe P. A & Gawai, N S. (2013). Automatic LPG booking, leakage detection and real time gas measurement monitoring system, *Int. J. Eng. Res. & Technol.* **2**(4), 1192-1195.
- [5] Nwaobasi, I. & Ponnle, A. (2016). Development of a domestic real time cooking gas level monitoring system, 3rd Int. Eng. Conf., Federal University of Technology, Akure, Nigeria, 366-379.
- [6] Tanvira, I. D., Jyotirmoy, S., Jyotirmoy, D. & Rajkumar, S. (2014). GSM Based gas leakage warning system. *Int. J. Adv. Res. in Comput. and Communic Eng.*, **3**(4), 6293-6298.
- [7] Shrivastava, A., Prabhaker, R., Kumar, R. & Verma, R. (2013). GSM based gas leakage detection system, *Int. J. of Emerg. Trends in Electr. and Electro.* **3**(2), 558-563.
- [8] Soundarya, T., Anchitaalagammai, J. V., Deepa Priya, G. & Karthick kumar, S. S. () C-Leakage: cylinder LPG gas leakage detection for home safety, *J. Electro. and Communic. Eng.* **9**(1), 53-58.
- [9] Apeh, S. T., Erameh, K. B. & Iruansi, U. (2014). Design and development of kitchen gas leakage detection and automatic gas shut off system, *J. Emerg. Trends in Eng. and Applied Sci.*, **5**(3), 222-228.
- [10] Ramya, V. & Palaniappan, B. (2012). Embedded system for hazardous gas detection and alerting. *Int. J. Distrib. and parallel syst.* **3**(3), 287-300.
- [11] Jebamalar Leavline E, Asir Antony Gnana Singh, D, Abinaya B, Deepika H. (2017). LPG Gas leakage detection and alert system. *Int. J. Electro. Eng. Res.* **9**(7), 1095-1097.
- [12] Shrivastava, A., Prabhaker, R., Rajeev Kumar, R. & Verma, R. (2013). GSM based gas leakage detection system. *Int. J. Emerg. Trends in Electr. and Electro.* **3**(2), 42-45.
- [13] Wheatstone C. (). An account of several new instruments and processes for determining the constants of a voltaic circuit. *Phil. Trans. Roy. Soc. Bd*, **133**(1843), 303-327.
- [14] Hoffmann, K. (1987). An introduction to measurements using strain gages. Hottinger Baldwin Messtechnik GmbH.
- [15] Fradien, J. (2010). Handbook of modern sensors: Physics, designs, and applications. Springer
- [16] Beetner, D., Pottinger, H. & Mitchell, K. (2000). Laboratories teaching concepts in microcontrollers and hardware software co-design. IEEE 30th Annual Conference in Frontiers in Education.
- [17] Haque, M. D., Azimu, S. M. & Nanwal, R. (2014). Cadmium zinc Sulphide Nanoparticles as sensing material for microcontroller based ammonia sensor: Pilot study, *Materials Science Forum*; **781**, 119-126.
- [18] Kleitz, W. (1997). Microprocessor and microcontroller fundamentals: The 8085 & 8051 Hardware and Software. Prentice Hall Professional Technical Reference.
- [19] Rajitha, S. & Swapna, T. (2012). A Security alert system using GSM for gas leakage. *Int. J. VLSI and Embedded Syst.* **3**(4), 173-175.
- [20] Sahu, K. & Mazumdar, M. S G. (2012). Digitally greenhouse monitoring and controlling of system based on embedded system. *Int. J. Scientific & Eng. Res.* **3**(1), 1-4.
- [21] Gupta, A. (2017). Economical and optimal gas leakage detection and alert system. *Int.J. of Scientific and Res. Pub.* **7**(11), 260-263.



An Open Access Journal Available Online

Load-ability Analysis during Contingency with Unified Power Flow Controller Using Grey Wolf Optimization Technique

Yusuf Samuel Sunday*, Okorie Patrick Ubeh, Abubakar Adamu Saidu, Momoh Illiasu Onimisi & Jimoh Boyi

Department of Electrical Engineering, Ahmadu Bello University, Zaria, Nigeria
yusufssamuel@gmail.com

Received: 03.04.2020

Accepted: 09.11.2020

Published: 31.12.2020

Abstract: Voltage stability enhancement with optimal placement of a unified power flow controller considering load-ability analysis is investigated in this paper. It is essential, because when voltage instability is left unattended, it leads to voltage collapse and, consequently, in a partial or total blackout of the whole network resulting from cascading effect. The optimization process is achieved by increasing the percentage load demand index to the maximum load-ability and under single contingency. This method will be of great benefits to bulk dispatcher of power to plan ahead of how to wheel and deliver power to the end-users during both normal and contingency conditions at the least cost and time. A grey wolf optimization technique is utilised to find the optimal location and sizing of UPFC on the network. The line's voltage stability and load margin are then evaluated with and without UPFC under different loading conditions using optimal power flow technique. The approach's effectiveness is carried out on 31-bus, 330kV Nigeria National Grid (NNG) based on two scenarios: load-ability analysis under maximum loading of the network and load-ability analysis under single contingency. The results show that power can be transmitted to meet the growing energy demand over an existing network during normal and contingency conditions without violating voltage stability by making use of the proposed method in this paper.

Keywords: Grey Wolf Optimization, Line Load-ability, Maximum Loading, UPFC, Voltage Stability

1. INTRODUCTION

Electrical energy is a crucial ingredient for a country's economic and industrial development; hence, there is an endless demand for this energy [1]. So, it is of central importance for the power industry to guarantee the continuity of a stable, secure, economic, efficient, and reliable power supply at all times. With the rising demand for electrical energy, coupled with population growth and recursive increase in technological development under contingency and restructured market environment, inevitably that voltage instability, line congestion, power losses, frequency collapse, and transient instability will exist on the network [2, 3]. Due to these challenges, transmission lines are being operated closer or beyond their stability limit and the emergence of other associated limits that lead to power system instability [4, 5]. Confronted with these challenges and constraints, power system engineers have been struggling to develop a new and robust device that can deal successfully and swiftly with these constraints limiting network

capacity and provides power improvement options. The need to install a robust device in an existing transmission asset to provide an effective, efficient, economic, and environmental friendly way of improving transmission line's power carrying capacity is of utmost importance [6]. This essential task has led to the introduction of advanced power electronics based converters known as Flexible Alternating Current Transmission System (FACTS).

FACTS devices are used to alleviate line congestion, increase power transfer capacity, enhance system security and make power transfers fully controllable by controlling all three power flow parameters, namely, line impedance, voltage magnitude and phase angle [6, 7]. Over the years, these devices have brought to bear new perceptions that network instability and constraints can be solved successfully and promptly. Among the various known FACTS devices, Unified Power Flow Controller (UPFC) is the mostly commonly used, because of its uniqueness to independently and

simultaneously provides a super control and regulation of the magnitude of the bus voltage, and power flow via the line where it is attached [8, 9]. Due to the high cost of procuring and installing the FACTS devices, an adequate plan should be geared towards placing it at an appropriate location. FACTS devices' performance depends significantly on the network's location and size [6]. Combining FACTS devices and optimization techniques are the leading method used in modern power systems to curtail and alleviate line congestion efficiently. In this paper, GWO is deployed to locate the best position and sizing of UPFC on 31-bus, 330kV NNG. It is used because of its flexibility, scalability and exceptional ability to balance between the exploration and exploitation in unknown search spaces to give a favourable result and convergence. UPFC is optimally placed on the network to alleviate congestion, power loss reduction, and improved stability of the network etc.

2. THE 31-BUS, 330KV NIGERIA NATIONAL GRID

The 31-bus, 330kV Nigeria National Grid used for this analysis consists of seven (7) generator buses (PV), twenty-four (24) load buses (PQ), and thirty-seven (37) transmission lines. It comprises 6,000km of 132kV lines, 5,000km of 330kV lines, 23km of 330/132kV substations, and 91km of 132/33kV. The following challenges characterize these networks; long transmission lines, fragile grid network, technical hitches of wheeling energy produced from the generating point to the load centers, single and radial circuit network, frequent system collapse, improper configuration of the network, aging and obsolete facilities, overloading, thermal limits violation and poor voltage profile, and lack of ability to regulate some transmission line parameters such as; voltage, and frequency [10]. Technically, these challenges bedeviling NNG can be eliminated by constructing additional generating units and transmission capacity to meet the rising demand to boost the system reliability and stability. However, economic, political, environmental impacts, and construction time have made these measures not to be anticipated. These problems have strongly demanded the optimization and upgrading of the existing network capacity to enable more power transmission during normal and contingency conditions without violating network voltage stability [11-14]. This paper presents a combination of the FACTS device (UPFC) and GWO optimization technique to solve the numerous challenges facing NNG.

2.1 Line Load-ability

Line load-ability is defined as the optimal power transfer capability of a transmission line under a predefined set of operating conditions [15]. Load-ability analysis examines the loading and operating conditions of the network [14]. This analysis estimates the peak power that a transmission line can withstand and permit to flow through it and also reveals various region of the network that can still serve extra loads. Since voltage quality limit affects the power-carrying capacity up to a substantial lengths of the transmission line. In analysing the load-ability of a network, it has been established that there will be areas that will be lightly loaded and can still accommodate additional loads, in contrast, some areas will be heavily loaded, and thereby pressing the network to be operating closer or beyond their stability limit [16]. The following factors limit the loading capacity of a transmission line: voltage-drop, thermal, and steady-state stability limits. Others are voltage stability margin, voltage quality limit, and joule losses limit [17]. The voltage-drop limit is a function of line loading and line characteristics. In contrast, thermal limit depends on the line characteristics and metrological condition of the network location and the steady-state stability reliant on the power system's line characteristics and characteristics of the power system [15]. These issues and other factors result in network voltage instability [18, 19]. Voltage instability is normally regarded as a local phenomenon, but its consequences are widely spread, causing many significant blackouts in the country [20]. Voltage collapse and line overload are still the principal threats to the transmission system [21].

3. MODELLING OF THE UNIFIED POWER FLOW CONTROLLER

The unified power flow controller was first proposed in 1991 by Gyugi [22]. It comprises two switches based on the voltage source converter valves; shunt (exciting-transformer) and series (boosting-transformer), as shown in Fig. 1. Both the exciting and boosting transformers are connected by a standard DC voltage link, signified by the capacitor and two-gate turn off (GTO) converters. Converter 1 (shunt) is connected in parallel to a local bus to be improved through an exciting transformer. This provides the active power needed by Converter 2 at the terminal of the common DC voltage link from the network alternating the local bus's current power system. It also serves as both generator and absorber of reactive power at its AC

terminal that is not dependent on the active power emanating from or to its DC terminal. Converter 1 leverage its ability to offer the role of independent advance static VAR compensator by compensating the transmission line’s reactive power and consequently provides voltage regulation at the UPFC input terminal. Converter 2 is linked in series to a bus via a boosting transformer. It generates source voltage at fundamental frequency with phase angle ($0 \leq \phi_T \leq 2\pi$) and variable amplitude ($0 \leq V_T \leq V_{Tmax}$). The voltage source generated

is coupled to a series-connected boosting transformer to the AC transmission line. Amongst the various FACTS devices, UPFC has an exceptional ability to simultaneously and independently control the three parameters of power flow: voltage magnitude, phase angle, and line impedance. This has made UPFC more versatile and widely used than other FACTS devices. Fig. 1 shows a typical operating principle of UPFC. It depicts the steady-state model of UPFC under different loading conditions.

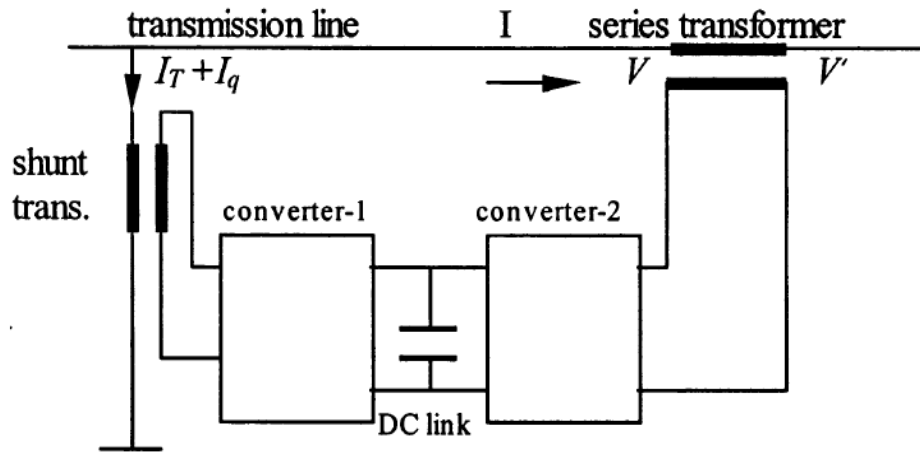


Figure 1: The Operating principle of UPFC [9, 23]

The injected powers (P_{gi} and Q_{gi}) at bus- i along with system loading (λ) is given by (1) and (2):

$$P_i = P_{gi} - P_{di}^0(1 + \lambda) = \sum_{j \in N_h} P_{ij} \quad (1)$$

$$Q_i = Q_{gi} - Q_{di}^0(1 + \lambda) = \sum_{j \in N_h} Q_{ij} \quad (2)$$

Here, active and reactive power demand is represented by P_{di}^0 and Q_{di}^0 . The real and reactive power generated at bus- i is denoted by P_{gi} and Q_{gi} . In equations (1) and (2), an even loading of load buses is considered and to be supplied by swing bus, such that allocation of generation among the generators can easily be done by integrating it into this model [9].

3.1 Grey wolf optimization technique

Based on the grey wolf (*Canis lupus*) social hierarchy and hunting characteristics, a metaheuristic algorithm called Grey Wolf Optimization (GWO) technique was developed by [24] in the year 2014. Wolves belong to the Canidae family and they live in a pack of an average size of 5-10. They are divided into four categories in the order of alpha (α), beta (β), delta (δ), and omega (ω) [25]. Figure 2 shows the leadership pyramid of grey wolves. A male and a female known

as alphas are the leaders of the pack. The alphas with higher dominance are decision-maker of the pack. They are well-endowed with the capacity to control and manage the pack appropriately by commanding the other lower-level wolves. The three main hunting phases are; tracking the prey, encircling the prey, and attacking the prey. Alpha, beta, and delta carry out the hunting for the pack. Alpha is regarded as the best (fittest) solution as a result its superior knowledge of hunting prey. At the same time, beta is the second-best solution, and delta gives the third-best solution, and gamma is the other candidate solutions. This algorithm has shown the ability to balance the exploitation and exploration of problem where the search space is unknown and yields a favourable result at a speedy rate [24].

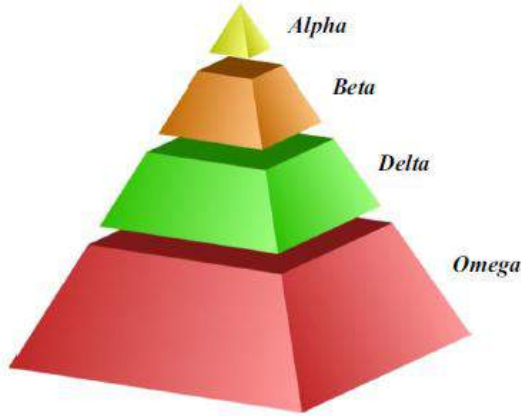


Figure 2: The social hierarchy of grey wolves [26]

(a) *Social Hierarchy*

Social hierarchy is model mathematically by taken alpha (α) as the best (fittest) solution, beta (β) is considered as the second-best solution, and the third-best solution is named delta (δ). In contrast, the other solutions are considered as omega (ω). The optimization technique is controlled by three wolves, namely; alpha, beta, and delta, while omega is just a follower and babysitter in the pack.

(b) *Encircling prey*

The first stage in the hunting behaviour of a wolf is to surround the prey; the mathematical model is given by (3) and (4):

$$\vec{X} = |\vec{A} \cdot \vec{P}_{prey}(t) - \vec{P}(t)| \quad (3)$$

$$\vec{P}(t+1) = \vec{P}_{prey}(t) - \vec{S} \cdot \vec{X} \quad (4)$$

Here; t denotes the current iteration.

\vec{S} and \vec{A} are coefficient vectors,

\vec{P}_{prey} gives the position of the prey, the

position of the prey is denoted by \vec{P} . The vectors \vec{S}

and \vec{A} are mathematical solved using equations (5):

$$\vec{S} = 2\vec{a} \cdot \vec{r}_1 - \vec{a}, \text{ and}$$

$$\vec{A} = 2 \cdot \vec{r}_2 \quad (5)$$

\vec{a} decreases linearly from 2 to 0, while r_1 and r_2 are the random vector between [0, 1]

(c) *Hunting*

Grey wolves can detect the exact location of the prey and circle-shaped it. α is the dominant dominance in the hunt and delta, and beta sometimes participates in the hunting. In order to develop the mathematical modelling of this behaviour, alpha (the fittest candidate solution), beta and delta are presumed to have the best knowledge of the precise (optimum) position of the prey. Hence, the first three best candidate solutions achieved are saved (i.e., α , β and δ), and then the

other search agents, including the omega (ω) positions are updated using (6) and (7):

$$\vec{X}_\alpha = |\vec{A}_1 \cdot \vec{P}_\alpha - \vec{P}|, \vec{X}_\beta = |\vec{A}_2 \cdot \vec{P}_\beta - \vec{P}|, \vec{X}_\delta = |\vec{A}_3 \cdot \vec{P}_\delta - \vec{P}| \quad (6)$$

$$\vec{P}_1 = \vec{P}_\alpha - \vec{S}_1 \cdot (\vec{X}_\alpha) \quad \vec{P}_2 = \vec{P}_\beta - \vec{S}_2 \cdot (\vec{X}_\beta), \quad \vec{P}_3 = \vec{P}_\delta - \vec{S}_3 \cdot (\vec{X}_\delta) \quad (7)$$

$$P_{(t+1)} = \frac{\vec{X}_1 + \vec{X}_2 + \vec{X}_3}{3} \quad (8)$$

4. OPTIMAL POWER FLOW PROBLEM FORMULATION

The power flow problem is optimized to give the optimal setting of the network control variables in order to adequately supply the power demand by minimizing predefined set of objective functions while sustaining the system physical and operational constraints:

Minimization of Real Power Loss

$$\text{Minimize } P_L(x, y) \quad (9)$$

Subject to:- $h(x, y) = 0, \quad g(x, y) \leq 0$

Here, “h” denotes the equality constraints which signify a typical load flow equation and “g” represents inequality (operating) constraints such as; generator voltages, real and reactive power outputs, and shunt compensation.

$$\min P_L = \sum_{k=1}^{N_l} [G_k (V_i^2 + V_j^2 - 2V_i V_j \cos \theta_{ij})] \quad (10)$$

The active power loss is denoted by P_L , G_k represents branch conductance k. V_i and V_j indicate sending and receiving end voltage magnitudes and phase angle between i^{th} and j^{th} bus is signified by θ_{ij} .

Minimization of Voltage Deviation (VD)

This objective function enhances the magnitude of the line voltage by decreasing the voltage deviation on all P-Q buses. This is defined in (11):

$$F_{VD} = \min(VD) = \min\left(\sum_{k=1}^N |V_i - V_j^{ref}|^2\right) \quad (11)$$

Here, V_i is the bus voltage at bus-i and

V_j^{ref} indicates reference voltage limit at bus-j.

Equality Constraints

Active and reactive power equality constraints are given by:

$$0 = P_{Gi} - P_{Di} - V_{Gi} \sum_{j \in N_b} V_j (G_{ij} \cos \theta_{ij} + B_{ij} \sin \theta_{ij}) \quad \text{for } i \in N_b \quad (12)$$

$$0 = Q_{Gi} - Q_{Di} - V_{Gi} \sum_{j \in N_b} V_j (G_{ij} \sin \theta_{ij} + B_{ij} \cos \theta_{ij}) \quad i \in N_b \quad (13)$$

Where N_b denotes total number of buses in a network, P_{Gi} represents total active power generation, P_{Di} is the total power demand, the reactive power generation is Q_{Gi} , Q_{Di} is the reactive power demand, G_{ij} denotes conductance and B_{ij} is susceptance between i^{th} and j^{th} bus.

Operational Inequality Constraints

The voltage, active power, reactive power, transformer and shunt compensator operational inequality constraints for both generator and network are given in terms of lower and upper limits as described below:

$$\begin{aligned} V_{Gi}^{min} &\leq V_{Gi} \leq V_{Gi}^{max} & i \in N_b \\ Q_{geni}^{min} &\leq Q_{geni} \leq Q_{geni}^{max} & i \in N_b \\ P_{geni}^{min} &\leq P_{geni} \leq P_{geni}^{max} & k = 1 \dots, NT \\ T_i^{min} &\leq T_i \leq T_i^{max} & k = 1 \dots, NT \\ Q_{shi}^{min} &\leq Q_{shi} \leq Q_{shi}^{max} & k = 1 \dots, NT \end{aligned}$$

5. RESULTS AND DISCUSSION

This section presents two scenarios: load-ability analysis under maximum loading condition and load-ability analysis under single contingency based on 31-bus, 330kV Nigeria National Grid. This aims to verifying the practicability of this technique at delivering power during both maximum loading and contingency conditions without interruption of supply to consumers. All simulations analyses are done in MATLAB R2017a software using Intel(R) Pentium (R) CPU 2020M with a Dual-Core processor speed of 2.40GHz. The maximum loading occurs at a point where Newton-Raphson has no value (diverged). The network voltage stability is enhanced by the optimal

placement of UPFC on the network using the grey wolf optimization technique.

A. Load-ability Analysis at Critical Loading Condition

Table 1 shows the power flow results of 31-bus, 330kV NNG under an increasing percentage load demand index of 39.72% with and without UPFC at 56th iterations. It is observed that the load growth results in huge power losses in line 33 (7-28) by 11.56MW, followed by line 35(17-19) with 6.89MW loss, and line 36(8-29) increased by 4.89MW respectively when compared to the result under normal condition. This results from the extended distance from the generating unit and the nearer critical lines' cascading effects. A total power loss of 210.7861MW is obtained. After optimal placement and sizing of UPFC device using GWO, the network power loss reduces to 145.4235MW, representing 40.6661% power loss reduction with the installation of UPFC device with a reactive power setting -103.3200MVar at bus 19, the UPFC considerably reduced the total power loss on the network.

Figure 3 shows the voltage profile with and without placing the UPFC device under the network's critical loading. It is observed that bus 28 has a minimum base voltage of 0.9031 p.u due to the considerable distance of the bus from the generating unit. When UPFC was optimally placed on the network, it increases the voltage magnitude to 0.9540p.u. Many of the load buses, especially bus 11, 16, 18, 20, 21, 22, 25, and 29, are the overloaded buses and as such closer to their specified lower boundary of 0.95 p.u, which means any slight rise in the load demand, will result in voltage collapse. However, with the optimal placement of UPFC using GWO at Bus 19, it is observed that the magnitude of the voltage profile increased significantly thereby enhanced the stability margin of the network and allow extra power to be transmitted over the existing network.

Table 1: Power flow result of 31-bus, 330kV Nigeria National Grid at critical loading.

Percentage Loading value	Loss without UPFC (MW)	UPFC Rating (MVar)	Loss with UPFC (MW)	UPFC Location	Percentage Power Loss reduction
39.72	210.7861	-103.3200	145.4235	19	40.6661

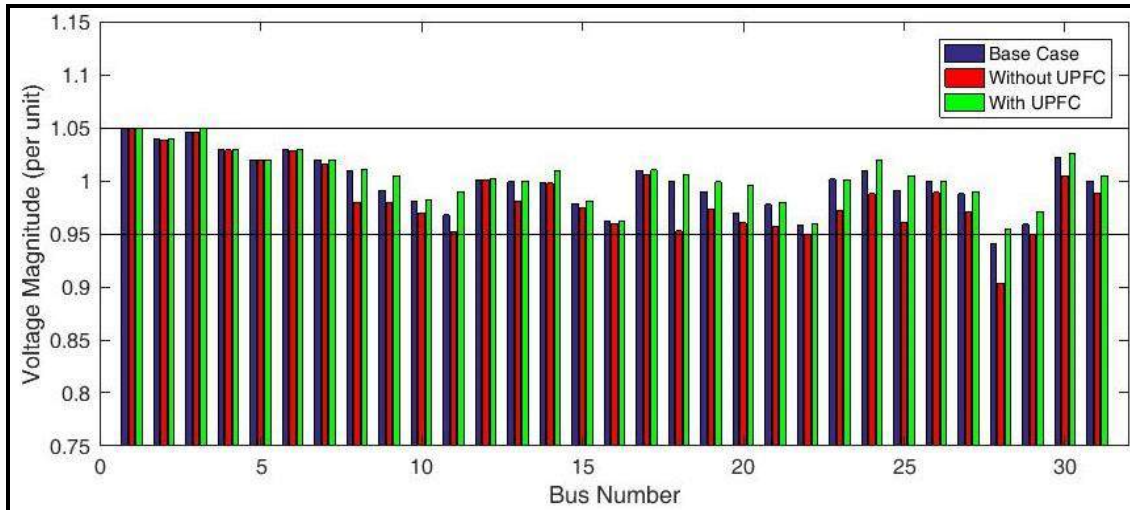


Figure 3: Voltage profile results under critical loading condition

B. Heavy Reactive Loading with Single Generator Outage

Table 2 shows the performance of GWO during a heavy reactive loading under a single generator outage condition. The power flow result revealed that, the loss of generation at Bus-7 increases the losses at line 6 to 85.54MVar from the initial base case with succeeding cascading failures on lines 7 (4-21) and 31(6-27) due to their nearer connections to the critical lines. Also, at line 36(8-29), a loss of 155MVar, the highest reactive power loss occurs due to the source’s network topology and distance. Bus 28 is evidently the weakest and most vulnerable node, due to its lowest permissible

reactive load of 0.4154MVar in the presence of contingency. It is also evident that the generator outage condition increases the network’s total power losses compared to normal conditions. It also reveals that with the installation of UPFC on the network, apparent power loss at the 6th line reduces from 105.54MVar to 32.22MVar representing 69.47% loss reduction, and at branch 36, a loss of 155MVar reduces to 28.95MVar representing 81.32%. This enhancement is witnessed in the whole network, which has demonstrated the UPFC device’s capability to control voltage magnitude at a bus and power flow in a line where it is installed.

Table 2: Power flow result for 31-bus, 330kV NNG during generator outage

Percentage Load Increase	Losses without UPFC (MVar)	Rating of UPFC (MVar)	Losses with UPFC (MW)	UPFC Location	Percentage Power Loss Reduction
42.30	250.5430	-189.98MVar	164.6500	24	34.28

In order to analyse the steady-state stability condition of the network under a heavily loaded reactive power and a single generator outage, bus 17 is loaded to a maximum load level of 42.30%, and generator-7 is made out of service to create contingency. High severity is witnessed when the outage of the generator at bus-7 occurred. Figure 4 shows the voltage profile of heavy reactive loading of bus 17 at 42.30% with and without UPFC installation. The major voltage sag occurred at bus 28 (0.9092) due to loss of reactive power that should originates from generator at bus-7 that was made out of service. From this Figure 4, it is identified that, simultaneous heavy loading and generator-7 outage have more effects on the voltage magnitudes. This is due to the lack of

reactive power that generator-7 ought to support the network. With an optimal installation of the UPFC device of reactive power setting - 189.98MVar at Bus 24, all voltage at the buses are augmented and stabilized to the tolerable limit.

C. Heavy real power loading with Single (N-1) line outage

Table 3 shows the performance of GWO for a single line outage condition of 31-bus, 330kV NNG. The most sensitive line 28 is made out of service, and a maximum load-ability is obtained at 42.76% at 47th iterations. An overall power loss of 180.2350MW is obtained. After optimal placement of the UPFC device, the power loss reduces to 95.4500MW, representing a 47.0414% loss

reduction. The optimal installation of UPFC of reactive power setting is -89.7500MVar on bus 19.

The UPFC considerably reduced the total power losses on the network.

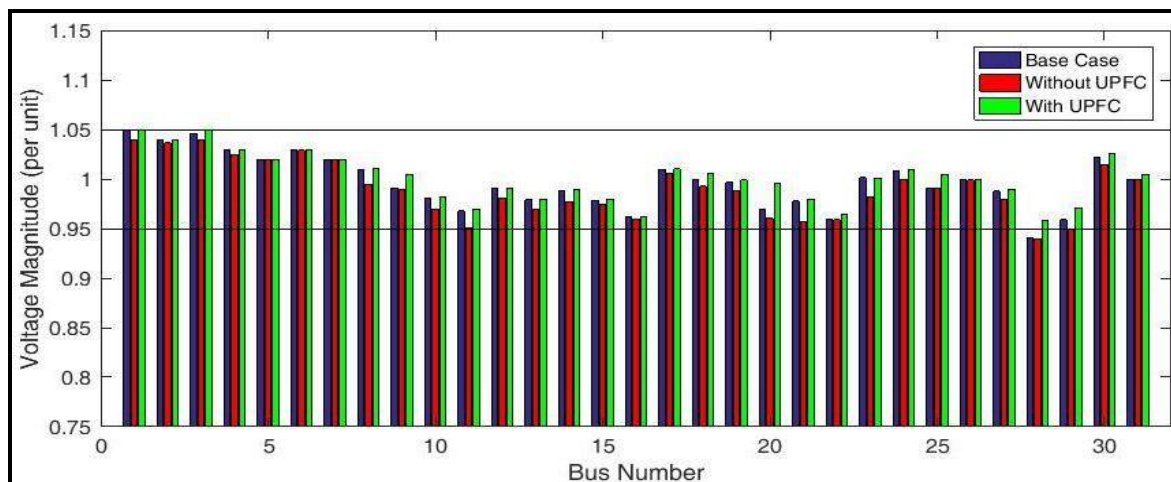


Figure 4. Voltage profile under heavily reactive loading at Bus 17 with Single Generator Outage

Table 3: Power flow result for 31-bus, 330kV NNG under single line outage

Percentage Max. Loading Value	Losses without UPFC (MW)	Rating of UPFC (MVar)	Losses with UPFC (MW)	UPFC Location	Percentage Power Loss Reduction
42.75%	180.2350	-89.7500	115.4500	19	47.0414

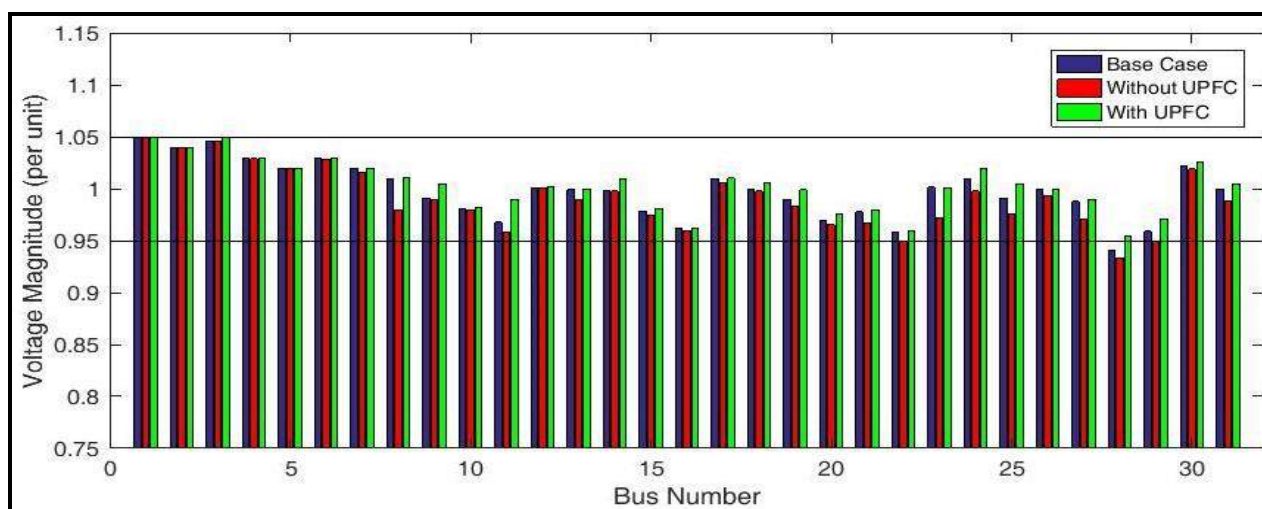


Figure 5: Voltage profile under real heavy load with a single (N-1) line outage

The most sensitive line 28 is made out of service, and a maximum load-ability is obtained at 42.76% at the point of voltage collapse. GWO was used for the optimal location and sizing of the UPFC device by considering all the contingency. The result shows that buses 22 (0.9476) and 28 (0.9092) have the highest voltage sags. After installing the -89.7500MVar size of UPFC on the network at bus 19, the voltage sags experienced was adequately compensated through the proper injection of sufficient reactive power to the network to

maintain a stable network by keeping all the buses within the acceptable limit. The critical voltage occurs on bus 28 (0.8999 p.u), resulting from the bus's long distance from the generating unit. The optimal installation of UPFC at bus 19 normalized all violated voltages as shown in Fig. 5. It is evident from the foregoing, that UPFC can improve power flow of a transmission line, by reducing the network power losses and enhance voltage stability.

6. CONCLUSION

This paper proposes a nature-inspired metaheuristic grey wolf optimization technique for optimal location and sizing of UPFC on 31-bus, 330kV Nigeria National Grid test system for power loss minimization and voltage deviation reduction. Optimal power flows at steady-state analyses are performed to determine the system performance of the proposed GWO algorithm on the test system under different load variations and contingency for a voltage control reference between 0.95p.u. to 1.05p.u. The results are evaluated based on two scenarios: load-ability analysis under maximum loading of the network and load-ability analysis under single contingency. The results show that using the FACTS device (UPFC) at an optimal location on the network, yields significant reductions in power loss and minimize voltage deviation compared to the base case without the FACTS device. It is also evident that more power can be wheeled and delivered to meet the ever-growing demand over an existing transmission asset during both normal and contingency condition without violating the voltage stability by using the proposed method in this paper.

REFERENCES

- [1] K. O. Ignatius, A. O. Emmanuel, and A. O. Patrick, "Load Flow Assessment of the Nigeria 330-kV Power System," *American Journal of Electrical and Electronic Engineering*, vol. 5, pp. 159-165, 2017.
- [2] A. Pillay, S. Prabhakar Karthikeyan, and D. P. Kothari, "Congestion management in power systems – A review," *International Journal of Electrical Power & Energy Systems*, vol. 70, pp. 83-90, 2015/09/01/ 2015.
- [3] P. Singh, R. Tiwari, A. K. Singh, and V. Sangwan, "Optimal Allocation and Comparative Investigation of Unified Power Flow Controller using ASMO," in *2020 International Conference on Power Electronics & IoT Applications in Renewable Energy and its Control (PARC)*, 2020, pp. 497-502.
- [4] I. A. Araga, A. O. Anibasa, and I. I. Alabi, "Placement of Multiple Svc on Nigerian Grid System for Steady State Operational Enhancement," *American Journal of Engineering Research (AJER)*, vol. 6, pp. 78-85, 2017.
- [5] S. P. Dash, K. Subhashini, and J. Satapathy, "Optimal location and parametric settings of FACTS devices based on JAYA blended moth flame optimization for transmission loss minimization in power systems," *Microsystem Technologies*, pp. 1-10, 2019.
- [6] S. S. Yusuf, J. Boyi, O. P. Ubeh, A. A. Saidu, and M. I. Onimisi, "Transmission Line Capacity Enhancement with Unified Power Flow Controller Considering Loadability Analysis," *ELEKTRIKA-Journal of Electrical Engineering*, vol. 18, pp. 8-12, 2019.
- [7] D. Stita, K. R. Subhashini, and J. Satapathy, "Efficient utilization of power system network through optimal location of FACTS devices using a proposed hybrid meta-heuristic Ant Lion-Moth Flame-Salp Swarm optimization algorithm," *International Transactions on Electrical Energy Systems*, p. e12402, 2020.
- [8] S. Ravindra, C. V. Suresh, S. Sivanagaraju, and V. C. Reddy, "Power System Security Enhancement with Unified Power Flow Controller under Multi-event Contingency Conditions," *Ain Shams Engineering Journal*, pp. 1-10, 2015.
- [9] K. S. Verma, S. N. Singh, and H. O. Gupta, "Location of unified power flow controller for congestion management," *Electric Power Systems Research*, vol. 58, pp. 89-96, 2001/06/21/ 2001.
- [10] E. Omorogiuwa and S. Ike, "Power Flow Control in the Nigeria 330kV Integrated Power Network using Unified Power Flow Controller (UPFC)," *International Journal of Engineering Innovation & Research*, vol. 3, pp. 723-731, 2014.
- [11] S. Raj and B. Bhattacharyya, "Optimal placement of TCSC and SVC for reactive power planning using Grey wolf optimization algorithm," *Swarm and Evolutionary Computation BASE DATA*, pp. 1-29, 2017.
- [12] A. O. Emmanuel, K. O. Ignatius, and E. A. Abel, "Enhancement of Power System Transient Stability - A Review," *IOSR Journal of Electrical and Electronics Engineering (IOSR-JEEE)*, vol. 12, pp. 32-36, 2017.
- [13] M. V. Suganyadevi and C. K. Babulalb, "Estimating of Loadability Margin of a Power System by comparing Voltage Stability Indices," *International Conference on "Control, Automation, Communication and Energy Conservation*, pp. 1-5, 2009.

- [14] S. Ratra, R. Tiwari, and K. R. Niazi, "Voltage stability assessment in power systems using line voltage stability index," *Computers & Electrical Engineering*, 2018/01/05/ 2018.
- [15] S. Quaia, "Critical analysis of line loadability constraints," *International Transactions on Electrical Energy Systems*, p. e2552, 2018.
- [16] S. N. Singh and I. Erlich, "Locating unified power flow controller for enhancing power system loadability," in *2005 International Conference on Future Power Systems*, 2005, pp. 5 pp.-5.
- [17] J. D. Glover, M. S. Sarma, and T. J. Overby, *Power System Analysis and Design*. Stamford, USA: Global Engineering Publishers, 2012.
- [18] J. J. Paserba, "How FACTS Controllers Benefit AC Transmission Systems," *IEEE Press*, 2003.
- [19] T. G. Manohar and R. S. Reddy, "Literature Review on Voltage stability phenomenon and Importance of FACTS Controllers In power system Environment," *Global Journal of Researches in Engineering Electrical and Electronics Engineering*, vol. 12, pp. 24-29, 2012.
- [20] O. A. Mousavi, M. Bozorg, and R. Cherkaoui, "Preventive Reactive Power Management for Improving Voltage Stability Margin," *Electric Power System Res*, pp. 36-46, 2013.
- [21] M. J. Vahid-Pakdel, H. Seyedi, and B. Mohammadi-Ivatloo, "Enhancement of power system voltage stability in multi-carrier energy systems," *International Journal of Electrical Power & Energy Systems*, vol. 99, pp. 344-354, 2018/07/01/ 2018.
- [22] L. Gyugi, "A Unified power flow controller concept for flexible AC transmission systems.," in: *Fifth International Conference on AC and DC Transmission, London*, pp. 19 - 26, September 17–20, 1991 1991.
- [23] X. P. Zhang, C. Rehtanz, and B. Pal, *Flexible AC Transmission Systems: Modelling and Control*. Heidelberg New York Dordrecht London: Springer, 2012.
- [24] S. Mirjalili, S. Mohammad, and A. Lewis, "Advances in Engineering Software Grey Wolf Optimizer," *Advances in Engineering Software*, vol. 69, pp. 46-61, 2014.
- [25] L. D. Mech, "Alpha status, dominance, and division of labor in wolf packs," *Can. J. Zool*, vol. 77, pp. 1196-1203, 1999.
- [26] D. P. Ladumor, R. H. Bhesdadiya, I. N. Trivedi, and P. Jangir, "Optimal Power Flow with Shunt Flexible AC Transmission System (FACTS) Device Using Grey Wolf Optimizer," *3rd International Conference on Advances in Electrical, Information Communication and Bio-Informatics (AEEICB17)*, 2017.



Rainfall Variability and Trend Analysis over Lokoja, Nigeria

Animashaun I. M.*, Adeoye P. A. Otache, M. Y and Abatan, O. A.

Agricultural and Bioresources Engineering, Federal University of Technology, Minna

* Corresponding author email: ai.iyanda@futminna.edu.ng

Received: 05.05.2020

Accepted: 09.08.2020

Published: 31.12.2020

Abstract- Studies on rainfall variability and trends are of great importance, particularly to the nations where rain-fed agriculture is predominant. This study used CRU data (CRU_TS 4.01) to examine the temporal variability of rainfall data over Lokoja. Statistical tests were employed to examine variability and trend in monthly, seasonal and annual time series. Analysis of variability showed that the rainy seasons and annual rainfall had less variability ($CV < 20$), but the variability was high ($CV > 30$) in some months in the rainy season (April, July and August). Standardised precipitation index showed alternation of wet and dry period conditions had been witnessed in the study area. Trend analysis showed more positive trends had been experienced from 1970 through 2010. The variability in rainfall and the increasing trend may have a tremendous effect on water resources availabilities and vulnerabilities of Lokoja.

Keywords: Lokoja, Mann-Kendall, Rainfall, Trend Analysis

1. INTRODUCTION

Rainfall is a major climatic parameter that influences crop production [1]. In Nigeria, like many other developing nations, agricultural practices depend majorly on rainfall. The variability of rainfall in response to climate change poses a serious threat to food security and water availability [2]. Rainfall variability is the unsteadiness of rainfall occurrence yearly or seasonally above or below a long-term mean value; over a particular period [3]. [4] suggested a need for a detailed analysis of local precipitation variability. Understanding variability in rainfall is a prerequisite to hydro-meteorological applications such as construction of agricultural and hydropower dams, planning for agriculture purpose, forecasting of floods and drought, urbanization, quantification of climate change impact, modeling of hydrological feature, estimation of water balance and irrigation management for viable crop production [5]. It is important to understand rainfall pattern and trend at any place, as it has great importance and relevance in water storage for future use. The

issue of water scarcity when needed or availability of less than the required has necessitated the need for proper water resources planning and management [6]. In addition to water scarcity, the extreme climatic event of drought and flood, which has become a reoccurrence event, also calls for concern [7]. [8] claimed that there is a high correlation between rainfall variability and extreme hydrological event occurrence. In the same vein, spatiotemporal patterns of water availability also depend largely on rainfall [9]. There is a need to study the spatial and temporal variability of rainfall over a long time. It allows for better understanding of the effects of climate change on rainfall as well as its probable impact on the water system and the environment [10]. Assessment of rainfall trends and variability study is paramount to understanding the variations in space and time. Trend analysis of precipitation on diverse spatial and temporal scales has become a topical issue among researchers in the past century because of the attention given to global climate change by the

scientific community [11]. Some parametric and non-parametric statistical tests have been found relevant in examining the trend of climatic parameters. Though parametric tests are more powerful as compared to non-parametric test, they, however, require independent and normally distributed data series. In contrast, non-parametric test requires only data to be independent data [5]. More so, the non-parameter tests can remove outliers. The most frequently used non-parametric test for analysis of rainfall trend is the Mann Kendal (MK).

Several studies have been carried out on the analysis of precipitation variability throughout the world. [12] studied a series of seasonal and annual precipitation for the period of 1833–1996 from 32 stations. On a seasonal basis, a decreasing trend was significant only for spring in Central-South and autumn in the North. While on an annual basis, the result showed a decreasing trend over Italy in its entirety, but it was statistically significant only in the Central-South. [13] examined trends in annual mean and monthly precipitation series on a long-term basis (1929 to 1993) in Turkey. Their results showed some significant trends, especially in the mean annual precipitation and in some months (January, February and September). The study by [14] also showed a significant decrease in the main rainy season (June to September) in the southwestern and central parts of Ethiopia. [15] examined the spatiotemporal patterns of monthly and annual precipitation in Nigeria between 1901 and 2000. They noted a variation in the rainfall patterns and submitted that while the 1950s was the wettest decade, the driest was 1980s. [16] studied the rainfall trend from 1953 to 2002 in northern Nigeria and reported an increase in the annual trend of rainfall between 1993 and 2002. All the studies cited above suggested that spatial and temporal variability in the long-term behaviour of rainfall dependent largely on regional characteristics. This study thus aimed at examining rainfall variability and trend analysis over Lokoja, Nigeria

2. MATERIALS AND METHODS

2.1 Study area

Lokoja is situated on the latitude 7°45'N - 7°51'N and longitude 6°41'E - 6°45'E. It lies at an

altitude of 45 to 125 meters above sea level and located close to the confluence of River Niger and River Benue [17]. It is the capital city of Kogi State-a state that share boundaries with some states in the southern and northern region of the country and hence a gateway to five of the six geopolitical zones in the country (Figure 1). Lokoja is characterized by a tropical climate that comprises of wet and dry seasons and falls within the Guinea Savannah vegetation belt. It experiences annual rainfall and temperature of about 1150 mm and 27.7°C respectively. It has total land coverage of about 63.82 sq. km. [18]. The area has a land use/land cover characterized by water bodies, wetland resources, vegetation and built-up area, which is massively expanding [19]. It also has dissected undulating plains, high hill masses, and many intermittent valleys and streams crisscrossing the breadth of the town [17].

2.2 Details of data and methods

The observed data used is gridded data. The gridded monthly rainfall data from the Climate Research Unit (CRU_TS 4.01) with a resolution of 0.5 by 0.5 latitude and longitude over the periods 1911 - 2010 was obtained and used for the analysis. The average rainfall amount was computed over the 100 years to examine rainfall anomalies, commonly defined as deviation from the average. For the variability analysis, standard deviation and coefficient of variation (CV) were calculated. Rainfall Anomaly Index (RAI) and the Standardised Precipitation Index (SPI) were computed to examine rainfall frequency and intensity. The coefficient of variation was used to calculate the degree of variability in the rainfall. The value of the CV is directly proportional to the degree of variability. The value of CV is categorised into three; less ($CV < 20$), moderate ($20 < CV < 30$), and high ($CV > 30$) (Hare, 2003). The Mann-Kendall trend analysis method was applied to examine the trend in annual, seasonal and monthly rainfall data. Mann-Kendall test was formulated by Mann (1945) as a non-parametric test for trend detection and the test statistics distribution given by Kendall (1975) for testing non-linear trend and the turning point. Mann Kendall and Sen Slope estimator were applied to determine the trend direction and

magnitude. The detail of rainfall variability index

and trend analysis is given below:

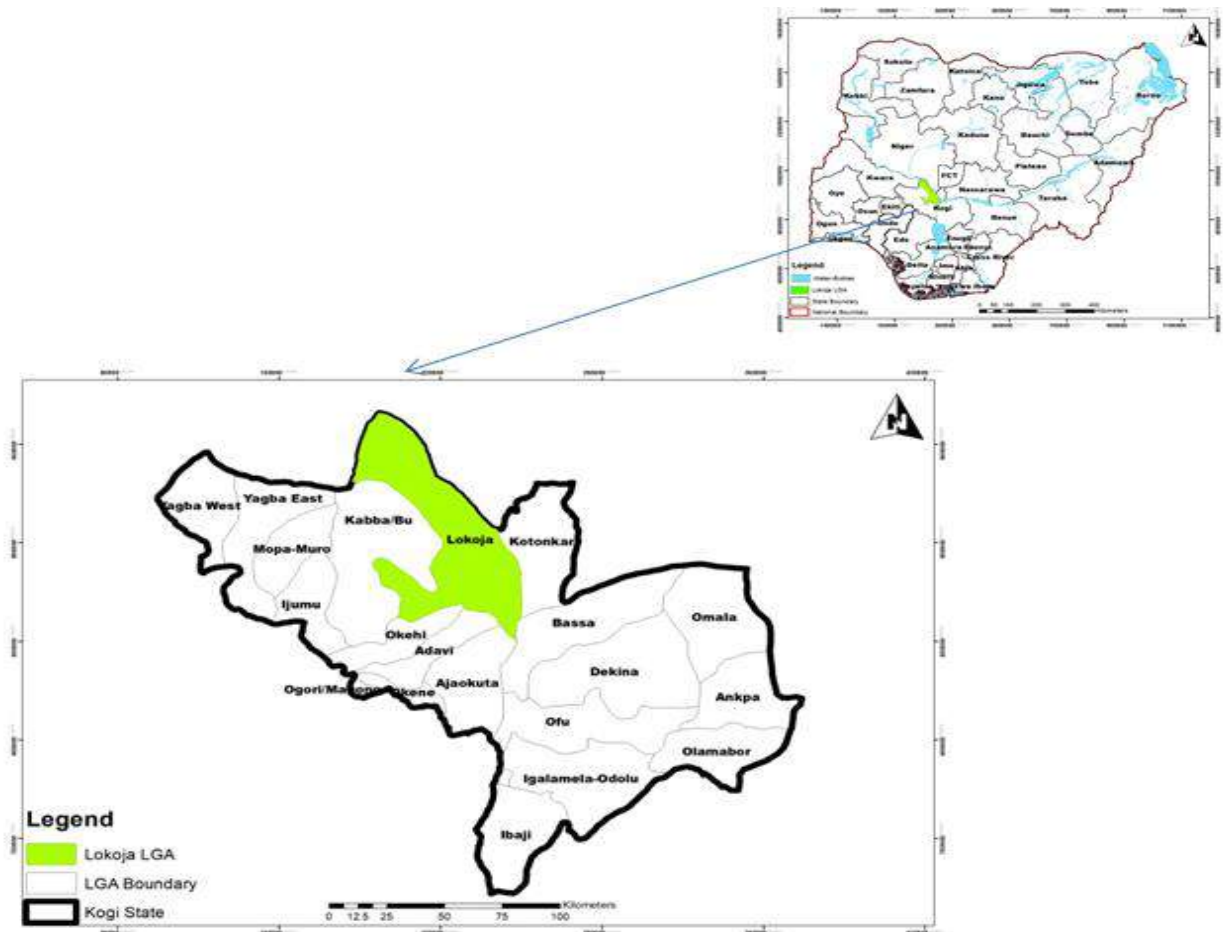


Figure 1: Map of the study area

2.2.1 Rainfall Anomaly Index (RAI)

Annual Rainfall Anomaly Index (RAI) was used to analyse the frequency and intensity of the dry and rainy years. The monthly RAI was also calculated for specific years of the historical series aiming to analyse the distribution of rainfall in the years of the greatest anomaly. According to [20], the RAI constitutes the following equations:

$$RAI = 3 \left[\frac{N - \bar{N}}{\bar{M} - \bar{N}} \right], \text{ for positive anomalies} \quad (1)$$

$$RAI = -3 \left[\frac{N - \bar{N}}{\bar{x} - \bar{N}} \right], \text{ for negative anomalies} \quad (2)$$

Where: N = current monthly or yearly rainfall in mm (or the month/year when RAI will be generated); \bar{N} = monthly or yearly average rainfall of the historical series (mm); \bar{M} = average of the ten highest monthly or yearly rainfall of the historical series (mm); \bar{x} = average of the ten

lowest monthly or yearly rainfall of the historical series (mm), and positive anomalies have their values above average, and negative anomalies have their values below average. The variability index was computed on a monthly, yearly and seasonal basis (NDJFM: November, December, January, February, and March, AMJ: April, May, and June, JASO: July, August, September, and October,) corresponding to the dry season, early rainy season and late rainy season as understood by the local farmers in the study area [4].

Table 1: Classification of Rainfall Anomaly Index Intensity

RAI Range	Classification
Above 4	Extremely humid
2 to 4	Very humid
0 to 2	Humid

-2 to 0	Dry
-4 to -2	Very dry
Below -4	Extremely dry

Source: Costa and Rodrigues (2017)

2.2.2 SPI Drought indices

The Standardised Precipitation Index (SPI) is a useful tool developed by McKee et al. in 1993 for drought monitoring and analysis [21]. It is normally used to assess the length and magnitude of drought events. It has gained the acceptance of the World Meteorological Agency (WMO) as an index to be used for drought monitoring across the world. To compute SPI for a particular location, a long-term historical rainfall record (thirty years or more) is fitted to a probability distribution function (pdf) (generally the gamma distribution), which is then transformed to a normal distribution so that the mean SPI for the location and considered period is zero [22]. Since research has shown that rainfall is subject to the gamma distribution law [22], a process of maximum likelihood estimation of the gamma distribution parameters, α and β , is thus applied to fit the rainfall distribution. Its probability density function defines the equation representing the distribution as:

$$g(x) = \frac{1}{\beta^\alpha \Gamma(\alpha)} x^{\alpha-1} e^{-\frac{x}{\beta}} \quad (3)$$

for $x > 0$

where a and β are the respective shape and scale parameters, x is the rainfall amount and $\Gamma(a)$ is the gamma function. Parameters a and β of the gamma pdf are estimated for each station and for each time scale of interest (1, 3, 6, 9, 12 months.). Maximum likelihood estimations of a and β are:

$$\alpha = \frac{1}{4A} \left(1 + \sqrt{1 + \frac{4A}{3}} \right) \quad (4)$$

$$\beta = \frac{x}{\alpha} \quad (5)$$

$$\text{where } A = \ln(x) - \frac{\sum \ln(x)}{n} \quad (6)$$

x is the rainfall average; and n is the number of observations.

The resulting parameters are then used to find the cumulative probability of an observed rainfall event for the given month and time scale for the location in question. Since the gamma function is undefined for $x = 0$ and a rainfall distribution may

contain zeros, the cumulative probability becomes:

$$H(x) = q + (1 - q)G(x) \quad (7)$$

q is the probability of zero rainfall and $G(x)$ is the cumulative probability of the incomplete gamma function. If m is the number of zeros in a precipitation time series, then q can be estimated by m/n . The cumulative probability $H(x)$, is then transformed to the standard normal random variable z with mean zero and variance of one [21], which is the SPI value. According to the SPI, a drought event occurs when the index continuously reaches an intensity of -1.0 or less, and the event ends when the SPI becomes positive. The various classifications of drought based on SPI are as shown in Table 2

Table 2: Classification of different Precipitation Indices

SPI Value	Drought Category
> 2.0	Extremely wet
1.5 to 1.99	Very wet
1.0 to 1.49	Moderately wet
-0.99 to 0.99	Near normal
-1.0 to -1.49	Moderately dry
-1.5 to -1.99	Severely dry
-2 and less	Extremely dry

2.2.3 Trend Analysis

Mann-Kendall was used to determine the monotonic trends in rainfall. To apply the test, the condition that must be satisfied is given as in equation 8:

$$\chi = f(t) + \sum t \quad (8)$$

The MK test statistic ‘S’ is calculated as follow:

$$S = \sum_{i=1}^{n-1} \sum_{j=i+1}^n \text{sign}(x_j - x_i) \quad (9)$$

Where x_i and x_j are the sequential data values, n is the data set record length, and

$$\text{Sign} = \begin{cases} +1 & \theta > 0 \\ 0 & \text{if } \theta = 0 \\ -1 & \theta < 0 \end{cases} \quad (10)$$

indicates positive differences, no differences, and negative differences, respectively and S is computed as the sum of the integers. The variance of the expected value of S equals zero ($E[S] = 0$) for series without trend and is given by::

$$\sigma^2(s) = \frac{1}{18} [n(n-1)(2n+5) - \sum_{p=1}^q t_p(t_p-1)(2t_p+5)] \tag{11}$$

Where q is the number of tied groups and t_p is the number of data values in p^{th} group. The test statistics Z is then given as:

$$Z = \begin{cases} \frac{s-1}{\sqrt{\sigma^2(s)}} & S > 0 \\ 0 & \text{if } S = 0 \\ \frac{s+1}{\sqrt{\sigma^2(s)}} & S < 0 \end{cases} \tag{12}$$

The Z statistic is used to test the null hypothesis, H0, that the data are randomly ordered in time, with the alternate hypothesis, H1, indicating an increasing or decreasing monotonic trend. The trend analysis was done on three different timescales. The timescale used is based on the assertion of [15] that 1969 is a year with a distinct change in annual rainfall for many regions in Nigeria.

3. RESULTS AND DISCUSSION

3.1 Variability study

Variability study and Trend analysis of rainfall and its spatial and temporal variability in a changing climate is important to access climate-induced changes and suggests adequate water

resources management for the future. The data for rainfall over Lokoja from 1911 to 2010 were analysed using basic statistics such as maximum, minimum, standard deviation, standard deviation and coefficient of variation. The statistical analyses for the 100-year time series of rainfall (1911-2010) are presented in Table 2. The mean annual rainfall was 1401.581 mm having a standard deviation of 168.42 mm. The minimum annual rainfall experienced in the area under consideration was 809.9 mm while the maximum was 1778.6 mm. The coefficient of variation (CV) was highest during December 183.28 % followed by January 147.72 %. This was not unexpected as the two months fall in the dry season. Of the months within the rainy season (April-October), August has the highest coefficient of variation (38.61%) while September has the least (16.73%). The results showed that the degree of variability was less only in September (CV < 20), moderate in May, June, and July (20 < CV < 30) while April, July and August have experienced high variability in rainfall over the 100 years considered (1911-1910).

Table 2: Monthly (mm/month) and annual (mm/year) statistics over Lokoja (1911-2010)

Months	Min	Max	Mean	SD	CV (%)
Jan	0	24.80	3.15	4.65	147.72
Feb	0.00	48.40	12.48	12.93	103.61
Mar	2.50	154.50	51.09	28.14	55.09
Apr	20.70	243.50	108.02	38.90	36.01
May	99.10	280.10	171.78	36.93	21.50
Jun	95.50	307.10	198.09	40.62	20.50
Jul	42.30	396.70	210.83	64.23	30.46
Aug	51.10	430.30	205.25	79.25	38.61
Sep	93.60	347.50	259.79	43.46	16.73
Oct	47.50	271.10	159.04	47.67	29.97
Nov	0.30	77.40	18.72	16.65	88.94
Dec	0.00	36.40	3.35	6.15	183.28
Annual	809.90	1778.60	1401.58	168.42	12.02
AMJ	324.00	695.80	477.89	74.50	15.59
JASO	306.90	1146.40	834.90	136.81	16.39
NDJFM	17.70	231.10	88.79	42.33	47.67

On the seasonal timescale, of the two rainy seasons, the variability was highest in JASO

(16.39%) and closely followed by in AMJ (15.59%). The coefficient of variation showed

that the temporal variability of annual rainfall was the lowest (12.02%). The rainy seasons and annual rainfall fall under the class of less variability. To the total annual rainfall of 1401.58 mm over 100 years, rainfall during September (259.79) and July (210.83) have the highest contributions, with each contributing a respective value of 18.53% and 15.04%. Of the seasons, JASO has the highest contribution (675.86), representing 59.57% of the total annual rainfall (Figure 2 and 3). These findings are in agreement with the reports of [23] and [24].

3.2 Rainfall indices

The result of the rainfall anomaly index showed that the wettest year was 1914 (1.60), and the driest year was 1931 (0.01) (Figure 4). The two, however, fall into the class of humid. Comparison between the two years (wettest and driest) showed that more rainfall was experienced in the early rainy season (AMJ) of the wettest while the driest have more rains during the late rainy seasons (JASO) (Figure 5). The results showed that the index (RAI) fails to detect the dry condition in Nigeria in a century data of rainfall. However, a further study with SPI, showed varying degree of the wet and dry conditions.

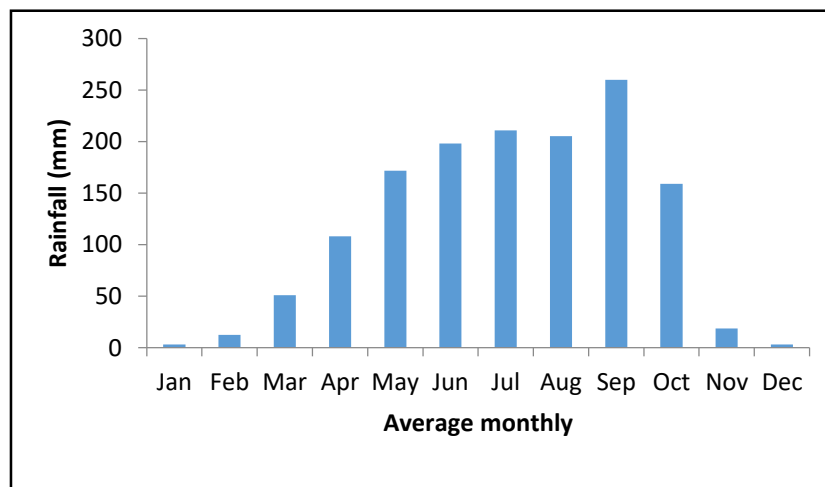


Figure 2: Average Monthly Rainfall over 1911-2010

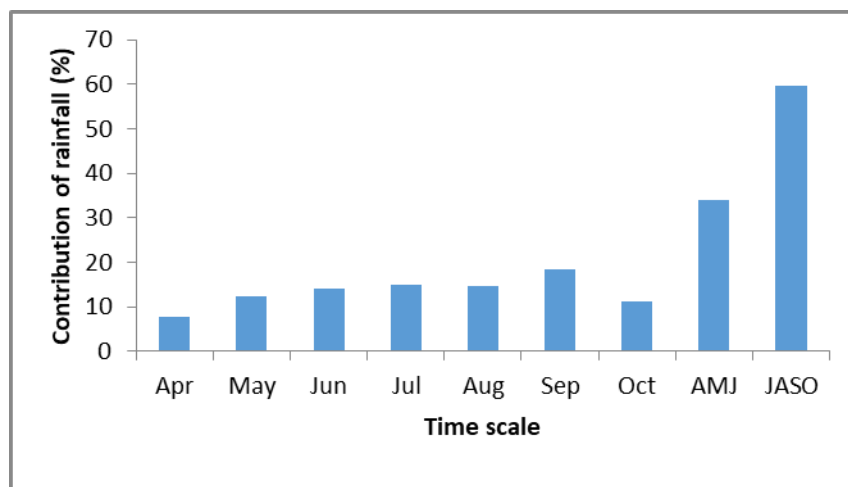


Figure 3: Monthly and Seasonal contribution to the annual Rainfall

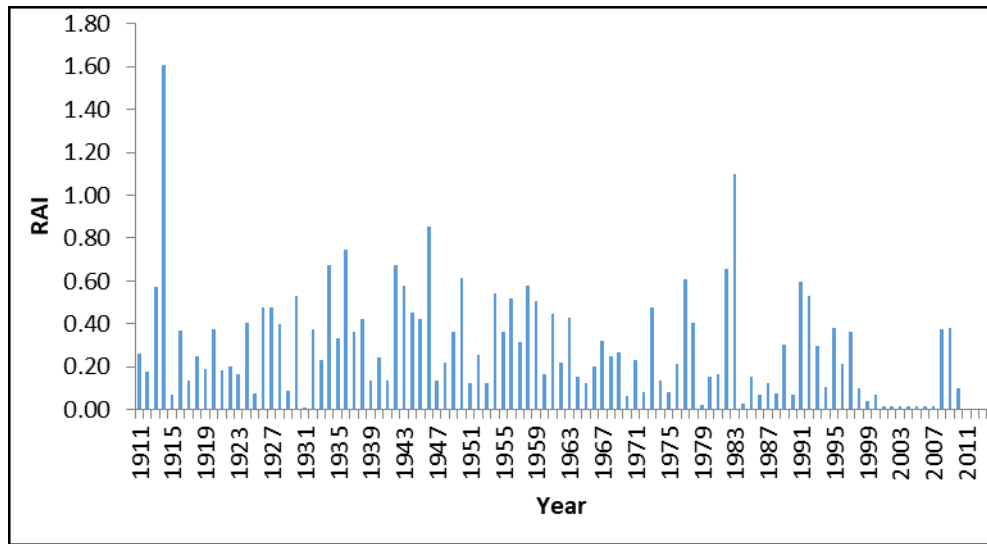


Figure 4: Rainfall anomaly index from 1911-2011

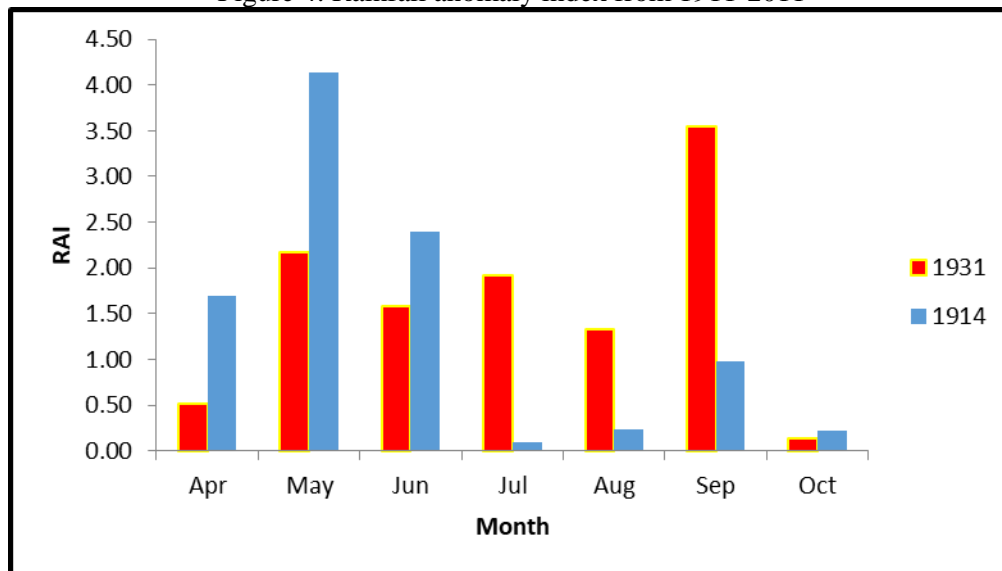


Figure 5: Comparison between the most humid and driest year

The time series plots of SPI showed a lower temporal frequency and longer duration of dry and wet periods on the monthly (Figure 6) and annual (Figure 7) time scale. Of the total timeline, two years (1914, 1983) experienced extreme dry, severe dry was experienced in three years (1936, 1942, 1945) and eleven years (11) experienced moderate dry. Near normal was experienced in the study location for sixty-five (65) years. Extreme wet was only experienced in 1934. Three years (1930, 1954, and 1991) experienced very wet condition; moderate wet was experienced for fifteen years. The annual and 12-

month timescale analysis showed that the driest year was 1914 (extremely dry) while the wettest year was 1934 (extremely wet). Between 1916 and 1934 and between 1963 and 1980, Lokoja witnessed wet conditions while between 1942 and 1946 more dry condition was experienced. Alternation of wet and dry period conditions was witnessed between 1950 and 1982. The results of these findings is in line with earlier findings of [25], [26], [15] and [27] who had laid claim to the existence of drought within the period mentioned in this study.

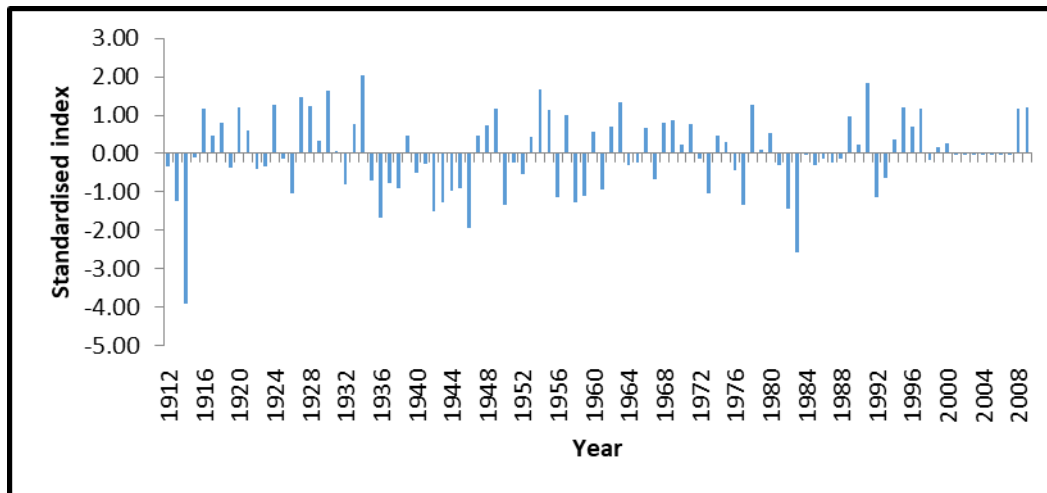


Figure 6: Time series plot of SPI on an annual timescale

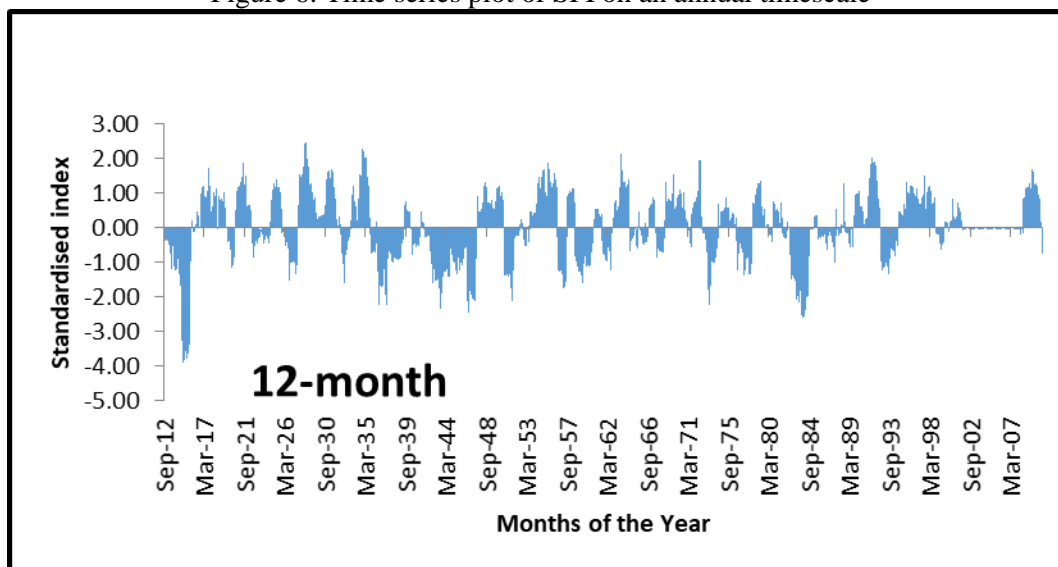


Figure 7: Time series plot of SPI on months of the years' timescale

3.3 Trend Analysis

The results of monotonic trends and slope estimates for different timescales (1911-2010, 1911-1969 and 1970-2010) are presented in Table 3. Monthly trend tests showed a mix of positive and negative trends at Lokoja. During the year 1911-2010, statistically significant positive trends were found in July and August (at 5%), while a significant negative trend was found in November (at 1%). All the months in the dry season experienced negative trends, indicating that the dry seasons are getting drier. Non-significant trends have been experienced in the early rainy season (AMJ) while the late rainy season has

experienced a statistically significant trend (5%). Sen's slope estimate (Q) showing the true slope of linear trend (i.e. change per month) is also presented in Table 3. The timeline 1911-1969 and 1970 to 2010 also experienced a mixture of positive and negative trends. More positive trends experienced in the period 1970-2011 compared to 1911-1968; indicate a relative increase in the monthly rainfall during the later climatic period (1970-2010). This could be what manifests through incessant flood witnessed in the area in recent times. This work agrees with the claim of [28] that rainfall is on the increase in most of the stations in Nigeria.

Table 3: Mann-Kendall Trend

Time series	1911-2010		1911-1969		1970- 2010	
	Test Z	Q(mm/month)	Test Z	Q(mm/month)	Test Z	Q(mm/month)
January	-0.72	0.00	-0.26	0.00	0.91	0.00
February	-0.19	0.00	-1.19	-0.06	0.43	0.01
March	-1.66 ⁺	-0.15	0.01	0.00	-0.56	-0.03
April	-1.16	-0.16	-0.45	-0.16	0.59	0.12
May	0.21	0.02	-0.58	-0.19	0.01	0.00
June	0.39	0.05	0.76	0.35	0.28	0.06
July	2.56 [*]	0.52	1.22	0.58	1.64	1.09
August	2.16 [*]	0.58	0.03	0.03	0.96	0.96
September	-0.97	-0.15	-0.30	-0.13	-0.06	0.00
October	-0.03	0.00	0.55	0.23	1.26	0.51
November	-2.65 ^{**}	-0.11	-0.35	-0.05	1.77 ⁺	0.14
December	-0.40	0.00	-0.17	0.00	1.74 ⁺	0.03
Annual	1.00	0.59	0.22	0.33	1.06	1.19
AMJ	-0.50	-0.13	-0.12	-0.04	0.64	0.36
JASO	2.40 [*]	0.96	0.84	0.75	1.62	1.65
NDJFM	-2.54 [*]	-0.32	-0.65	-0.19	-0.25	-0.04

** trend at 0.01 level of significance, *trend at 0.05 level of significance, + the trend at 0.1 level of significance

4. CONCLUSION

The study investigated variability and trends in rainfall time series for the annual, wet and dry season over Lokoja between 1911 and 2010. The analysis of rainfall showed that September has the highest percentage of monthly contributions (18.53%) to the annual rainfall and the late rainy season (JASO) contributed the highest (59.57%) on a seasonal basis. Rainfall anomaly index (RAI) showed that the wettest year was 1914, and the driest year was 1931. However, both values are humid, suggesting that the index may only be suitable for detecting the wet condition. The Standardised precipitation index showed that all the different classes (from extremely dry to extreme wet) of precipitation indices had been witnessed in Lokoja. The driest years were 1914 and 1983 (both extremely dry), and 1934 was the wettest year (extreme wet). More months showed a decreasing trend of rainfall during the 1911-1969 climatic periods compared to 1970-2010, which is on the increase. The trend suggested a probable temporal increase in rainfall trend, which may have impacts on water resources management, agricultural practices and the socio-

economic activity of the area as it is being witnessed through the flood in recent time.

REFERENCES

- [1] Duhan, D., Pandey, A., 2013. Statistical analysis of long term spatial and temporal trends of precipitation during 1901–2002 at Madhya Pradesh, *India Atmospheric Research* 122 (2013) 136–149
- [2] Animashaun, I. M., Oguntunde, P. G., Akinwumiju, A. S. and Olubanjo, O. O., 2018. Niger River Basin and SWAT Model Application in Nigeria Context: A Review, the 2018 Annual Conference of the School of Engineering & Engineering Technology, FUTA, 17-19 July, page 674-684
- [3] IPCC (2007): Intergovernmental Panel on Climate Change, Synthesis Report. An Assessment of the Intergovernmental Panel on Climate Change; IPCC: Valencia, Spain.
- [4] Animashaun, I. M., Oguntunde, P. G., Akinwumiju, A. S., and Olubanjo, O. O. (2020):

- Rainfall Analysis over Niger Central Hydrological Area, Nigeria: Variability, Trend and Change-point detection, Scientific African <https://doi.org/10.1016/j.sciaf.2020.e00419>
- [5] Pranuthi, G., Dubey, S. K., Tripathi S. K. and Chandniha, S. K. (2014) Trend and Change Point Detection of Precipitation in Urbanizing Districts of Uttarakhand in India *Indian Journal of Science and Technology*, 7(10), 1573–1582.
- [6] Panthi, J., Dahal, P., Shrestha, M.L., Aryal, S., Krakauer, N.Y., Pradhanang, S.M., Lakhankar, T., Jha, A.K., Sharma, M., Karki, R. (2015). Spatial and Temporal Variability of Rainfall in the Gandaki River Basin of Nepal Himalaya. *Climate*, 3, 210–226.
- [7] Liao, W.; Wang, X.; Fan, Q.; Zhou, S.; Chang, M.; Wang, Z.; Wang, Y.; Tu, Q. (2015). Long-term atmospheric visibility, sunshine duration and precipitation trends in South China. *Atmos. Environ.*, 107, 204–216.
- [8] Li, J., Zhu, Z., Dong, W. (2017). Assessing the uncertainty of CESM-LE in simulating the trends of mean and extreme temperature and precipitation over China. *Int. J. Climatol.*, 37, 2101–2110.
- [9] Adeyeri O. E, Lamptey B. L, Lawin A. E and Sanda I. S (2017): Spatio-Temporal Precipitation Trend and Homogeneity Analysis in Komadugu-Yobe Basin, Lake Chad Region *Journal of Climatology & Weather Forecasting* 5(3): 1-12
- [10] Oguntunde, P. G., Abiodun, B. J., Gunnar L. (2012). Spatial and temporal temperature trends in Nigeria, 1901–2000. *Meteorology and Atmospheric Physics* 118:95–105
- [11] Eshetu, G. Johansson, T. and Garedew, W (2016): Rainfall trend and variability analysis in Setema-Gatira area of Jimma, Southwestern Ethiopia 11(32), 3037-3045
- [12] Buffoni, L., Maugeri, M., Nanni, T., (1999): Precipitation in Italy from 1833 to 1996. *Theoretical and Applied Climatology* 63, 33–40.
- [13] Partal, T., Kahya, E., (2006): Trend analysis in Turkish precipitation data. *Hydrological Processes* 20, 2011–2026.
- [14] Wing H, Gabriel B, Ashbindu S (2008). Trends and Spatial distribution of annual and seasonal rainfall in Ethiopia. *Int. J. Climatol.* 28(13):1723-1734.
- [15] Oguntunde PG, Abiodun BJ, Lischeid G (2011) Rainfall trends in Nigeria, 1901-2000. *J Hydrol* 411: 207-218.
- [16] Ati O. F, Stitger CJ, Oladipo EO (2002) A comparison of methods to determine the onset of the growing season in northern Nigeria. *Int J Climatol* 22:731-742.
- [17] Ukoje, J. E. (2016): Impacts of rapid urbanisation in the urban fringe of Lokoja, Nigeria, *Journal of Geography Regional Planning.* 9(10), pp. 185-194,
- [18] Adetunji, M. A. and Isah, I. O (2015): Urban housing Quality and Its health implications in Nigeria: An example of Lokoja, Kogi State, Nigeria *Ethiopian Journal of Environmental Studies & Management* 8(5): 570 – 578, 2015
- [19] Adeoye, N. O. (2012). Spatio-temporal analysis of land use/cover change of Lokoja-a confluencetown. *Journal of Geography and Geology*, 4(4),40
- [20] Costa, J. A and Rodrigues, G. P. (2017): Space-time distribution of rainfall anomaly index (RAI) for the Salgado Basin, Ceará State – *Brazil science and Nature* 39 (3) 627-634
- [21] Tigkas, D, Vangelis, H., Tsakiris, G (2013) Proceedings of 8th International Conference of EWRA Water Resources Management in an Interdisciplinary and Changing Context Porto, Portugal, 26th-29th June 2013
- [22] Edwards, D.C., Mckee, T.B., (1997). Characteristics of 20th Century Drought in the United States at Multiple Time Scales, Atmospheric Science Paper No. 634, Climatology Report No. 97-2. Colorado
- [23] Viste, E., Diriba, K., Sorteberg, A., (2013): Recent drought and precipitation tendencies in Ethiopia. *Theor. Appl.*

- Climatol. 112, 535–551.
<https://doi.org/10.1007/s00704-012-0746-3>.
- [24] Arragaw, A., Woldeamlak, B., (2017). Local spatiotemporal variability and trends in rainfall and temperature in the central highlands of Ethiopia. *Geogr. Ann. Phys. Geogr.*
<https://doi.org/10.1080/04353676.2017.1289460>
- [25] Abaje, I.B., Ati, O.F., Iguisi, E.O. and Jidauna, G.G (2013): Droughts in the Sudano-Sahelian Ecological Zone of Nigeria: Implications for Agriculture and Water Resources Development *Global Journal of Human Social Science, Geography, Geo-Sciences & Environmental* 13(2)1
- [26] Oloruntade, A. J., Mohammad, T. A., Ghazalib, A. H., Wayayok, A., (2017): Analysis of meteorological and hydrological droughts in the Niger-South Basin, *Nigeria Global and Planetary Change* 155 (2017) 225–233
- [27] Akinsanola, A.A. and Ogunjobi, K.O., (2014): Analysis of rainfall and temperature variability over Nigeria. *Global Journal of Human-Social Science: B Geography, Geo-Sciences, Environmental Disaster Management*, 14 (3), 1–17.
- [28] Ogunrinde, A. T., Oguntunde, P. G. Akinwumiju, A. S and Fasinmirin, J. T. (2019): Analysis of recent changes in rainfall and drought indices in Nigeria, 1981–2015, *Hydrological Sciences Journal*, DOI: 10.1080/02626667.2019.1673396



Effect of Temperature and Residence Time on Torrefaction Characteristics of African Birch (*Anogeissus leiocarpa*)

Pious O. Okekunle*, Samuel Maduekwe, Gbenga S. Ajadi and Sanyaolu A. Olugbemisoye

Department of Mechanical Engineering, Faculty of Engineering and Technology, Ladoke Akintola University of Technology, P. M. B. 4000, Ogbomoso, Oyo state, Nigeria.

*Corresponding author's email and phone number: pookekunle@lautech.edu.ng +2348167643227

Received: 27.05.2020

Accepted: 09.10.2020

Published: 31.12.2020

Abstract- In this study, the effect of temperature and residence time on African birch (*Anogeissus leiocarpa*) torrefaction characteristics was investigated. African birch trunk was procured from Aanu-Oluwapo Sawmill in Ogbomoso, South-Western Nigeria. The trunk was sawn into pieces. The pieces were machined into cylindrical samples of 40 mm diameter and 65 mm length using a wood lathe machine (Powermatic 3520B). Prepared samples were torrefied, one at a time, in an electrically heated fixed bed reactor at different torrefaction temperatures (200, 230, 260, and 290 °C) and residence times (10, 20, 30, and 40 min). The proximate analysis of both the raw sample and solid torrefaction products was done according to the ASTM D3174-76 standard. The mass and energy yields, Higher Heating Value (HHV), and water absorption characteristic of the solid torrefaction products were then determined. Findings revealed mass and energy yields of the torrefied solid products decreased with an increase in both temperature and residence time. HHV increased with temperature but did not show any consistent pattern with residence time. The water affinity of the torrefied biomass decreased with both temperature and residence time. Torrefaction inhibits biomass moisture uptake during storage while increasing its heating value.

Keywords: Torrefaction, temperature, residence time, HHV, water absorption.

1. INTRODUCTION

The acceptance of biomass energy as a promising alternative to fossil fuels has resulted in many advancements regarding biomass conversion technologies. Aside from being available on a renewable basis, biomass is almost evenly spread across the globe, and is suitable for many biochemical and thermo-chemical conversion processes. The by-products from its conversion processes do not also threaten environmental health as those from fossil fuels. However, raw biomass possesses low bulk energy density, high moisture content, poor grindability, susceptibility to deterioration, and microbial and fungal attacks during storage. In order to extenuate these defects, thermal pretreatment of raw biomass, referred to as torrefaction, is being practiced. Torrefaction is a mild pyrolysis process within a temperature range of 200 – 300 °C over a residence time of several minutes to few hours [1, 2].

Previous studies have shown that torrefied biomass has reduced moisture content, increased energy density, improved hydrophobicity, better resistance to microbial attacks during storage [3-6] and closely resembles coal in quality [7]. During torrefaction, parameters influencing product characteristics include temperature, heating rate, reaction time, particle size, and feedstock type [8]. Many experimental studies have investigated the effect of these parameters on biomass torrefaction [9,10,11,12].

Modelling and simulation of torrefaction have also been attempted to understand the kinetics and transport interactions during the process [1,7,13,15,16]. In most of these studies, temperature and residence time effects on the water absorption characteristic of the torrefied sample was not reported. The wood samples used

were not also typical of West Africa. Therefore, in this study, the effects of torrefaction temperature and residence time on mass and energy yield, Higher Heating Value (HHV), and water absorption characteristics of African birch (*Anogeissus leiocarpa*) were investigated.

2. MATERIALS AND METHODS

2.1 Sample procurement and processing

African birch trunk was obtained from Aanu-Oluwapo Sawmill in Ogbomoso, South-Western Nigeria. The trunk was sawn into pieces. The pieces were machined into cylindrical samples of 40 mm diameter and 65 mm length by using a wood lathe machine (Powermatic 3520B) at the sawmill.

2.2 Experimental set-up

A fixed bed reactor, electrically heated, was set up for the experiments. The reactor consists of a furnace chamber, which houses a cylindrical retort, charged with the raw sample to be torrefied. A temperature controller, fed by signals from a thermocouple buried in the reactor, controls the bed's temperature. Two traps were used to trap the released condensable volatiles during the process. Figure 1 shows the exploded view of the reactor for the torrefaction process.

2.3 Experimental procedure

The biomass samples prepared were placed, one at a time, inside the retort in preparation for a run. The reactor was connected to the mains and set at an initial temperature value of 230 °C (30 °C higher than the desired temperature) in

$$\text{Mass yield} = \frac{\text{Mass of torre. biomass on DAF basis}}{\text{Mass of dried biomass on DAF basis}} \times 100\% \quad (3)$$

$$\text{Energy yield} = \frac{\text{Product mass} \times \text{HHV}_{\text{product}}}{\text{Raw feed mass} \times \text{HHV}_{\text{raw}}} \times 100\% \quad (4)$$

2.6 Water absorption

To study the effect of torrefaction on biomass water absorption characteristic, the weight of selected raw samples, and their corresponding torrefied solid products were measured. These were then submerged simultaneously to the same depth in 5 liters of water for 24 hours. The samples were then taken out of the water, and their weight

compensation for the heat loss due to retort insertion. When the reactor temperature attained the preset temperature of 230 °C, the reactor was opened. The retort was then placed in it. The reactor temperature then fell steadily towards 200 °C due to the heat absorbed by the retort and heat loss by convection. The reactor temperature was then set to 200 °C, and the sample was heated steadily for 10 min. The torrefied sample was taken out of the reactor after the specified time and cooled before its mass was measured. This procedure was repeated for other biomass samples at 20, 30, and 40 min. The entire process was followed for torrefaction temperatures of 230, 260, and 290 °C.

2.4 Proximate analysis

The proximate analysis of the raw sample and torrefied solid products was carried out according to the ASTM D3174-76 standard. The HHV of the raw sample and torrefied solid products were estimated according to [17] as expressed by equations 1 and 2, respectively.

$$\text{HHV}_{\text{raw}} = 0.1708 \text{ VM} + 0.3543 \text{ FC} \quad (1)$$

$$\text{HHV}_{\text{torrefied}} = 0.1846 \text{ VM} + 0.3525 \text{ FC} \quad (2)$$

Where VM and FC are the volatile matter and fixed carbon, respectively.

2.5 Determination of Mass and Energy Yield

Mass and energy yield after torrefaction were determined on a Dry Ash-Free (DAF) basis according to equations 3 and 4, respectively [18].

was measured and recorded. The weight of water absorbed was determined according to equation 5, given as

$$\text{Weight of water} = W_{s2} - W_{s1} \quad (5)$$

Where W_{s1} and W_{s2} are the weight of the sample before and after immersion, respectively.

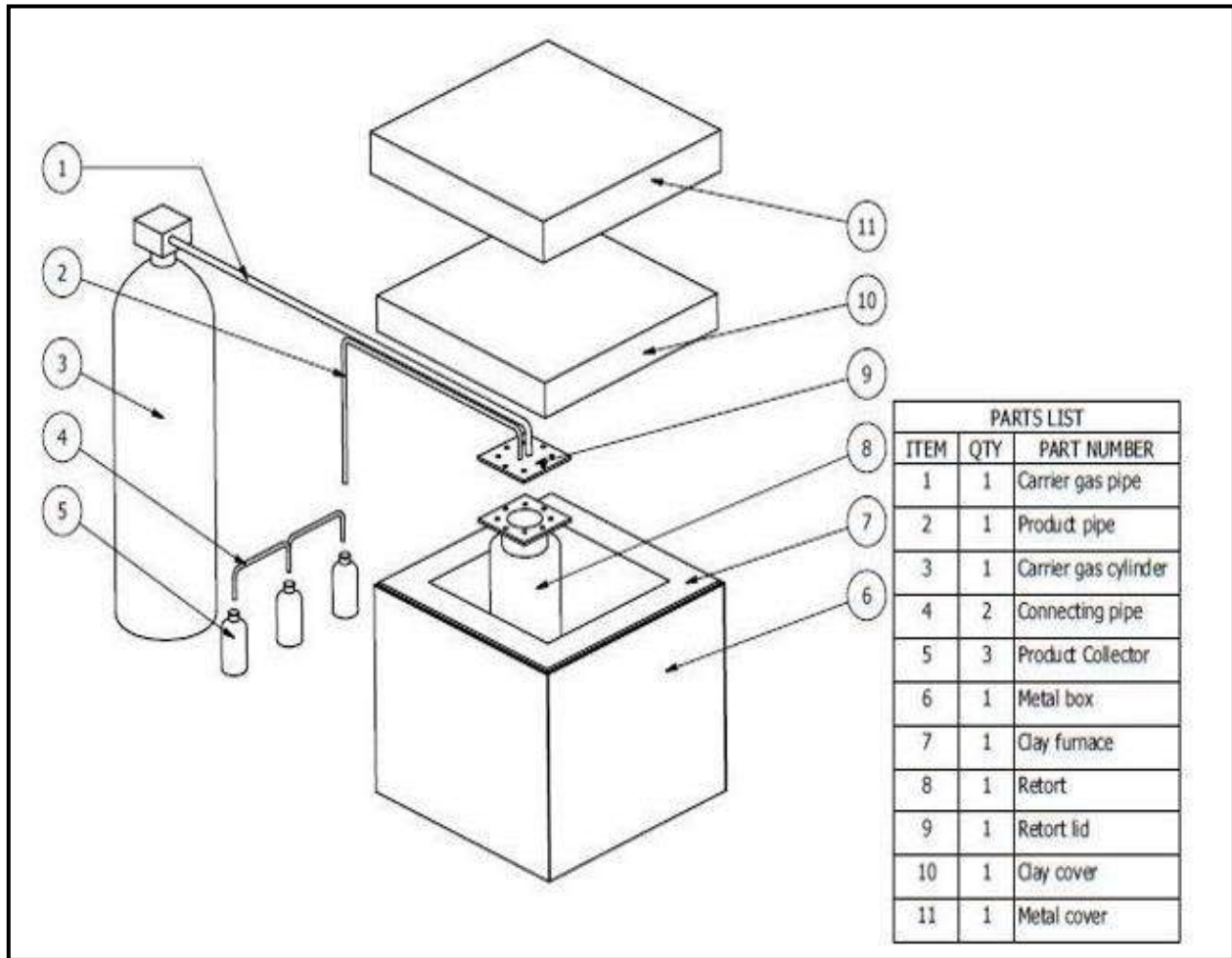


Figure 1: Exploded view of torrefaction fixed bed reactor

3. RESULTS AND DISCUSSION

3.1 Proximate analysis

Table 1 shows the proximate analysis of both the raw sample and torrefaction solid products. From the table, it can be seen that at 200 °C, percentage moisture content decreased with increase in residence time. However, this decrease did not follow any definite pattern. Also, at 200 and 230 °C, the percentages of fixed carbon and volatile matter at all residence times are not significantly different from those of the raw sample. However, as expected, the percentage moisture content decreased in compared to that of the raw sample. in residence time. This may be due to not too distant residence times used.

For 260 and 290 °C, the percentage of fixed carbon and ash increased while volatile matter decreased. At all temperatures and residence times considered, the ash content in the torrefaction products was higher than that of the raw sample. These results are in agreement with the findings of [19]. Figure 2 shows the variation of HHV of torrefied biomass at different temperatures and residence times. As shown in Figure 2, HHV generally increased with temperature [19] but did not show any definite pattern with change

Table 1: Proximate analysis of the raw sample and torrefaction solid products

Temperature (°C)	Time (min)	FC (%)	VM (%)	Ash (%)	Moisture content (%)
200	10	18.92	72.46	0.78	7.59
	20	25.54	69.58	1.06	3.82
	30	19.12	71.04	0.84	3.94
	40	18.24	70.69	0.67	4.11
230	10	25.19	70.25	0.85	3.71
	20	17.88	70.18	0.87	3.71
	30	24.15	71.47	0.33	3.75
	40	28.15	67.05	1.01	3.79
260	10	71.73	22.85	2.21	3.21
	20	70.60	23.65	2.31	3.44
	30	70.78	23.64	2.23	3.35
	40	70.43	23.76	2.42	3.36
290	10	71.65	22.78	2.26	3.39
	20	25.27	69.84	0.92	3.97
	30	69.81	24.56	2.34	3.29
	40	69.65	24.56	2.37	3.42
Raw sample		24.35	70.18	0.45	5.02

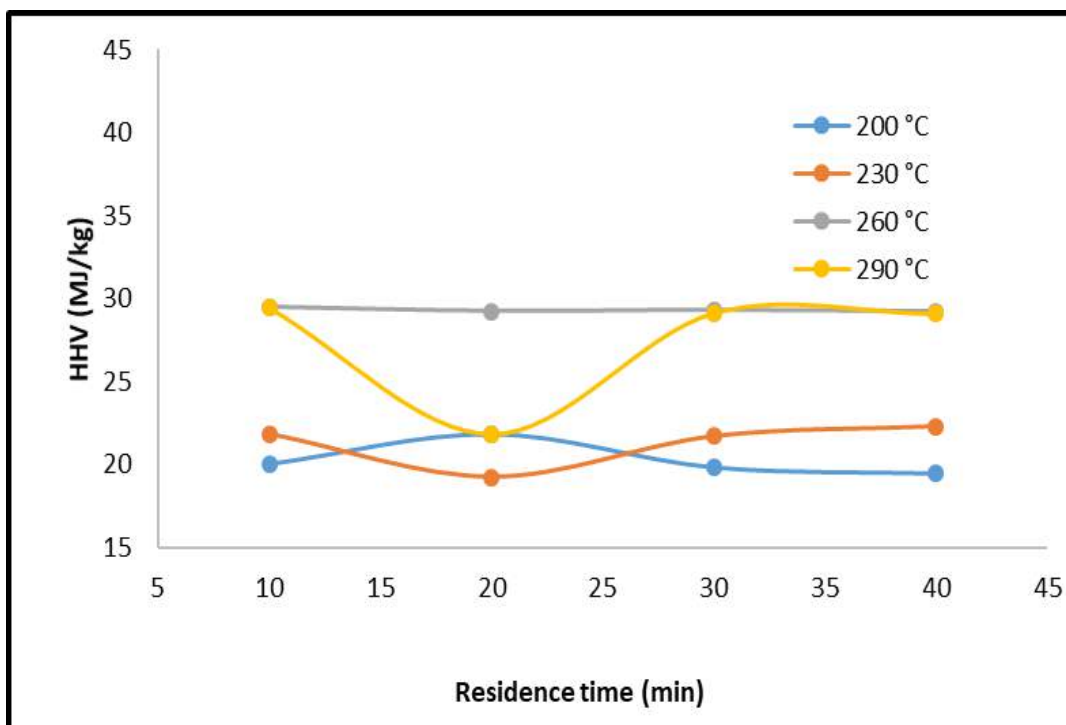


Figure 2: HHV at different torrefaction temperatures and residence times

Other researchers have reported some slight increase in HHV with residence time [19]. However, at 260 °C, HHV does not show any appreciable response to increased residence time.

3.2 Effect of temperature and residence time on mass and energy yield

Figure 3 shows the mass yield of solid torrefaction products at different temperatures and residence times. As shown in Figure 3, mass yield decreased with both temperature and residence time. An increase in temperature and residence time implies a higher degradation, which is usually associated with a greater release of biomass organics containing water, acetic acid, lactic acid, formic acid and furfural [18], hence the decrease in mass yield. These findings are in agreement with [19] and [20].

Figure 4 shows the energy yield of solid torrefaction products at different temperatures and residence times. From Figure 4, although no definite pattern at residence time of 10 min, energy yield generally decreased with temperature and residence time. The decrease in energy yield with temperature is in agreement with the findings of [1] and [20]. The decrease in

energy yield with residence time agrees with the findings of [23], who reported that mass and energy yields of biomass decreased with operating temperature and torrefaction residence time.

3.3 Effect of temperature and residence time on water absorption

Figure 5 shows the effect of temperature and residence time on the solid torrefaction products water absorption characteristics. From Figure 5, it can be seen that the weight of water absorbed by the torrefied solid decreased with both temperature and residence time. This implies wood, which is naturally hydrophilic, becomes hydrophobic, and the degree of hydrophobicity increases with torrefaction temperature and residence time. This is in agreement with the findings of [21], who reported that wood wettability change during heat treatment is more probably due to the plasticization of the lignocellulosic polymeric components of wood. Although the relation between hydrophobicity and fungi growth cannot be established, the chemical modification and degradation during torrefaction have been responsible for improved durability of torrefied solid products [22].

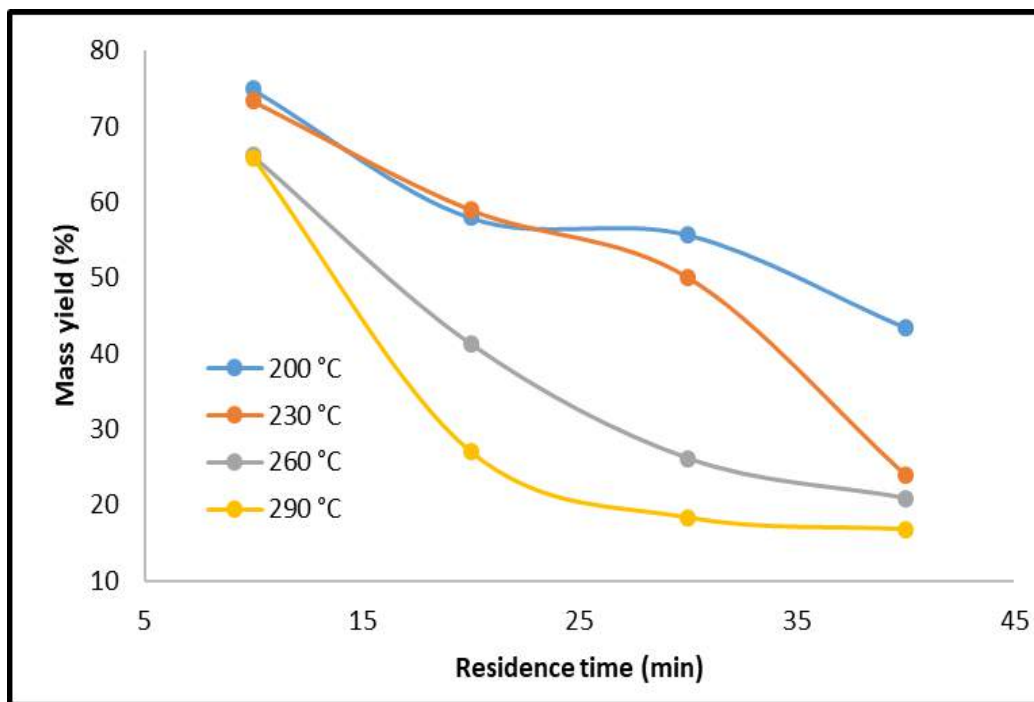


Figure 3: Mass yield at different torrefaction temperatures and residence times

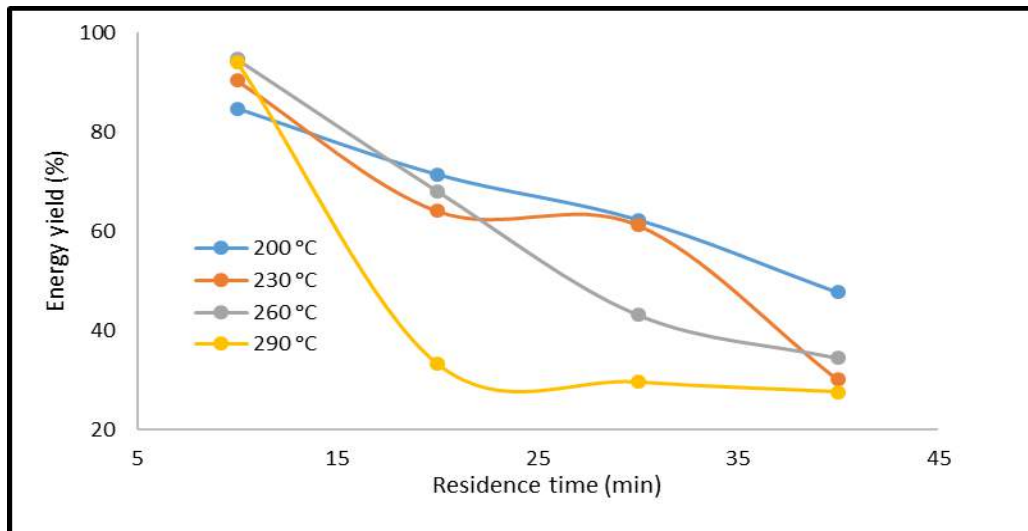


Figure 4: Energy yield at different torrefaction temperatures and residence times

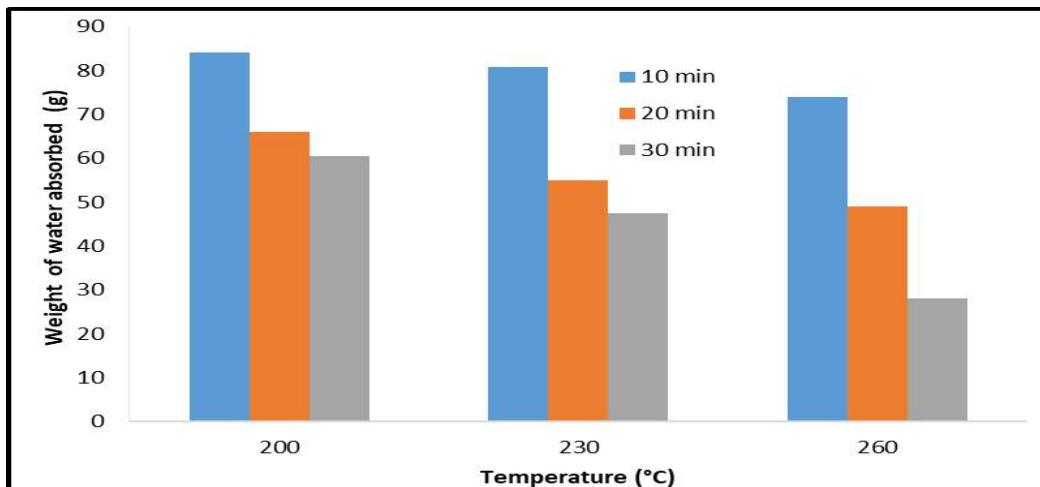


Figure 5: Water absorption of solid torrefaction products

4. CONCLUSION

Effects of temperature and residence time on torrefaction characteristics of African birch were investigated. Mass and energy yields decreased with increase in temperature and residence time. On the other hand, HHV increased with temperature but did not show any definite pattern with residence time. Results also showed that torrefaction limits water absorption in the solid torrefaction products. The degree of hydrophobicity increased with temperature and residence time. In all, the effect of temperature on the torrefaction characteristics of the woody biomass used was higher than that of residence time.

REFERENCES

- [1] Bates, R.B., and Ghoniem, A.F., (2014). Modeling kinetic-transport interaction during biomass torrefaction: the effect of temperature, particle size, and moisture content. *Fuel* 137, 216 – 229.
- [2] Li, H., Liu, X., Legros, R., Bi, X. T., Lim, C. J., and Sokhansanj, S., (2012). Torrefaction of sawdust in a fluidized bed reactor. *Bioresource Technology* 103, 453 – 458.
- [3] Kamdem, D. P., Pizzi, A., and Triboulot, M.C., (2000). Heat-treated timber: potentially toxic byproducts presence and extent of wood cell wall degradation. *Holz als Roh-und Werkstoff* 58, 253-257.

- [4] Stamm, A.J., (1956). Thermal degradation of wood and cellulose. *Industrial and Engineering Chemistry* 48, 413-417.
- [5] Hakkou, M., Petrissans, M., Gerardin, P., and Zoulalian, A., (2006). Investigations of the reasons for fungal durability of heat-treated beech wood. *Polymer Degradation and Stability* 91, 393-397.
- [6] Kamdem, D., Pizzi, A., and Jermannaud, A., (2002). Durability of heat-treated wood. *Holz als Roh-und Werkstoff* 60, 1-6.
- [7] Nordin, A., Pommer, L., Nordwaeger, M., and Olofsson, I., (2013). Biomass conversion through torrefaction, in: Strandberg, M., Olofsson, I., Pommer, L., Wiklund-Lindstrom, S., Aberg, K., and Nordin, A., (2015). Effect of temperature and residence time on continuous torrefaction of spruce wood. *Fuel Processing Technology* 134, 387 – 398.
- [8] Bates, R.B., and Ghoniem, A. F., (2012). Biomass torrefaction: modeling of volatile and solid product evolution kinetics. *Bioresource Technology* 124, 460 – 469.
- [9] Sadaka, S., and Negi, S., (2009). Improvement of biomass physical and thermochemical characteristics via torrefaction process. *Environ. Prog. Sust. Energy* 28(3), 427 – 434.
- [10] Rodrigues, T.O., and Rousset, P. L. A., (2009). Effects of torrefaction on energy properties of *Eucalyptus grandis* wood. *Cerne, Lavras* 15(4), 446 – 452.
- [11] Yusup, S., Aminuddin, A., Azian, M. T., Abdullah, S. S., and Sabil, K. M., (2010). Improvement of risk husk and coconut shell properties for enhancement of gasification process. *Third International Symposium on Energy from biomass and Waste, Venice, 8 – 11 by CISA, Environmental Sanitary Engineering Centre, Italy.*
- [12] Repellin, V., Govin, A., Rolland, M., and Guyonnet, R., (2010). Modelling anhydrous weight loss of wood chips during torrefaction in Pilot kiln. *Biomass Bioenergy* 34(5), 602 – 609.
- [13] Peduzzi, E., Boissonnet, G., Haarlemmer, G., Dupont, C., and Marechal, F., (2014). Torrefaction modeling for lignocellulosic biomass conversion processes. *Energy* 70, 58-67.
- [14] Okekunle, P.O., (2019). Modelling and simulation of intra-particle heat transfer during biomass torrefaction in a fixed-bed reactor. *Biofuels*, DOI: 10.1080/17597269.2019.1637071 .
- [15] Artiukhina, E., and Grammelis, P., (2015). Torrefaction of biomass pellets: modeling of the process in a fixed bed reactor. *International Journal of Chemical, Molecular, Nuclear, Materials and Metallurgical Engineering* 9, 1433 – 1436.
- [16] Nikolopoulos, N., Isemin, R., Atsonios, K. et al., (2013). Modeling of wheat straw torrefaction, *Waste Biomass Valor* 4, 409–420.
- [17] Nhuchhen, D.R., and Afzal, M.T., (2017). HHV predicting correlations for torrefied biomass using proximate and ultimate analysis. *Bioengineering* 4(7), 1 – 15.
- [18] Basu, P., Rao, S., & Dhungana, A., (2012). An investigation into the effect of biomass particle size on its torrefaction. *Canadian Journal of Chemical Engineering* 91(3), 466 – 474.
- [19] Wannapeera, J., Fungtammasan, B., and Worasuwannarak, N. (2011). Effect of temperature and holding time during torrefaction on the pyrolysis behaviors of woody biomass. *Journal of Analytical and Applied Pyrolysis* 92, 99 – 105.
- [20] Bridgeman, T.G., Jones, J.M., Shield, I., and Williams, P.T., (2008). Torrefaction of reed canary grass, wheat straw and willow to enhance solid fuel qualities and combustion properties. *Fuel* 87, 844 – 856.
- [21] Hakkou, M., Petrissans, M., Zoulalian, A., and Gerardin, P., (2005). Investigation of wood wettability changes during heat treatment on the basis of chemical analysis. *Polymer Degradation and Stability* 89, 1–5.
- [22] Hakkou, M., Petrissans, M., Gerardin, P., and Zoulalian, A., (2006). Investigations of the reasons for fungal durability of heat-treated beech wood. *Polymer Degradation and Stability* 91, 393 – 397.
- [23] Pimchuai, A., Dutta, A., and Basu, P., (2010). Torrefaction of agriculture residue to enhance combustible properties. *Energy Fuels* 24, 4638 – 4645.



Effect of Welding Using Electrodes with Certain Treatment on Stainless Steel 304 Using SMAW Welding

Iswanto ^{1*}, Ribangun B. Jakaria ², Mulyadi ^{1,3}, M. Sofwan Hariadi ¹

¹ Department of Mechanical Engineering, Muhammadiyah University of Sidoarjo, Sidoarjo, Indonesia.

² Faculty of Design Innovation & Technology, Sultan Zainal Abidin University, Terengganu, Malaysia.

³ Department of Mechanical Engineering, Sepuluh Nopember Institute of Technology, Surabaya, Indonesia.

*Corresponding author. Email address: iswanto.sda@gmail.com

Received: 15.06.2020

Accepted: 26.10.2020

Published: 31.12.2020

Abstract- This paper will discuss how the influence of welding electrodes which before being used in the welding process is given a certain treatment first. The treatment is given to the welding electrode before the welding process is by dipping the welding electrode into the oil and dipping the welding electrode into the coolant. The effect of the welding electrode treatment on the SMAW welding results seen from the tensile strength. The specimen used is stainless steel type 304 with four welding variations. First, welding is carried out on type 304 stainless steel by using welding electrodes of type E308 Gutwelt. Second, welding using Nikko Steel type E308 welding electrodes. Third, welding using Nikko Steel type E308 welding electrodes that are oil dipped. Fourth, welding uses Nikko Steel type E308 welding electrodes which are dyed coolant. After tensile testing of the welding results, the results are obtained: welding using Gutwelt type E308 welding electrodes has greater tensile strength compared to using Nikko Steel type E308 welding electrodes. While welding using Nikko Steel type E308 welding electrodes that have been carried out certain treatments, namely by dipped coolant, produce greater tensile strength compared to using the Gutwelt type E308 welding electrodes. However, in welding using Nikko Steel type E308 welding electrodes that are oil dipped, the tensile strength is still lower than using a Gutwelt type E308 welding electrodes.

Keywords: Stainless steel type 304, Welding electrodes, SMAW welding, Certain treatment

1. INTRODUCTION

Stainless steel is a type of metal that is widely used in everyday life. Stainless steel has various types, one of which is stainless steel type 304 [1]. Stainless steel 304 is the most versatile stainless steel and is most widely used for various needs. With its special properties, 304 stainless steel is widely used both in the household and industrial sectors [2]. Its uses include, among others, household material, building industry, medical and laboratory equipment, piping systems and others [3]. This type has excellent forming and welding characteristics [4,5]. In the fabrication process, metal fusion is the most important process for fabrication components. To combine metals, the welding process is most widely used due to

various considerations [6]. Welding is a metallurgical bond in an alloy metal connection which is carried out in a melted or liquid state [7,8]. In the scope of welding there are various kinds of welding that occur, one out of various welding method is shielded metal arc welding (SMAW). This type of welding is included in the category of liquid welding with arc media (electrodes) as filling fluid [9,10].

SMAW welding is a method of the fusion welding process to combine two pieces of metal by melting the edges with an electric arc between two conductors. The electrode is one conductor and the workpiece is another conductor [11]. In arc welding, shielded metal arc welding (SMAW) is usually used in the

welding process in most industries, because it is economical and easy to carry [6,12]. In the welding process using an electric arc, required electrodes or better known as welding wires. Electrodes consist of a single core, which is metal and is coated by a layer that is mixed with chemicals [4,13].

The types of electrodes on the market are numerous and have different prices and quality of welding results. Usually between price and quality are directly proportional, the more expensive the price of electrodes, the better the quality of welding results. No exception to the electrodes used for stainless steel welding. For small welding shops the difference in price of welding electrodes is very calculated, because it will affect the price of the products they make. Electrodes are usually chosen at low prices, although the quality of welding results is not good [14]. Therefore, it is necessary to do research on how the welding electrodes which have poor quality become better by means of specific treatments.

Previous studies have tested the effect of oil dipped AWS 5.1 E 6013 electrodes flux on FC 25 gray cast iron welding on tensile strength. And the result is that, welding electrodes dipped in oil before the welding process is able to increase the tensile strength of welding results [14]. Here will be discussed about the comparison between the results of welding using Gutwelt welding electrodes type E308 with welding results using Nikko Steel type E308 electrodes on stainless steel type 304 in terms of tensile strength.

As well as whether there is an influence of the oil immersion and coolant treatment on the Nikko Steel E308 welding electrodes used in welding stainless steel type 304 seen from the results of the tensile test.

2. MATERIALS AND METHODS

The material used in this study is stainless steel type 304 and the welding machine used is AC welding machine Lakoni MMA Inverter model FALCON 141 GE. In the welding process using Gutwelt type 308 welding electrodes and Nikko Steel type 308 welding electrodes. while for the Nikko Steel electrode type E308 before being used for the welding process plus two treatments

namely: first dipped in oil and second dyed coolant. The welding process uses a strong current of 90 Amperes. Welding seam used is type seam V, angle 60 with a gap width of 2 mm.

After the welding process using four different types of welding electrodes is completed, then testing the results of welding. Testing of welding results is divided into two, non-destructive testing and destructive testing [15]. For non-destructive testing, in this study using the dye penetrant test method. The working principle of the dye penetrant test is that a penetrant liquid of a certain color (red) permeates the discontinuity, then the liquid penetrant is removed from the discontinuity by using a developer fluid whose color contrasts with the penetrant (white). Detection of discontinuity is by the appearance of red spots (liquid penetrant) that come out of the discontinuity [7]. Testing is carried out with the aim to find out the quality of the welding process whether it meets the requirements or not.

After the welding results are declared to have met the requirements, the next step is to do destructive testing. The destructive test chosen is the tensile test of the specimen that has been made. Tensile testing is a destructive testing method that aims to determine the strength of the material by giving a linear load [16]. For tensile testing in accordance with ASTM (American Society for Testing and Materials) A 240 standards on welding workpieces. There are mainly two types of standard dimensions, one for plates and one for rod type specimens [11]. So the selection of standard tensile test specimens in this study is plate type.

3. RESULTS AND DISCUSSION

3.1 Dye Penetrant Test

Dye penetrant tests were carried out in order to find out the quality of the welding process using different welding electrodes, whether or not they met the requirements. The results of welding using Gutwelt type E308 welding electrodes, after the dye penetrant test is performed looks like in Figure 1.



Figure 1: Dye penetrant test results welding proses using gutwelt welding electrodes

From Figure 1 shows that SMAW welding using Gutwelt type E308 welding electrodes only slightly experienced welding defects, namely in the specimen (AII). Welding defects that occur due to the welding operator expertise. Welding using the Nikko Steel type E308 welding electrode after dye penetrant test results are shown in Figure 2.



Figure 2: Dye penetrant test results welding process using nikko steel welding electrodes

From Figure 2 it can be seen that the SMAW welding using the Nikko Steel type E308 welding electrode occurs only slightly welding defects, namely in the specimen (BIII). The defect is caused by the expertise of the welding operator. Welding results using welding electrodes Nikko Steel type E308 oil dipped, after the dye penetrant test can be seen in Figure 3.



Figure 3: Dye penetrant test results welding process using welding electrodes nikko steel with dipped in oil

Figure 3 shows that the SMAW welding using weld electrode Nikko Steel type E308 with dipped in oil only slightly occurred welding defects, namely in the specimen (CI), even that is caused by the operator expertise. Welding using welding electrodes Nikko Steel type E308 dipped in coolant, after the dye penetrant test is done the results look like in Figure 4.



Figure 4: Dye penetrant test results welding process using nikko steel electrodes which are coolant dipped

From Figure 4, it can be seen that SMAW welding using Nikko Steel type E308 weld electrodes that are dyed with coolant only slightly causes welding defects, but evenly on all specimens. This is also caused by the operator expertise factor. Dye penetrant tests that have been carried out on all the results of the welding process with various treatments, indicate that the welding results meet the

requirements and subsequently carried out tensile test.

3.2 Tensile Test From the tensile test conducted on the specimens of each welding treatment, among others: First, welding is carried out on type 304 stainless steel by using welding electrodes of type E308 Gutwelt. Second, welding using Nikko Steel type E308 welding electrodes. Third, welding using Nikko Steel type E308 welding electrodes that are oil

dipped. Fourth, welding uses Nikko Steel type E308 welding electrodes which are dyed coolant. From the test results obtained data as in table 1. Each welding treatment was to tensile test three times to obtain more accurate data.

To make it easier to compare the results of tensile testing of each welding treatment, then from Table 1 can be made a graph as presented in Figure 5.

Table1: Tensile test result

Welding Process	Tensile Strength (N/mm ²)	Yield strength (N/mm ²)	Strain (%)
Gutwelt electrodes	119.73	96.03	28.27
Nikko Steel electrodes	117.60	85.76	27.00
Nikko Steel electrodes dipped in oil	115.68	76.04	40.27
Nikko Steel electrodes dipped in coolant	121.39	75.1	41.03

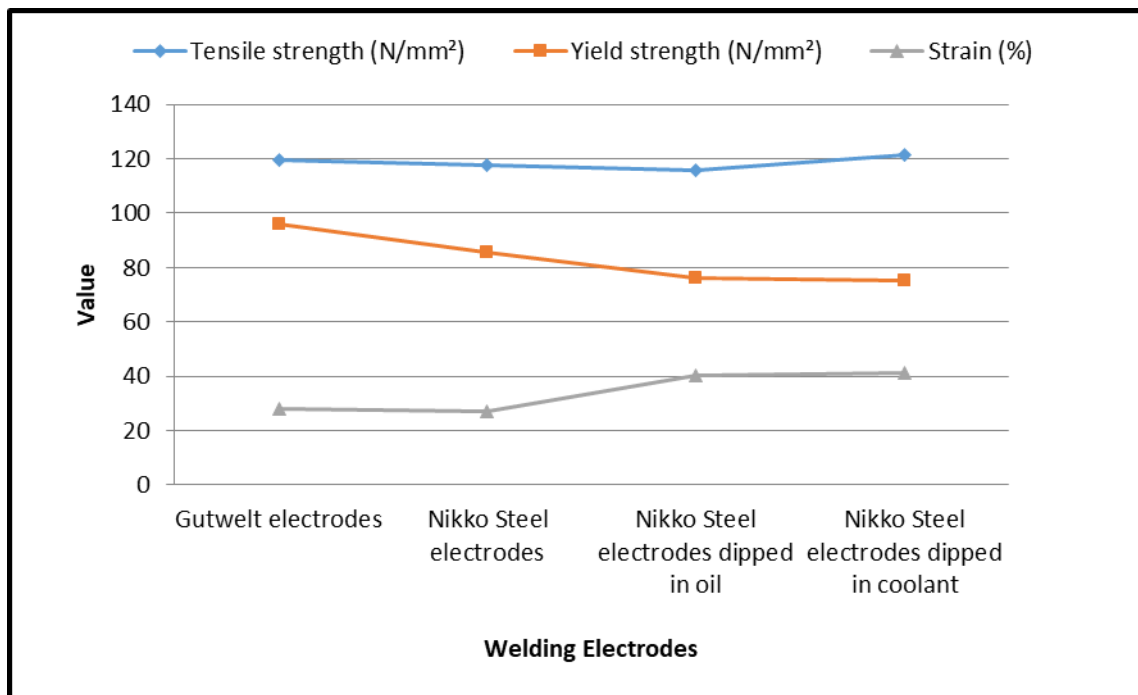


Figure 5 Graph of the tensile test results of each welding treatment

From Table 1 and Figure 5 it can be seen that welding stainless steel type 304 using welding electrodes Gutwelt type E308 has higher tensile strength compared to welding using Nikko Steel type E308 weld electrodes or using Nikko Steel type E308 weld electrodes dipped in oil. However, welding using Gutwelt E308 welding electrodes has a smaller tensile strength when compared to welding using Nikko Steel E308

welding electrodes that are dyed coolant first before being used for the welding process.

The results of the welding process stainless steel type 304 using welding electrode Gutwelt type E308 produce greater yield strength when compared to welding results using Nikko steel type E308 welding electrode and welding results using Nikko steel type E308 welding

electrode that were previously dipped in oil or dipped in coolant.

The welding process using Gutwelt type E308 welding electrodes has a greater strain when compared to welding using Nikko Steel type E308 welding electrodes. But welding using Gutwelt type E308 welding electrodes has a lower strain when compared to welding using Nikko Steel type E308 welding electrodes that are oil dipped or Nikko Steel type E308 welding electrodes that are dyed coolant.

The lowest tensile strength is obtained from the welding process using an oil dipped Nikko Steel type E308 welding electrode, which is 115.68 N/mm². While the highest tensile strength is generated from the welding process using Nikko Steel type E308 welding electrodes dipped in coolant, which is 121.39 N/mm².

From the results of the welding process using Gutwelt type E308 welding electrodes has the highest yield strength value, which is 96.03 N/mm². The lowest yield strength value is produced from a welding process that uses Nikko Steel type E308 welding electrodes with coolant dipped, amounting to 75.1 N/mm².

The smallest strain is produced from welding using Nikko Steel type E308 welding electrodes, valued at 27%. The biggest strain obtained from the welding process with Nikko Steel type E308 welding electrodes dipped in coolant, which is 41.03%.

4. CONCLUSIONS

Based on the analysis of the results of tensile testing on each welding treatment, it can be concluded that:

i. Certain treatment on Nikko steel type E308 weld electrodes, in this case the treatment of the welding electrode is by dipped in oil and dipped coolant before being used for the welding process, affecting the tensile strength of welding result stainless steel type 304. Where, if the welding electrode Nikko steel type E308 is dipped in oil the tensile strength of the welding results decreases and vice versa, if the welding electrode Nikko steel type E308 is dyed coolant the tensile strength of the welding results is higher.

ii. Certain treatment of Nikko steel type E308 welding electrode affects the value of the yield strength of stainless steel type 304 welding results. The value of yield strength decreases when before it is used for the welding process, Nikko steel type E308 weld electrode dipped in oil or coolant dipped.

iii. Certain treatment of Nikko steel electrode type E308 also affects the value of the strain of results welding stainless steel type 304. Which, from the two treatments of Nikko steel type E308 weld electrodes, results in higher strain values. And the highest strain value was obtained in the Nikko steel type E308 welding electrodes which were dyed coolant.

REFERENCE

- [1] Davis JR. (1994). ASM Specialty Handbook: Stainless Steel. In: ASM Handbook. ASM International.
- [2] Sharifitabar M, Halvae A, Khorshahian S. (2011). Microstructure and mechanical properties of resistance upset butt welded 304 austenitic stainless steel joints. Iran, Elsevier Journal of Materials and Design, 32(7): 3854–3864.
- [3] Galvis EAR, and Hormaza W. (2011). Characterization of failure modes for different welding processes of AISI/SAE 304 stainless steels. Colombia, Elsevier Journal of Engineering Failure Analysis, 18(7): 1791–1799.
- [4] Lippold JC, Kotecki DJ. (2005). Welding metallurgy and weldability of stainless steels. New Jersey: Wiley Inter-Science.
- [5] Padilha AF, and Rios PR. (2002). Decomposition of austenite in austenitic stainless steels. ISIJ International, 42(4): 325–37.
- [6] Bansod AV, and Patil AP. (2017). Effect of welding processes on microstructure, mechanical properties, and corrosion behavior of low-nickel austenitic stainless steels. Springer Journal of Metallography, Microstructure, and Analysis, 6(4): 304–314.
- [7] Kou, Sindo. (2003). Welding Metallurgy. 2nd ed. New Jersey: A John Wiley & Sons Inc.

- [8] Baskoro AS, Indra Milyardi, Amat MA. (2020). The effect of welding parameter on mechanical properties and macrostructure of AA1100 using autogenous TIG welding. *International Journal of Automotive and Mechanical Engineering (IJAME)*, 17(1): 7562-7569.
- [9] Linnert G. (1965). *Welding Metallurgy*. 3rd ed. vol. 1. American Welding Society.
- [10] Widodo, E., Iswanto, I., Nugraha, M. A., & Karyanik, K. (2018). Electric current effect on mechanical properties of SMAW-3G on the stainless steel AISI 304. *MATEC Web of Conferences*, 197, 12003.
- [11] Gowthaman PS, et al. (2017). Review on mechanical characteristics of 304 stainless steel using SMAW welding. *MASK International Journal of Science and Technology*, 2(2): 32-37.
- [12] Iswanto, Noerdianto, A'razy Fachruddin and Mulyadi (2020). Comparative analysis of the strength result of TIG welding and MIG welding on aluminum 5083. *TURBO Journal*, 9(1): 87-92.
Original title: Analisa perbandingan kekuatan hasil pengelasan TIG dan pengelasan MIG pada Aluminium 5083.
- [13] Lakshminarayanan AK, Balasubramanian V, Elangovan K. (2009). Effect of welding processes on tensile properties of AA6061 aluminum alloy joints. *The International Journal of Advanced Manufacturing Technology*, 40(3): 286-296.
- [14] Hermanto A, and Iswanto. (2018). Effect of electrodes AWS 5.1 E 6013 that oil dipped on FC-25 gray cast iron welding on tensile strength. *REM Journal*, 3(2): 57-60.
Original title: Pengaruh flux elektroda AWS 5.1 E 6013 dicelup oli pada pengelasan besi cor kelabu FC-25 terhadap kekuatan tarik.
- [15] American A, Standard N. (2007). *Standard methods for mechanical testing of welds*. AWS B4.0.
- [16] Winarno R, Daryono, Jufri M. (2018). The influence of welding ampere range to ST-40 shear strength with butt joint. *JEMMME*, 3(2): 113–118.



Optimum Portland Cement-Guinea Corn Husk Ash Blend as Filler in Hot Mix Asphalt

Abdulummin Ahmed Shuaibu, Aliyu Mani Umar, Hassan Suleiman Otuoze, *Ashiru Mohammed and Aminu Muhammad Abba

Department of Civil Engineering, Ahmadu Bello University, Zaria 810107, Nigeria

*Corresponding Author: ibshazali03@gmail.com (+2348036061389)

Received: 11.07.2020

Accepted: 24.11.2020

Published: 31.12.2020

Abstract- Dwindling natural resources and the negative environmental impact that comes with the industrial processing of construction materials. They are driving forces to man's quest for cleaner (green) and cheaper alternative construction materials. Among such alternatives include agricultural wastes. Guinea corn husk ash (GCHA), an agricultural waste obtained from the incineration of Guinea corn husk, has shown potentials of been used as filler material in hot mix asphalt due to its pozzolanic properties. Thus, this research aims to assess the strength and durability properties of hot mix asphalt with the incorporation of GCHA as a partial replacement for filler (cement). Marshal mix design method was used to determine the optimum bitumen content (OBC) at no GCHA content (control mix) within the bitumen content range prescribed by Nigerian general specifications for roads and bridges (NGSRB) for bituminous courses in flexible pavements. This OBC was used to determine the optimum GCHA by replacing the primary filler with GCHA up to 45% increments of 5%. Marshal indices and volumetric properties of samples prepared at each replacement level were determined according to relevant standards. Mixtures containing up to 20% Portland cement replacement with GCHA were found to produce competitive results against the control mix (only cement as filler). Thus, Marshall indices and volumetric properties of mixtures containing up to 20% cement replacement GCHA satisfy the minimum requirements prescribed by NGSRB for hot mix asphalt to be used as binder course in flexible pavements.

Keywords: hot mix asphalt; mineral filler; Marshall mix design; waste management; guinea corn husk ash

1. INTRODUCTION

Generally, asphalt concrete is composed primarily of aggregates and asphalt binder. Hot mix asphalt (HMA) concrete or simply hot mix asphalt (HMA) is a type of asphalt concrete that requires heating the concrete constituents (to a specific temperature) prior to transport, placement, and compaction [1]. Apart from the two components mentioned above, an excellent material referred to as filler is present in HMA mixtures. Fillers contain particles passing B.S. sieve No. 200 (sieve aperture of 75 μ m) and can occur naturally within the aggregates or are added

from foreign materials. When added from foreign materials, fillers often participate in chemical processes within the hot mix asphalt. Hydrated lime, for example, is described as an "active filler" due to its ability to reduce chemical aging of bitumen and stiffen the mastic more than a conventional filler (one naturally occurring within the crushed aggregate) above room temperature [2].

Primarily, fillers are incorporated into HMA to fill voids in coarser aggregates, thereby increasing the density, stability, and toughness of

a conventional bituminous paving mixture. Another function of fillers in HMA is filler-asphalt mastics, which serves as a cementing agent in HMA [3]. Hence, HMA is practically a mixture of aggregates and mastic coatings [4]. Also, fillers play an important role concerning stripping or moisture damage in HMA [5].

In Nigeria and some parts of the world, Portland cement (P.C.) is the commonly used as filler in HMA. High cost and environmental concerns associated with this material's production are primarily the reasons for growing interest in exploring suitable alternatives to P.C. as filler material in HMA. In Nigeria, for example, cement costs about 183% higher than the global average cost [6]. As such, researchers sought alternatives to P.C. from inexpensive materials. One such alternative comes from solid wastes. Since these materials are already byproducts of other processes (e.g., agricultural, industrial, municipal, etc.), it implies there are almost no costs and environmental concerns associated with their production. Rapid industrialization and other activities of man leave behind huge amounts of these wastes annually. This figure is as high as 42 million metric tons (MMT) in Nigeria [7]. Of the huge amount of waste generated annually in Nigeria, only a small percentage is recycled. The remaining finds its way to landfills or incineration plants. The limited capacity of landfills and alternative recycling means together with the carbon footprint from waste incineration present a serious challenge to the safe disposal of these wastes. For these reasons, researchers sought ways to expand the alternative means of recycling these wastes for sustainable waste management. One of such alternatives is incorporating them into the civil construction industry as construction materials. This, apart from saving the environment, will lessen the burden on excavating the ever-dwindling virgin resources for use in the construction industry.

Experimentally, several wastes from various sources have been investigated for use as an alternative filler in HMA. Industrial wastes such as fly ash and coal waste powder produce HMA with better flexibility behavior than HMA containing cement-based filler material [8, 9]. Other industrial wastes, when used as fillers at

various percentages such as cement kiln dust [10], waste foundry sand [11], limestone dust [12], etcetera, are found to improve the performance of HMA.

Among agricultural wastes, up to 50% replacement of limestone dust with rice husk ash as filler improves the stability, volumetric properties, and long-term performance of HMA [13]. However, Arabani et al. [14] observed that HMA prepared with rice husk ash as filler tends to have larger air voids and is susceptible to moisture damage. The authors recommend its use as filler only in arid regions or regions where the probability of moisture damage is low. Sugarcane bagasse ash is another agricultural use that has shown promising results as filler material in HMA. Sugarcane bagasse ash is found to improve stability, flow, and resilient modulus of HMA by 0.6%, 4.9%, and 17.4%, respectively, compared to HMA prepared with P.C. as filler [15]. We refer readers interested in an extensive study on how various solid wastes perform as filler material in hot mix asphalt to a recent survey paper by Choudhary et al. [16].

Guinea corn, also known as Sorghum, is a staple food, livestock feed. It has been used to produce bioethanol in many parts of the world. Guinea corn is the fifth most produced grain globally [17] and, of the 57.3 MMT estimated global production of guinea corn in 2020, Nigeria accounts for about 6.9 MMT [18]. It is among the significant foods consumed, especially in Northern Nigeria [19]. As the production of Guinea corn soars, there is an equal increase in Guinea corn husk (GCH). GCH is inexpensive biomass that is obtained as a residue after the cut crop has been threshed. GCH has found applications in the textile industry as a source of Sorghum husk extract for dyeing [20] and amorphous silica for various industrial applications [21]. However, in Nigeria, this residue is mostly left in the threshing fields and incinerated in an open field or tilled into the soil in preparation for the next farming season. GCH, when incinerated to produce Guinea corn husk ash (GCHA), is rich in silica [21], therefore has the potential to be used as a pozzolana. Several types of research have been conducted to ascertain the viability of using this material as a supplementary binder in cement concrete [19],

lateritic concrete [22]; as a stabilizer in lateritic soil for road construction [23], and as an extender (additive) in oil-well cement slurries [24]. GCHA at various quantities is found to perform well in these experiments.

This research derives motivation from the performance of GCHA mentioned in the experiments above. It aims to determine the optimum blend of P.C. and GCHA as filler in HMA for which the asphalt concrete can be used in pavement construction. The rest of the paper is structured as follows. Materials preliminary assessment according to relevant standards and mix design to obtain optimum bitumen content of HMA are presented in the next section. Experimental results on the performance of HMA at different proportions of the blended filler are discussed in section 3, and we end the paper with some conclusions in section 4.

2. MATERIALS AND METHODS

2.1. Materials

Materials used in the production of HMA include aggregates (coarse and fine), bitumen, and filler material (Portland cement and GCHA). A detailed description of material sourcing, processing, and properties is given below.

2.1.1. Bitumen

The bitumen used in this study was obtained from gidan kwalta Zaria, Kaduna state- Nigeria, and **Table 1** shows its physical characteristics and standard used for each test. Based on test results on the bitumen shown in **Table 1**, the bitumen can be classified as 85/100 penetration grade bitumen [25] and satisfies all standard requirements for use as a binder in HMA.

Table 1: Physical Characteristics of bitumen

Test conducted	Standard	Result
Penetration at 25 ⁰ C, 0.1mm	ASTM D5 [26]	87.2
Softening point (°C)	ASTM D36 [27]	49.5
Flash-point (Cleveland open cup) °C	ASTM D92 [28]	248
Fire-point (Cleveland open cup) °C	ASTM D92 [28]	256
Ductility at 25 ⁰ C, cm	ASTM D113 [29]	116
Specific gravity at 25 ⁰ C, (g/cc)	ASTM D70 [30]	0.98
Solubility in trichloroethylene, %	ASTM D2042 [31]	99

2.1.2 Aggregates

Crushed aggregates (fine and coarse) obtained from a quarry site in Zaria-Nigeria were used in this research.

Table 2 shows the physical characteristics of the aggregates, standard specifications used for each

test, and results obtained. The results obtained are within the specifications of NGSRB.

Table 2: Physical characteristics of aggregates

Test conducted	Standard	Result
Aggregate crushing value (%)	BS 812-110 [32]	20
Aggregate impact value (%)	BS 812-112[33]	22.2
Specific gravity	ASTM C127 & C128 [34, 35]	2.61 2.63*
Water absorption (%)	ASTM C127 & C128 [34, 35]	0.48 8.62*

Note: Values with an asterisk (*) are for fine aggregates others are for coarse aggregates.

2.1.2.1 Aggregate Proportioning and Blending

NGSRB requires that the all-in-aggregate gradation to be used in HMA must lie within the envelope shown in **Figure 1**. In this study, coarse aggregate (material retained on 4.75 mm sieve with a maximum aggregate size of 25 mm). Fine aggregate (material passing 4.75 mm sieve and

retained on 200 µm sieve), and mineral filler (material passing 200 µm sieve) were proportioned by trial and error and blended until an all-in-aggregate satisfying NGRSB requirement is obtained. **Figure 1** shows the particle size distribution curve of the all-in-aggregate used in this study.

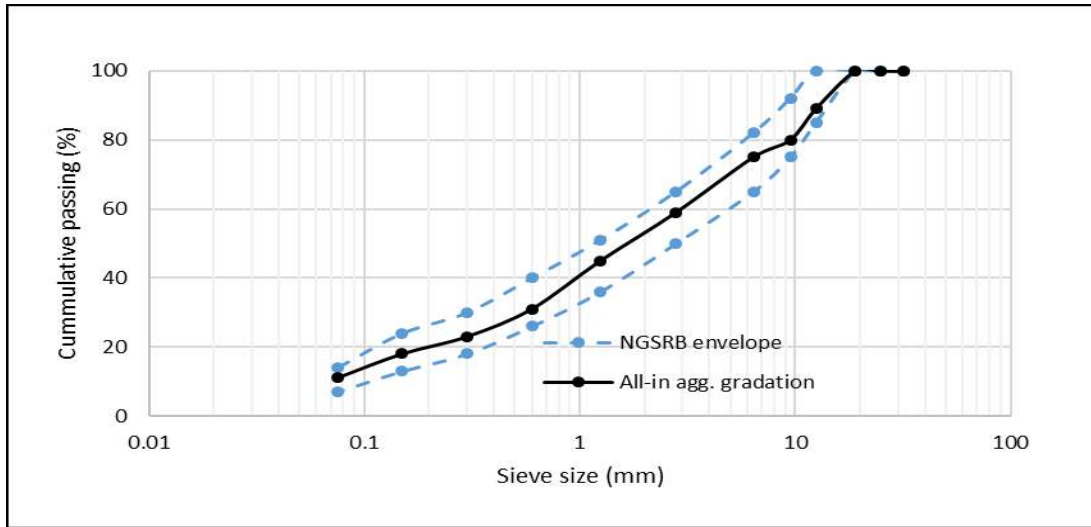


Figure 1: Gradation curve of all-in aggregates (According to BS 812-103.1 [36]).

2.1.3 Fillers

There are two materials used as fillers in this research; Portland cement and Guinea-corn husk ash (GCHA). Portland cement is the reference filler material and is partially replaced at various percentages with GCHA to obtain a blended filler material. The blended filler is obtained by

partially replacing cement up to 45% in increments of 5%. The Dangote 3X cement brand used in this study was obtained from a cement depot in Samaru, Zaria-Nigeria. **Table 3** shows the physical properties of filler materials and the standard used for each test.

Table 3. Physical properties of filler materials

Test	Standard	Result
Initial setting time (min)	BS EN 196-3 [37]	125
Final setting time (min)	BS EN 196-3 [37]	205
Soundness (mm)	BS EN 196-3 [37]	1.0
Specific gravity	ASTM C188 [38]	3.10 2.17*

Note: Value with an asterisk (*) is for GCHA while others are for P.C.

Guinea corn husk was obtained from a farm in Zaria-Nigeria. Foreign materials in the sample were handpicked, and the clean sample was burnt in an electric furnace for 3 hours at 700°C. This burning time and temperature are found to yield the optimum pozzolanic activity in GCHA [39]. The ash was collected from the furnace, allowed to cool, and sieved through B.S. sieve No. 200 to

obtain a material that satisfies the particle size requirements. A chemical composition test on the GCHA (**Table 4**) was carried out according to ASTM C311 [40] to determine the pozzolanic activity of a random sample. The result showed that silica + alumina + iron oxide is above 70% (74.6%). Thus, it can be adjusted to a pozzolana of class N following ASTM C618 [41].

Table 4. Chemical composition of GCHA.

Composition	Concentration (%)	Composition	Concentration (%)
Na ₂ O	0.747	SO ₃	1.772
MgO	4.052	Cl	1.620
Al ₂ O ₃	2.365	K ₂ O	7.615
SiO ₂	72.178	CaO	3.569
P ₂ O ₅	4.857	TiO ₂	4.857
Cr ₂ O ₃	0.000	Mn ₂ O ₃	0.054
Fe ₂ O ₃	0.0831	ZnO	0.030

2.2. Optimum bitumen content

Marshall method was used to determine the optimum bitumen content (OBC) using HMA containing 100% P.C. filler as the reference (control) mix. For this, 15 samples of the reference mix (3 samples each at varying bitumen content ranging from 5%-7% at 0.5% increment) were prepared for the Marshall test, according to

Asphalt Institute [42]. After sample preparation, Marshall stability, flow, and other volumetric properties of the samples were determined. The OBC is taken as the average of bitumen contents. The maximum stability, maximum bulk density, and the median percent of air voids were recorded [42]. The OBC was found to be 5.8% (

Table 5), approximated to 6%. The OBC was used to prepare HMA samples at various percentage replacement of OPC filler with

GCHA. Performance of the mixes were assessed according to Nigerian general specifications for roads and bridges [43], as shown in **Table 6**.

Table 5. Determination of OBC using control mix

Test property	Bitumen content (%)
Max. stability (kN)	6.0
Max. bulk density (g/cm ³)	6.0
Median % air voids	5.3
$OBC = (6+6+5.3)/3 = 5.8\%$	

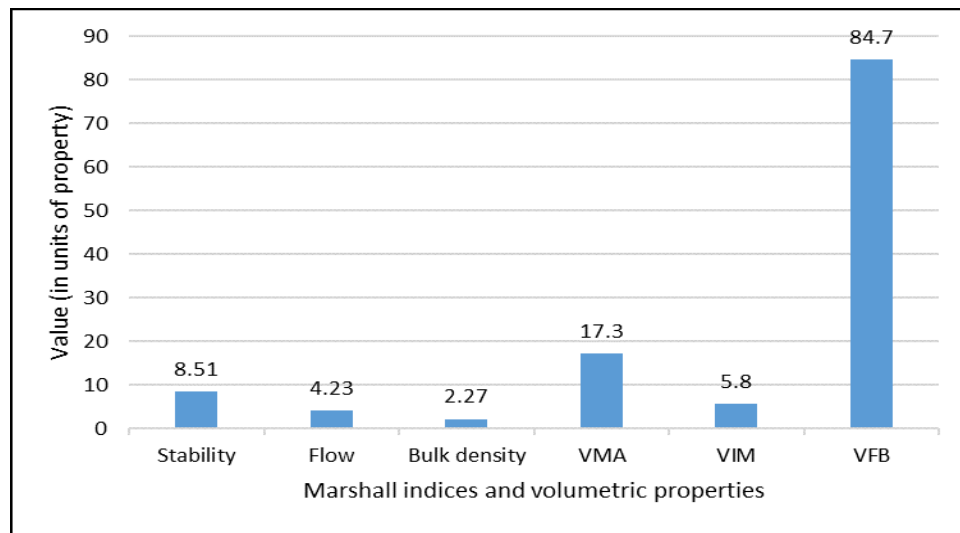


Figure 2: Marshall indices and volumetric properties of reference mix (100% P.C. filler)

3. Results and discussion

This section presents the results and discussion on Marshall stability, flow, and volumetric properties of HMA samples prepared at various percentage replacement of P.C. filler with GCHA. The replacement levels considered range from 5%-45% at 5% increment, and all HMA samples were prepared at the optimum bitumen content. At each replacement level, 3 samples were prepared, and the results of the three were averaged. The volumetric properties considered are; bulk density, voids filled with bitumen (VFB), void in mineral aggregate (VMA), and void in the mix (VIM).

Marshall stability is a measure of HMA resistance to deformation and distortion under traffic loading. This resistance is mainly derived from cohesion (provided by the binder material) and internal friction (provided by interlocking and frictional resistance of aggregates). The increasing trend instability seen in **Figure 3** (between 5% - 20% replacement levels) could not be attributed to the achievement of better cohesion because P.C. (being the primary filler) is a material with better cohesion properties, and its replacement (with a material with weaker

cohesion properties) could not likely yield any better cohesion. This agrees with the assertion in Antunes et al. [44] that siliceous fillers (e.g., GCHA – having high silica content as shown in **Table 4**) form weaker bonds with bitumen compared to basic fillers (e.g. P.C., hydrated lime etc.).

However, this increase could be attributed to an improvement in aggregate gradation. GCHA being finer than P.C., occupies the tiny voids between cement particles yielding a more compact aggregate skeleton. The sudden decline instability after the 20% replacement level could be attributed to the mix's saturation with finer particles. This problem is two-fold. First, it leads to the absorption of more bitumen (by filler material) required to coat aggregates for bonding. Second, the fine particles tend to push the larger particles apart, distorting the initially compact aggregate skeleton. Both scenarios lead to a decrease in the resistance of the HMA to deformation. However, Marshall stability values of HMA samples at all replacement levels considered in this experiment satisfy the minimum value prescribed by NGSRB (3.5%, **Table 6**) for use in the wearing course.

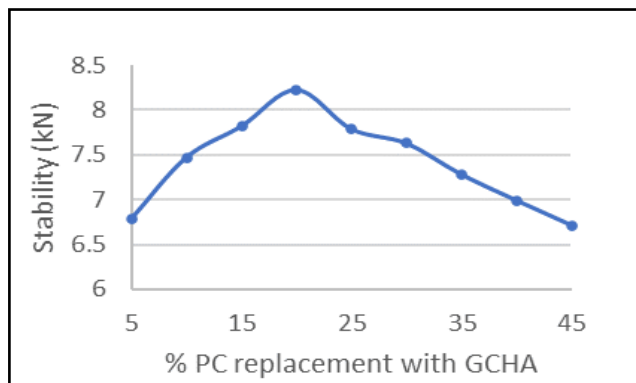


Figure 3. Stability of HMA containing filler blend

Marshall flow, on the other hand, is a measure of deformation (both elastic and plastic) of HMA during the stability test [45]. Allowable limits on the flow of an HMA define boundaries on plasticity or brittleness of the mix. Large flow values indicate a plastic or unstable mix, and too low flow values signal a brittle combination. Both

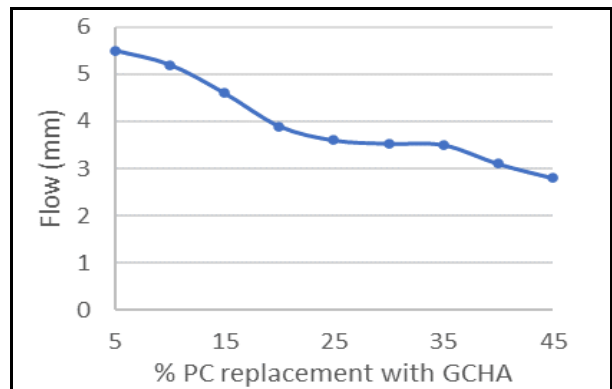


Figure 4. The flow of HMA containing filler blend

extremes are undesirable in HMA. The workability of filler-bitumen mastic (the cementing component of asphalt concrete) influences asphalt concrete flow. The gradual decrease in flow reported in **Figure 4**. The flow of HMA containing filler

blend

is due to the stiffening of the filler-bitumen mastic. The increase in mastic stiffening (and a decrease in the flow of the mix), which increases with P.C. replacement, could be due to GCHA having more absorption properties than P.C.

The bulk specific gravity or bulk density of asphalt concrete is crucial because it influences other volumetric properties and ultimately asphalt concrete strength. This density measurement, unlike the maximum specific gravity, is obtained with voids in the compacted mix. **Figure 5** presents how this asphalt concrete property varies with increasing GCHA content in the compacted mix. The decline in bulk density of the mix (between 5%-20% P.C. replacement levels) is as a result of the replacement of P.C. particles (having higher specific gravity) with GCHA particles (with lower specific gravity). The

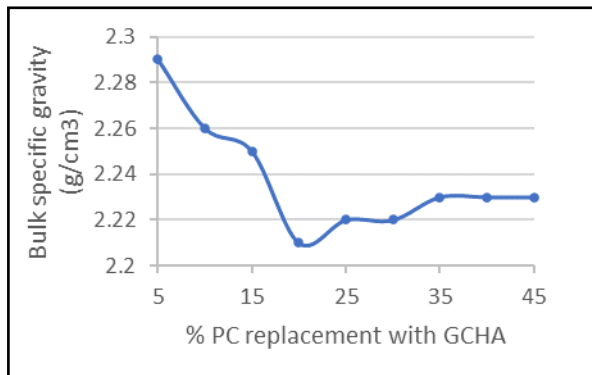


Figure 6. VIM of HMA containing filler blend

A certain percentage of voids is desirable in compacted HMA to allow for the movement of unabsorbed bitumen (through spaces created by the voids) during post-construction compaction of the pavement by traffic weather-induced asphalt expansion. The durability of asphalt pavement is a function of this HMA property. The lower the air-void content, the denser the mix (less permeable). Too high air-void content will provide passageways for air and water and leads to durability problems. Too low air-void content is also undesirable as it leads to bleeding, where the unabsorbed bitumen bleeds out to the surface of the mix.

The introduction of GCHA into the asphalt concrete (up to 20%), causes a gradual increase in

gradual rise in bulk density beyond 20% P.C. replacement could be attributed to forming a compact aggregate skeleton.

GCHA particles are finer than P.C. particles. As such, the replacement of P.C. particles with finer GCHA particles will likely yield a better interlocking of aggregate particles. Although this replacement (at early stage) comes with a decrease in bulk density due to the difference in specific gravity between the two materials (as seen between 5%-20% replacement levels), a replacement-level is reached (around 20% in this experiment) where a more compact aggregate skeleton is formed (with lesser air voids) that leads to increase in bulk density.

Percent air voids or voids in the mix (VIM) defines the percentage of a compacted HMA sample occupied by air voids.

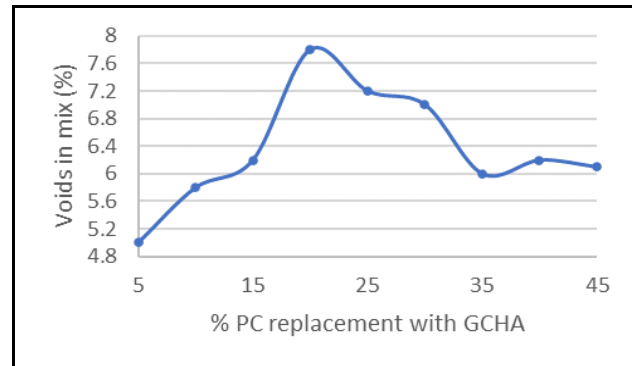


Figure 5. Bulk density of HMA containing

air voids in the compacted mix (**Figure 6**). This increase could be attributed to GCHA particles' greater ability to convert free bitumen to structural bitumen than P.C. particles. Structural bitumen here refers to the bitumen that fills the voids among filler particles. This conversion reduces the amount of free bitumen required to lubricate aggregates and fill intergranular voids. The reduction in percent air voids beyond 20% of P.C. replacement with GCHA could be attributed to the achievement of a compact aggregate skeleton where the void spaces (in fine and coarse aggregates) not filled with bitumen are occupied by smaller but weaker GCHA particles. This trend correlates well with stability and bulk density plots of the compacted HMA (**Figure 3** and **Figure 5** respectively).

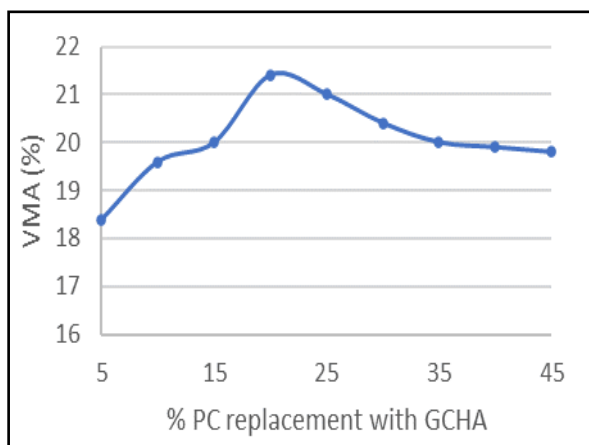


Figure 8: VFB of HMA containing filler blend

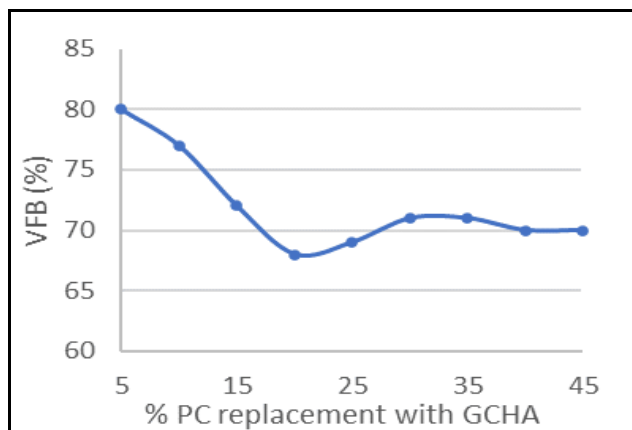


Figure 7: VMA of HMA containing filler blend

Voids in mineral aggregate (VMA) is an HMA design parameter that defines the sum of the volumes of air voids (voids in total mix) and the unabsorbed bitumen (effective binder content) in a compacted HMA sample. Minimum requirements on VMA are set to ensure that sufficient voids are present in the compacted mix to avoid durability problems. The VMA plot in **Figure 7** follows the trend of VIM plot (**Figure 6**) largely because the driving factor in changes in VMA of the mix comes from changes in VIM.

Table 6. NGSRB minimum requirement of HMA for use in pavement surface course

Property	Binder course	Wearing course
OBC (%)	4.5 – 6.5	5.0 – 8.0
Stability (kN), not less Than	3.5	3.5
Flow (mm)	2 – 6	2 – 4
Voids in total Mixture (%)	3 – 8	3 – 5
Voids filled with Bitumen (%)	65 – 72	75 – 82

Voids filled with bitumen (VFB) refers to the portion of VMA filled with bitumen. It is synonymous with a bitumen-void ratio. It has a strong correlation with the bulk density of an HMA. The more the bulk density, the more voids will be filled with bitumen and vice versa. **Figure 8** shows how this HMA design parameter varies with GCHA content. The initial reduction in VFB (up to 20% P.C. replacement) in **Figure 8** could be due to GCHA particles having more voids in compacted dry-state (higher Rigden voids) than P.C. particles. Fillers with higher Rigden voids are

known to produce stiffer mastics [46], increase air voids at constant binder content, and reduce intergranular voids filled with bitumen [47].

4. CONCLUSIONS

This study focused on determining the suitability of PC-GCHA blend for use as a filler material in HMA. Various HMA test samples were prepared according to the Marshall mix design method by varying the proportion of the two filler materials to determine their optimum content,. Satisfies relevant standards for use in flexible pavement construction.

Higher absorption and voids in compacted dry-state of GCHA are likely the driving factors for decreased flow. These, however, reduce the amount of free bitumen needed to coat and fill voids in the compacted HMA and produce weaker mixes with low VFB. Up to 20% P.C. replacement with GCHA as filler material produces HMA with satisfactory performance. Although mixes at all replacement percentages performed below the reference mix (except with decrease in flow achieved), Marshall indices and volumetric properties obtained with up to 20% PC replacement with GCHA satisfy the minimum requirement prescribed by NGSRB for use in binder course of flexible pavements.

ACKNOWLEDGMENT

The authors wish to acknowledge the contributions of staff from soil, concrete, and highway laboratories of the Civil Engineering Department, Ahmadu Bello University, Zaria, Kaduna, Nigeria, for their support during this study. Any grant does not support the work described in this paper. The authors declare that no conflict of interest exists

among them regarding the publication of this paper.

REFERENCES

- [1] National Cooperative Highway Research Program (NCHRP). (2011). *A Manual for Design of Hot Mix Asphalt with Commentary* (Report 673). Transportation Research Board. Washington D.C.
- [2] Lesueur, D., Petit, J., & Ritter, H. J. (2013). The mechanisms of hydrated lime modification of asphalt mixtures: a state-of-the-art review. *Road Materials and Pavement Design*, 14(1), 1-16.
- [3] Csanyi, L. H. (1962). *Functions of fillers in bituminous mixes*. Paper presented at the Symposium on Mineral Fillers for Bituminous Mixtures, Washington D.C.
- [4] Wang, H., Al-Qadi, I. L., Faheem, A. F., Bahia, H. U., Yang, S.-H., & Reinke, G. H. (2011). Effect of mineral filler characteristics on asphalt mastic and mixture rutting potential. *Transportation Research Record*, 2208(1), 33-39.
- [5] Remisova, E. (2015). Study of mineral filler effect on asphalt mixtures properties. Paper presented at the Bituminous Mixtures and Pavements VI. Taylor & Francis Group London
- [6] World Bank Group (2016). *Breaking Down Barriers: Unlocking Africa's Potential Through Vigorous Competition Policy*. World Bank Group, Washington, D.C.
- [7] Ike, C., Ezeibe, C., Anijiofor, S., & Daud, N. (2018). Solid Waste Management in Nigeria: Problems, Prospects, and Policies. *The Journal of Solid Waste Technology and Management*, 44(2), 163-172.
- [8] Mistry, R., & Roy, T. K. (2016). Effect of using fly ash as alternative filler in hot mix asphalt. *Perspectives in Science*, 8, 307-309.
- [9] Modarres, A., & Rahmanzadeh, M. (2014). Application of coal waste powder as filler in hot mix asphalt. *Construction and Building Materials*, 66, 476-483.
- [10] Modarres, A., Ramyar, H., & Ayar, P. (2015). Effect of cement kiln dust on the low-temperature durability and fatigue life of hot mix asphalt. *Cold Regions Science and Technology*, 110, 59-66.
- [11] Shuaibu, A., Otuoze, H., Mohammed, A., & Lateef, M. (2019). Properties of asphalt concrete containing waste foundry sand (wfs) as filler material. *Arid Zone Journal Of Engineering, Technology & Environment*, 15(3), 662-677.
- [12] Choudhary, J., Kumar, B., & Gupta, A. (2018). Application of waste materials as fillers in bituminous mixes. *Waste Management*, 78, 417-425.
- [13] Sargin, Ş., Saltan, M., Morova, N., Serin, S., & Terzi, S. (2013). Evaluation of rice husk ash as filler in hot mix asphalt concrete. *Construction and Building Materials*, 48, 390-397.
- [14] Arabani, M., Tahami, S. A., & Taghipoor, M. (2017). Laboratory investigation of hot mix asphalt containing waste materials. *Road Materials and Pavement Design*, 18(3), 713-729.
- [15] Zainudin, M. Z. M., Khairuddin, F. H., Ng, C. P., Osmi, C., Khadijah, S., Mison, N., & Murniati, S. (2016). Effect of sugarcane bagasse ash as filler in hot mix asphalt. Paper presented at the Materials Science Forum. Trans Tech Publishers, 846, 683-689.
- [16] Choudhary, J., Kumar, B., & Gupta, A. (2020). Utilization of solid waste materials as alternative fillers in asphalt mixes: A review. *Construction and Building Materials*, 234, 117271.
- [17] Mundia, C. W., Secchi, S., Akamani, K., & Wang, G. (2019). A Regional Comparison of Factors Affecting Global Sorghum Production: The Case of North America, Asia and Africa's Sahel. *Sustainability*, 11(7), 2135.
- [18] Nzeke, U. M. (2019). Grains and feed annual report: *Nigeria's Imports of Wheat and Rice to Rise* (NG-19002). USDA's Foreign Agricultural Service (FAS) – United States.
- [19] Ndububa, E. E., & Nurudeen, Y. (2015). Effect of guinea corn husk ash as partial replacement for cement in concrete. *OSR Journal of Mechanical and Civil Engineering*, 12(2), 40-45.
- [20] Wizi, J., Wang, L., Hou, X., Tao, Y., Ma, B., & Yang, Y. (2018). Ultrasound-microwave assisted extraction of natural colorants from sorghum husk with different solvents. *Industrial crops and products*, 120, 203-213. #
- [21] Bello, M., Abdus-Salam, N., & Adekola, F. (2018). Utilization of Guinea corn (Sorghum vulgare) Husk for Preparation of Bio-based Silica and its Characterization Studies.

- International Journal of Environment, Agriculture and Biotechnology*, 3(2).
- [22] Williams, F., Anum, I., Isa, R., & Aliyu, M. (2014). Properties of Sorghum Husk Ash Blended Cement Laterized Concrete. *International Journal of Research in Management, Science & Technology*, 2(2), 73-79.
- [23] Adebayo, V. B., Adebayo, T. D., & Popoola, O. O. (2017). Effects Of Guinea Corn Husk Ash And Lime Mixtures On Lateritic Soil For Highway Construction. *Journal of Multidisciplinary Engineering Science and Technology (JMEST)*, 4(10), 1-7
- [24] Marfo, S., Owusu, W., & Amarfi, E. (2018). Evaluation of Guinea Corn Husk Ash as Oil-Well Cement Slurry Extender. *International Journal of Petroleum and Petrochemical Engineering (IJPPE)*, 4(4), 1-7.
- [25] ASTM D946. (2020). Standard Specification for Penetration-Graded Asphalt Binder for Use in Pavement Construction, ASTM International, West Conshohocken, PA.
- [26] ASTM D5. (1997). Standard Test Method for Penetration of Bituminous Materials, ASTM International, West Conshohocken, PA.
- [27] ASTM D36. (2000). Standard Test Method for Softening Point of Bitumen (Ring-and-Ball Apparatus), ASTM International, West Conshohocken, PA.
- [28] ASTM D92. (2002). Standard Test Method for Flash and Fire Points by Cleveland Open Cup, ASTM International, West Conshohocken, PA.
- [29] ASTM D113. (2017). Standard Test Method for Ductility of Asphalt Materials, ASTM International, West Conshohocken, PA.
- [30] ASTM D70. (2003). Standard Test Method for Specific Gravity and Density of Semi-Solid Bituminous Materials (Pycnometer Method), ASTM International, West Conshohocken, PA.
- [31] ASTM D2042. (2015). Standard Test Method for Solubility of Asphalt Materials in Trichloroethylene, ASTM International, West Conshohocken, PA.
- [32] British Standard Institution. (1990) BS 812-110: Testing aggregates Methods for determination of aggregate crushing value (ACV).
- [33] British Standard Institution. (1990) BS 812-112: Testing aggregates Method for determination of aggregate impact value (AIV).
- [34] ASTM C127. (2015). Standard Test Method for Relative Density (Specific Gravity) and Absorption of Coarse Aggregate, ASTM International, West Conshohocken, PA.
- [35] ASTM C128. (2015). Standard Test Method for Relative Density (Specific Gravity) and Absorption of Fine Aggregate, ASTM International, West Conshohocken, PA.
- [36] British Standard Institution. (1985) BS 812-103.1: Testing aggregates. Method for determination of particle size distribution. Sieve tests.
- [37] British Standard Institution. (2005) BS EN 196-3: Methods of testing cement. Determination of setting times and soundness.
- [38] ASTM C188. (2017). Standard Test Method for Density of Hydraulic Cement, ASTM International, West Conshohocken, PA.
- [39] Tijani, M., Ajagbe, W., & Agbede, O. (2018). Modelling the Effect of burning temperature and time on chemical composition of sorghum husk ash for optimum pozzolanic activity. *FUTA Journal Of Engineering And Engineering Technology*, 12(2), 273-281.
- [40] ASTM C311 / C311M. (2018). Standard Test Methods for Sampling and Testing Fly Ash or Natural Pozzolans for Use in Portland-Cement Concrete, ASTM International, West Conshohocken, PA.
- [41] ASTM C618. (2019) Standard Specification for Coal Fly Ash and Raw or Calcined Natural Pozzolan for Use in Concrete, ASTM International, West Conshohocken, PA.
- [42] Asphalt Institute. (1997). Mix Design Methods for Asphalt, Manual Series No. 2 (MS-02). The Asphalt Institute. Lexington, KY.
- [43] Federal Ministry of Works & Housing – FMWH. (1997). General Specifications for Roads and Bridge. Federal Ministry of Works & Housing Abuja, Nigeria.
- [44] Antunes, V., Freire, A. C., Quaresma, L., & Micaelo, R. (2015). Influence of the geometrical and physical properties of filler in the filler-bitumen interaction. *Construction and Building Materials*, 76, 322-329.
doi:<https://doi.org/10.1016/j.conbuildmat.2014.12.008>.

- [45] ASTM D6927. (2015). Standard Test Method for Marshall Stability and Flow of Asphalt Mixtures, ASTM International, West Conshohocken, PA.
- [46] Faheem, A. F., Hintz, C., Bahia, H. U., Al-Qadi, I. L., & Glidden, S. (2012). Influence of Filler Fractional Voids on Mastic and Mixture Performance. *Transportation Research Record*, 2294(1), 74-80. doi:10.3141/2294-08
- [47] Melotti, R., Santagata, E., Bassani, M., Salvo, M., & Rizzo, S. (2013). A preliminary investigation into the physical and chemical properties of biomass ashes used as aggregate fillers for bituminous mixtures. *Waste Management*, 33(9), 1906-1917.